



UNIVERSIDAD DE CHILE
FACULTAD DE CIENCIAS FÍSICAS Y MATEMÁTICAS
DEPARTAMENTO DE ASTRONOMÍA

**A SEARCH OF MASSIVE COMPANIONS AROUND YOUNG STARS WITH
VLT/NACO**

TESIS PARA OPTAR AL GRADO DE MAGÍSTER EN CIENCIAS, MENCIÓN
ASTRONOMÍA

SEBASTIÁN ANDRÉS JORQUERA CONTRERAS

PROFESORA GUÍA:
LAURA PÉREZ MUÑOZ

MIEMBROS DE LA COMISIÓN:
GAËL CHAUVIN
PAULINA LIRA TEILLERY
PATRICIO ROJO RÜBKE

Este trabajo ha sido parcialmente financiado por:
becaCONICYT-PFCHA/MagísterNacional/2019 - 22191721

SANTIAGO DE CHILE
2021

RESUMEN DE LA MEMORIA PARA OPTAR
AL TÍTULO DE MAGÍSTER EN CIENCIAS,
MENCIÓN ASTRONOMÍA
POR: **SEBASTIÁN ANDRÉS JORQUERA CONTRERAS**
FECHA: 2021
PROF. GUÍA: Laura Pérez

A SEARCH OF MASSIVE COMPANIONS AROUND YOUNG STARS WITH VLT/NACO

En los últimos años, observaciones obtenidas con el Telescopio ALMA han revelado una alta abundancia y ubicuidad de subestructuras en discos de formación planetaria, siendo los más comunes una combinación de anillos brillantes y zurcos oscuros. El origen de dichas subestructuras sigue siendo desconocido, puesto que se ha mostrado que existen múltiples y variados mecanismos capaces de crear las estructuras observadas. Sin embargo, una de las teorías más favorecidas para explicar la presencias de anillos y zurcos en estos sistemas es la existencia de un compañero planetario inserto al interior del disco.

El objetivo de esta Tesis es el lograr la detección de planetas en etapas tempranas de su evolución al interior de discos protoplanetarios. Para esto, se analizan observaciones de alto contraste en la banda L' ($3.8 \mu m$) de 10 discos de formación planetaria, parte de la muestra del "Disks Substructures At High Angular Resolution Project"(DSHARP). Las observaciones en la banda L' son procesadas mediante el uso de múltiples algoritmos de "Angular Differential Imaging"(ADI), los cuales nos permiten resolver fuentes puntuales a partir de una separación proyectada de entre $0.4.^a$ $0.5''$, dependiendo del sistema. El uso de múltiples algoritmos también permite la comparación entre estos, en caso de una detección.

Reportamos la detección de dos fuentes puntuales; una ubicada a una separación de $1.1''$ para el sistema RU Lup, y otra ubicada a $0.42.^{en}$ el sistema Elias 24. En el caso de RU Lup, se comparo el movimiento propio del objeto con observaciones obtenidas con el instrumento SPHERE durante el año 2017. Este análisis muestra que el movimiento propio es consistente con el de un objeto estacionario de fondo, descartando la posibilidad de un compañero planetario. En el caso de Elias 24, no existen detecciones previas que permitan realizar el mismo análisis. Sin embargo, la comparación entre los resultados de los diferentes algoritmos de ADI, junto con tests de inyección de planetas y el hecho de que la posible detección se ubica dentro de uno de los zurcos observados por ALMA, refuerzan la idea de que se trata de una detección real, aunque no es posible confirmarlo en esta etapa. Asumiendo que la detección corresponde a un planeta real, nuestros análisis sugieren una masa que puede variar entre los $0.5 M_{Jup}$ a $5M_{Jup}$, dependiendo de la presencia de un disco circumplanetario y su contribución a la luminosidad de la fuente en la banda L' .

Para todos los demás discos de la muestra no se obtienen detecciones de fuentes puntuales. A partir de los resultados del procesamiento ADI se obtienen mapas de contraste y masa, los cuales permiten derivar límites de detección en magnitud y masa a diferentes separaciones, en conjunto con mapas de probabilidad de detección. Estos resultados nos permiten descartar la presencia de compañeros planetarios con masas superiores a $5M_{Jup}$ para toda la muestra, y sugieren la presencia de compañeros planetarios con masas inferiores a este límite, lo cual es consistente con modelos hidrodinámicos y señales cinemáticas en los discos.

RESUMEN DE LA MEMORIA PARA OPTAR
AL TÍTULO DE MAGÍSTER EN CIENCIAS,
MENCIÓN ASTRONOMÍA
POR: **SEBASTIÁN ANDRÉS JORQUERA CONTRERAS**
FECHA: 2021
PROF. GUÍA: Laura Pérez

A SEARCH OF MASSIVE COMPANIONS AROUND YOUNG STARS WITH VLT/NACO

In the past few years, observations with the ALMA telescope have revealed a high abundance and ubiquity of substructures over a large sample of young planet-forming disks, with the more common ones being a combination of bright rings and dark gaps. The origin of these substructures is still not clear, as it has been shown that multiple different mechanisms are capable of creating the observed structures. However, one of the more favoured theories to explain the presence of rings and gaps in those systems is the presence of a planetary companion embedded into the disk.

The focus of this Thesis is to detection of planets at early evolutionary stages into planet-forming disks. For this, high contrast observations at the L'-band ($3.8 \mu m$) of 10 plane-forming are analyzed, which are part of the sample of the "Disks Substructures At High Angular Resolution Project"(DSHARP). These observations are processed with multiple Angular Differential Imaging (ADI) algorithms, which allow to resolve point-like sources at projected separations between 0.4. and 0.5", depending on the system. The use of multiple algorithms also allows for their comparison in the case of a detection.

We report the detection of two point-like sources; the first on located at a separation of 1.1"for the RU Lup system, and the other located at 0.42.at the Elias 24 system. In the case of RU Lup, the proper motion of the object was compared with observations from the SPHERE instrument during 2017. This analysis shows that is propr motion is consistent with an stationary background object, discarding the hypothesis of a planetary companion. In the case of Elias 24, no previous detection exist of the observed source to perform the same analysis. However, the comparison between the results from the different ADI algorithms, together with tests consisting of injection of fake planets and the fact that the possible detection lies into one of the gaps observed by ALMA, reinforce the idea that it is a real detection, although no confirmation is possible at this stage. Assuming that it is a real planet, our analysis suggests a mass ranging from $0.5 M_{Jup}$ to $5M_{Jup}$, depending on the presence of a circumplanetary disk and its contribution to the L' luminosity of the source.

For all the remaining disks from the sample, no detections are reported. Contrast and mass maps are obtained from the ADI processing, which allow to derive both magnitude and mass detection limits at different separations, together with detection probability maps. Based on these results, we discard thee presence of planetary companions with masses over $5M_{Jup}$ for all our sample, suggesting the presence of lower mass companions, consistent with hydrodynamical simulations and kinematic signatures on the disks.

*A mis padres, Eduardo y Sandra, y a mi hermano, Ignacio
En un año de incertidumbre, fueron la roca que me dio apoyo.*

Agradecimientos

En primer lugar, quiero agradecer de todo corazón a mi familia. A mis padres, Eduardo y Sandra, por aguantar el estrés y mal humor producto del año, por el cariño y apoyo incondicional que siempre me han mostrado, y por siempre creer en mí y motivarme a apuntar a lo más alto. A mi hermano Ignacio, por esa confianza que siempre ha mostrado en mí y en mis capacidades, aún cuando yo mismo dudaba de ellas. El nunca haber escuchado un ápice de duda en su voz al decir que lograría mis proyectos y ambiciones ha tenido un enorme efecto en mí. A mi abuelo Humberto, por enseñarme el amor por aprender y por ser un ejemplo del tipo de persona que quiero ser en mi vida. A mi abuela Olga, por mostrarme que los actos simples muchas veces son las mejores muestras de cariño que se pueden dar. A mis tías Sole y Sara, a mi tío Pato, y a mi prima Sofi, por demostrarme que el cariño y la familia son incondicionales. Y a mi querida 'Nana', que me mostró que el amor no es solo de la familia.

A mi profesora guía, Laura Pérez, gracias por todo el apoyo estos dos años. Gracias por la confianza en mis capacidades y en mi trabajo, por las oportunidades que me has entregado para crecer como profesional y como persona, y por la preocupación y paciencia durante este año. Pero por sobre todo, gracias por haberme dado una segunda oportunidad. A mi profesor guía, Gaël Chauvin, gracias por la disposición y paciencia al enseñarme tantas técnicas y herramientas que eran nuevas para mí, por la voluntad de responder todas mis preguntas sin importar lo simples o básicas que estás puedan ser, y por siempre estar mostrándome nuevas cosas que aprender y en las que trabajar. Ambos me han abierto caminos en los que jamás había pensado, y les estaré eternamente agradecido por esto. Son una inspiración para mí, y si logro ser aunque sea una pequeña parte de las grandes personas e investigadores que son ustedes, puedo darme por satisfecho.

Gracias al equipo de investigación de discos. Myriam, Tere, Anibal, Pauli, he aprendido muchísimo de ustedes, y han sido un punto de apoyo en un año por lo demás incierto. Me alegra saber que así serán mis futuros colegas, y espero sigamos colaborando en el futuro.

Gracias a las amigas y amigos que me han acompañado desde el colegio. A Jorge, por enseñarme que a veces es necesario relajarse y simplemente dejarse llevar. A Coni, por estar en las buenas y en las malas, dispuesta a escuchar y ser la voz de la razón cuando a mí me fallaba. A Pipe, por el apoyo y la confianza que siempre ha mostrado y que no ha cambiado en todos estos años. A Fer y al Flaco, por recordarme que la amistad permanece, sin importar si uno se aleja un poco. Y a todos mis 'Pudies'; Kote, Diego, Dani, Bizama, Mary, Cami, Barraza, Isma, Gato. Puede que no sea el amigo más atento, pero les tengo un enorme cariño a todos y cada uno, y no sería quien soy si no fuera por ustedes. Gracias a los amigos que conocí en la U; Robinson, Max, por haber hecho mi paso por pregrado una gran experiencia. Al equipo de difusión colegios, que aunque sean muchos para nombrarlos, he aprendido muchísimo de cada uno y uno de ustedes, y ser parte de este equipo ha sido una de las mejores experiencias de mi paso por la U. Y Gracias a mi scout, por darme un espacio en el que siempre me siento seguro, pase lo que pase.

Contents

1. Introduction	1
1.1. Motivation	1
1.2. Stellar and planet formation	2
1.3. Substructures in planet-forming disks	4
1.4. Observational strategy: technique and sample	7
1.4.1. The DSHARP sample	7
1.4.2. Direct Imaging	10
2. Observations	13
2.1. L' observations with VLT/NaCo	13
2.2. ADI reduction	16
3. Detection limits of the sample	20
3.1. Mass and contrast detection limits	20
3.2. Detection Probability Maps	21
4. Point-source detections	23
4.1. RU Lup	24
4.2. Elias 24	25
5. Discussion	28
5.1. Planet-Disk interaction	28
5.2. Circumplanetary disk effects	32
5.3. Extinction from planet-forming disk material	34
6. Conclusion	35
6.0.1. Future work	36
Acknowledgements	37
Bibliography	38
Appendix A. ADI reductions	52

Table Index

2.1.	Observing log of targets with VLT/NaCo. Columns are ordered as follows: Column 1: Type of observation. Saturated observations are identified with the name of the corresponding target. PSF correspond to unsaturated exposures. Column 2: Date of the observations. Column 3: Camera and filter used for the observations. ND refers to the NaCo ND_long filter. Column 4: Detector integration time times the number of integrations. Column 5: Final number of data cubes for each target, consisting of NDIT frames with and exposition time of DIT. Each cube has the target located at one of the five offset positions for the target (Several cubes were obtained for each offset position). In some cases, extra observations were obtained to complete the allocated time, producing a discrepancy between the number of data cubes and number of offset positions. Column 5: Parallactic angle at start and end of the observation sequence.	14
2.2.	Star properties from our NaCo sample. Values were extracted from Andrews et al. (2018). The columns are ordered as follows: Column 1: target name. Column 2: Associated star-forming region. Column 3: 2MASS designation. Column 4: distance. Column 5: Spectral type from the literature. Column 6: Effective temperature from the literature. Column 7: Stellar luminosities from the literature, scaled according to the appropriate distance in column 4. Column 8: Stellar masses. Column 9: Stellar ages. Column 10: Accretion rates inferred from accretion luminosities. Column 11: L' magnitudes (magnitude references: (1) Bourges et al. (2017), (2) Cutri and et al. (2014)).	15
5.1.	Mass ranges and accretion rates based on the results from Zhu (2015). Three possible models of a planet plus a CPD are consistent with the derived L' magnitude of the point like source, considering the derived error of 0.14 mag and the distance uncertainties to the host star. The columns are ordered as follows: Column 1: Expected L' magnitude from the CPD models. Column 2: Expected value of $M_p \dot{M}$ from the CPD models. Column 3: CPD inner radius. Column 4: Companion mass range. Column 5: Accretion rates associated with the minimum and maximum mass of the planet, respectively.	33

Figure Index

1.1.	Evolutionary process of a YSO and planetary systems. A pre-stellar core collapses to a protostar still embedded in its envelope. Material keeps falling in and a rotating disk forms around the star. Molecular outflows and accretion remove the envelope material, until only a disk remains. The disk evolves from a massive gas-rich to a gas-poor debris disk, ending as a planetary system. Figure from van der Marel (2015), by Magnus Persson	3
1.2.	Gallery of mm continuum and IR scattered light images of planet-forming disks, from Andrews (2020). Resolutions are marked with white ellipses in the lower-left corners of each panel. For scattered light images, grey circles mark the coronagraphic or bad pixel region. The images correspond to the following systems. (a) ring-cavities: (a,i from left to right) CIDA 9 (Long et al., 2018), Sz 91 (Tsukagoshi et al., 2019), SR 24 S (Pinilla et al., 2017a), HD 34282 (van der Plas et al., 2017), IP Tau (Long et al., 2018) and SR 21 (van der Marel et al., 2018a); (a, ii from left to right) RXJ1604.3-2130 (Pinilla et al., 2018b), DM Tau (Kudo et al., 2018), DoAr 44 (Pinilla et al., 2018b), IRS 48 (Follette et al., 2015), HD 142527 (Avenhaus et al., 2014), and RXJ1604.3-2130 (Pinilla et al., 2018a). (b) ring-gaps: (b,i from left to right) AS 209 (Guzmán et al., 2018), HL Tau (ALMA Partnership et al., 2015), V1094 Sco (van Terwisga et al., 2018), D1 Tau (Tsukagoshi et al., 2019), HD169142 (Pérez et al., 2019) and RU Lup (Andrews et al., 2018); (b, ii from left to right) GO Tau (Long et al., 2018), Elias 24 (Andrews et al., 2018), RXJ1852.3-3700 (Villenave et al., 2019), RXJ1615.3-3255 (Avenhaus et al., 2018), V4046 Sgr (Avenhaus et al., 2018) and HD 163296 (Monnier et al., 2017). (c) arcs: (from left to right) MWC 758 (Dong et al., 2018), SAO 206462 (Cazzoletti et al., 2018), HD 143006 (Pérez et al., 2018), HD 163296 (Isella et al., 2018), V1247 Ori (Kraus et al., 2017) and HD 142527 (Casassus et al., 2013). (d) spirals: (from left to right) IM Lup, WaOph6, Elias 27 (all from Huang et al., 2018b), SAO 206462 (Stolker et al., 2017), MWC 758 (Benisty et al., 2015) and HD 100453 (Benisty et al., 2017).	6

1.3.	<p>Comparison between the observed 1.3 mm continuum emission of the system AS209 and the corresponding hydrodynamical models from Zhang et al. (2018). Key parameter of the simulations are the planet and star mass ratio (M_p/M_*), the viscosity parameter α, the initial gas surface density, $\Sigma_{g,0}$, the maximum grain size s_{max}, and the parameter p, related to the dust size distribution. Panels are ordered as follows: (a) 1.3 mm continuum image of AS209. (b) Synthetic image from the hydrodynamical simulation, considering the presence of a single planet at 99 AU with $M_p/M_* = 0.1M_{Jup}/M_\odot$, $\alpha = 10^{-5}$, $\Sigma_{g,0} = 15 \text{ g cm}^{-2}$, $s_{max} = 0.3 \text{ mm}$ and $p = -3.5$, at an age of $\sim 2 \text{ Myr}$ (c) Similar to panel (b), with different parameters used for the simulation ($M_p/M_* = 0.1M_{Jup}/M_\odot$, varying α, $\Sigma_{g,0} = 6.4 \text{ g cm}^{-2}$, $s_{max} = 0.68 \text{ mm}$ and $p = -3.5$, with an age of $\sim 1.35 \text{ Myr}$). The intensity and structures observed in the hydrodynamical models are in very good agreement with the real observations of the system, supporting the idea that the observed structures are produced by the interaction of the disk with a planetary companion. The distance between two ticks on the axes is 40 AU. From Zhang et al. (2018)</p>	8
1.4.	<p>Comparison between the observed 1.3 mm continuum emission of the system Elias 24 and the corresponding hydrodynamical model from Zhang et al. (2018). Panels are ordered as follows: (a) 1.3 mm continuum image of AS209. (b) Synthetic image from the simulation, considering the presence of a single planet at 57 AU, with $M_p/M_* = 0.2M_{Jup}/M_\odot$, $\alpha = 5 \times 10^{-4}$, $\Sigma_{g,0} = 15 \text{ g cm}^{-2}$, $s_{max} = 2 \text{ mm}$ and $p = -3.5$, considering an age of of 0.43 Myr for the system. The intensity and structures observed in the hydrodynamical models are in very good agreement with the real observations of the system, supporting the idea that the observed structures are produced by the interaction of the disk with a planetary companion. The distance between two ticks on the axes is 40 AU. From Zhang et al. (2018)</p>	8
1.5.	<p>1.3 mm continuum images of the DSHARP sample. Beam size is shown at the bottom left of each panel, together with a 10 au scale bar at the bottom right. Disks observed on this work are marked with a white check symbol. Figure from Andrews et al. (2018).</p>	10
1.6.	<p>Distribution of planet mass vs separation of known exoplanets as listed on exoplanets.eu (Schneider et al., 2011). Planets are identified by different colors depending on the method used for their detection. Transparent boxes mark the range of semi-major axes and masses for different families of exoplanets. An additional box marks the region of semi-major axis vs mass expected for the systems presented in this work. Figure by Gaël Chauvin</p>	12

2.1.	Schematic representation of the ADI method. A_i correspond to the set of images obtained for the target. An imaginary companion is represented with a red dot, with a red dashed line representing the path it follows due to the apparent rotation of the FOV. A reference psf, B, is created by calculating the median for each pixel from A_i . Due to the rotation of the FOV, signal from the companion doesn't appear in B. The reference PSF is then subtracted from the original frames, creating the set C_i . This subtracted frames only contains the signal from the companion plus some remaining artifacts at the innermost regions of the image. Frames are then derotated to align the signal of the companion, creating the set D_i . Finally, the derotated frames are median combined to obtain the final image, E. All methods used on this work follow the same basic steps, with the only difference being the method used to create the reference PSF. Figure by Carlos Gomez	17
2.2.	Gallery containing the all the reduction for the system AS 209. PSF and nADI refer to the original PSF obtained for the system and the median combination of all frames without applying any of the ADI methods, respectively. Although the results are similar, slight differences can be appreciated between the different ADI reduction methods. No companion was found for this system	18
2.3.	ALMA and NaCo gallery of all observed targets. ALMA images (left panels) are from the DSHARP survey, NaCo images (right panels) are the results from the Classical ADI reduction. White (grey) dashed lines mark the bright rings (dark gaps) of each disk, as derived by Huang et al. (2018a). Point-like sources are marked by a white arrow when recovered after the ADI reduction. A 10 AU scalebar is shown in the lower left corner of each cADI panel, the beam size of the ALMA images is shown in the lower left corner of each ALMA panel. In the case of HT Lup, variation of the parallactic angle was too low for proper cADI processing. The result from the PCA processing is presented instead.	19
3.1.	5σ contrast and mass limits for possible companions obtained using the sADI algorithm as a function of separation for all the targets in our sample. Conversion from magnitude to mass were obtained based on COND model predictions and the age, distance and L' magnitude of the host stars presented in Table 2.2 . .	21
3.2.	Detection probability maps for the single-star targets in our survey. Shaded green regions correspond to the location and width of the observed gaps of the disks, as derived by Huang et al. (2018a). Red lines indicate the location of the point sources presented in this work for Elias 24 and RU Lup. Our mass contrast limits are based on COND model predictions. In all cases, detection probability increases with both separation and mass, having a 50 % probability for masses $\sim 5M_{Jup}$ at ≈ 100 AU around almost all targets.	22
4.1.	L' band images for RU Lup after processing using four different ADI algorithms. An additional reduction using the ANDROMEDA algorithm (Cantalloube et al., 2015) was performed as a test for the detection. A point source is recovered at the same position, marked with a circle, for all algorithms.	23
4.2.	L' band images for Elias after processing using four different ADI algorithms. A point source is recovered at the same position, marked with a circle, for all algorithms.	24

4.3.	Relative astrometry for the point-source detected in RU Lup, at three different epochs, from bottom to top: March-2016, March-2017 and May-2019. The predicted motion of a comoving object follows the black line, with the red dots being the expected astrometry of a comoving object at the different epochs of the observations. Blue dots are the real astrometry of the observed point-source at the different epochs of the observations. Error bars are obtained by propagation of errors, considering the intrinsic error of 0.2 pixels for star centering, the True North and plate scale error of the instrument, and the error of the position fitting for the observed point source.	25
4.4.	Comparison of the two different epochs of observation of Elias 24, using the PCA method. The same color scale is used for both observations. The signal of the possible companion was not recovered again during the second epoch, which was reduced using the RDI method.	27
5.1.	Cut of our MESS Detection probabilities at the possible planet locations considered by Zhang et al. (2018). Red vertical lines mark the highest mass needed for a planet to produce the observed gaps in the disk, as predicted by the hydrodynamical models.	28
5.2.	Cut of our MESS Detection probabilities at the possible planet locations obtained by Pinte et al. (2020). Red shaded intervals correspond to the mass range $1M_{Jup} - 3M_{Jup}$. In the three cases, planets location is consistent with the radius of one of the disk gaps.	30
5.3.	Candidate velocity kinks detected in the 12CO J=2-1 DSHARP data. Dashed circles indicate the velocity kinks, and the cyan dots the location of the planet assuming it is in the disk midplane. Solid lines in the third column indicate the expected location of the isovelocity curves at $\pm 0.2v_{Kep}\sin i$, where v_{Kep} is the Keplerian velocity at the location of the planet and i the disk inclination. From Pinte et al. (2020)	31
A.1.	Gallery containing the all the reduction for the system AS 209. PSF and nADI refer to the original PSF obtained for the system and the median combination of all frames without applying any of the ADI methods, respectively. Although the results are similar, slight differences can be appreciated between the different ADI reduction methods. No companion was found for this system	52
A.2.	Gallery containing the all the reduction for the system Elias 24. PSF and nADI refer to the original PSF obtained for the system and the median combination of all frames without applying any of the ADI methods, respectively. Although the results are similar, slight differences can be appreciated between the different ADI reduction methods. An apparent point-like source can be observed at a separation of $\sim 0.4''$ (~ 55 AU) and a position angle of $\sim 300^\circ$ in all the different reductions, as discussed in Sect. 4.2	53
A.3.	Gallery containing the all the reduction for the system HD 143006. PSF and nADI refer to the original PSF obtained for the system and the median combination of all frames without applying any of the ADI methods, respectively. Although the results are similar, slight differences can be appreciated between the different ADI reduction methods. Some artifacts remained after the LOCI reduction, but were impossible to completely remove due to the fact that the remotion of more images would compromise the FOV rotation needed for the ADI algorithms to properly work. No companion was found for this system	53

A.4.	Gallery containing the all the reduction for the system AS 205. PSF and nADI refer to the original PSF obtained for the system and the median combination of all frames without applying any of the ADI methods, respectively. Although the results are similar, slight differences can be appreciated between the different ADI reduction methods. Due to the presence of a binary companion, detection at the separation of the secondary star is not possible. No companion was found for this system	54
A.5.	Gallery containing the all the reduction for the system RU Lup. PSF and nADI refer to the original PSF obtained for the system and the median combination of all frames without applying any of the ADI methods, respectively. Although the results are similar, slight differences can be appreciated between the different ADI reduction methods. An apparent point-like source can be observed at a separation of $\sim 1.1''$ (~ 55 AU) and a position angle of $\sim 260^\circ$ in all the different reductions, as discussed in Sect. 4.1	54
A.6.	Gallery containing the all the reduction for the system Sz 129. PSF and nADI refer to the original PSF obtained for the system and the median combination of all frames without applying any of the ADI methods, respectively. Although the results are similar, slight differences can be appreciated between the different ADI reduction methods. No companion was found for this system	55
A.7.	Gallery containing the all the reduction for the system Wa Oph 6. PSF and nADI refer to the original PSF obtained for the system and the median combination of all frames without applying any of the ADI methods, respectively. Although the results are similar, slight differences can be appreciated between the different ADI reduction methods. No companion was found for this system	55
A.8.	Gallery containing the all the reduction for the system GW Lup. PSF and nADI refer to the original PSF obtained for the system and the median combination of all frames without applying any of the ADI methods, respectively. Although the results are similar, slight differences can be appreciated between the different ADI reduction methods. No companion was found for this system	56
A.9.	Gallery containing the all the reduction for the system Sz 114. PSF and nADI refer to the original PSF obtained for the system and the median combination of all frames without applying any of the ADI methods, respectively. Due to lack of enough FOV rotation, only the PCA method was applied. No companion was found for this system	56
A.10.	Gallery containing the all the reduction for the system HT Lup. PSF and nADI refer to the original PSF obtained for the system and the median combination of all frames without applying any of the ADI methods, respectively. Due to lack of enough FOV rotation, only the PCA method was applied. No companion was found for this system	57

Chapter 1

Introduction

1.1. Motivation

Since the first confirmed detection of an exoplanet (Wolszczan and Frail, 1992) almost three decades ago the search for other worlds has revealed a broad variety of planetary systems architectures, in terms of multiplicities, orbital parameters, and physical properties (Winn and Fabrycky, 2015). Multiple factors are believed to influence the final configuration of planetary systems, such as the initial conditions of the environments where planets are formed (Benz et al., 2014; Mordasini, 2018), the different mechanisms of planetary formation (e.g., core accretion, Pollack et al. 1996; gravitational instability, Cameron 1978, Boss 1997), and the dynamical interactions that these systems go through (Privitera et al., 2016; Rao et al., 2018). It is then essential to understand the role of each of these evolution steps in shaping young, planetary systems, including the ones that might host telluric planets able to sustain life. In this context, the search of planetary companions in young planet-forming disks offers a great opportunity to deepen our understanding about the formation and evolution of planetary systems. Detection of these young protoplanets not only is crucial to test the predictions of planetary formation and evolution theories, but also to understand the correlation between the disk and planet properties.

In this thesis we present the results of an observational campaign to directly image massive companions in 10 young planet-forming disks, using L' ($\lambda_0 = 3.8\mu\text{m}$, $\Delta\lambda = 0.62\mu\text{m}$) high contrast imaging with the NAOS-CONICA (NaCo) instrument that was installed at the Very Large Telescope (VLT). The objective of this work is to correlate the presence of massive companions with the spatial sub-structures (rings, gaps, cavities, vortices, spirals, etc) detected in the dust thermal emission of disks observed with the Atacama Large Millimeter Array (ALMA) at high resolution in the continuum at 1.3mm. As will be discussed in the upcoming chapters, in the case of a direct detection of young proto-planets in direct imaging, one can then derive fundamental properties such as mass or effective temperature using the predictions of evolutionary models (Baraffe et al., 2003), predicting the bulk properties of giant planets over time. These predictions can then be compared to the ones obtained by hydrodynamical simulations of the disk to explain the formation of the observed spatial substructures seen with ALMA in these systems (Zhang et al., 2018). If no planetary candidates are detected, our observations still allow to set upper limits on the masses of the planetary perturbers at different separations creating the substructures, by deriving the minimum contrast between the host star and the planet that would produce a detectable signal.

The work is presented as it follows: the remainder of this chapter presents a theoretical background on planet-forming disks and planet formation, followed by theories on the formation of annular structures on disks and a presentation of the DSHARP project as well as our sub-sample. Chapter 2 describes the selection criteria as well as the observational strategy for the sample, followed by the description of the data processing. Chapter 3 presents the results obtained regarding the detection limits and detection probability maps for all targets of the sample, while Chapter 4 focus on the apparent detection of a point source in the systems RU Lup and Elias 24. A discussion comparing our results with the prediction of hydrodynamical models, kinematic signatures on the disk, and the possible presence of a circumplanetary disk in the case of the detection on Elias 24, is presented in Chapter 5. Finally, our conclusions are presented in Chapter 6.

1.2. Stellar and planet formation

Stars are formed by the gravitational collapse of high density cores in molecular clouds (Shu et al., 1987). Due to conservation of the angular momentum of the core, its rotational velocity naturally increases as it collapse, forming a flat rotating disk structure surrounding the protostar (Terebey et al., 1984) commonly known as protoplanetary or planet-forming disk.

The evolutionary stages of young stellar objects (YSO) going from a high density core to a planet-forming disk, and later a planetary system, are identified by different Classes, based on their spectral energy distribution (SED) between 2 and 25 μm (Lada, 1987). Class 0-I stages are characterized by a rapid accretion of material into the protostar, producing a significant growth of these objects. No optical and very low near-IR emission can be observed for these protostars over a period of $\sim 10^5$ yrs, due to the presence of an envelope of material blocking these wavelengths (Evans et al., 2009). After less than 1 Myr the transition to the Class II stage is characterized by an actively accreting star surrounded by a planet-forming disk, with strong emission in the ultraviolet (UV) and some spectral lines such as H_α . Emission from both the disk and central star can be observed, as the envelope is expected to be removed at this point due to accretion and molecular outflows (van der Marel, 2015). Duration of this stage varies greatly for each particular system, with an average duration of a few Myr (Williams and Cieza, 2011). Finally, the Class III stage is characterized by a mostly passive and depleted disk, and the emission of the system is greatly dominated by the stellar photosphere. A diagrammed version of this evolutionary path is presented in Fig. 1.1

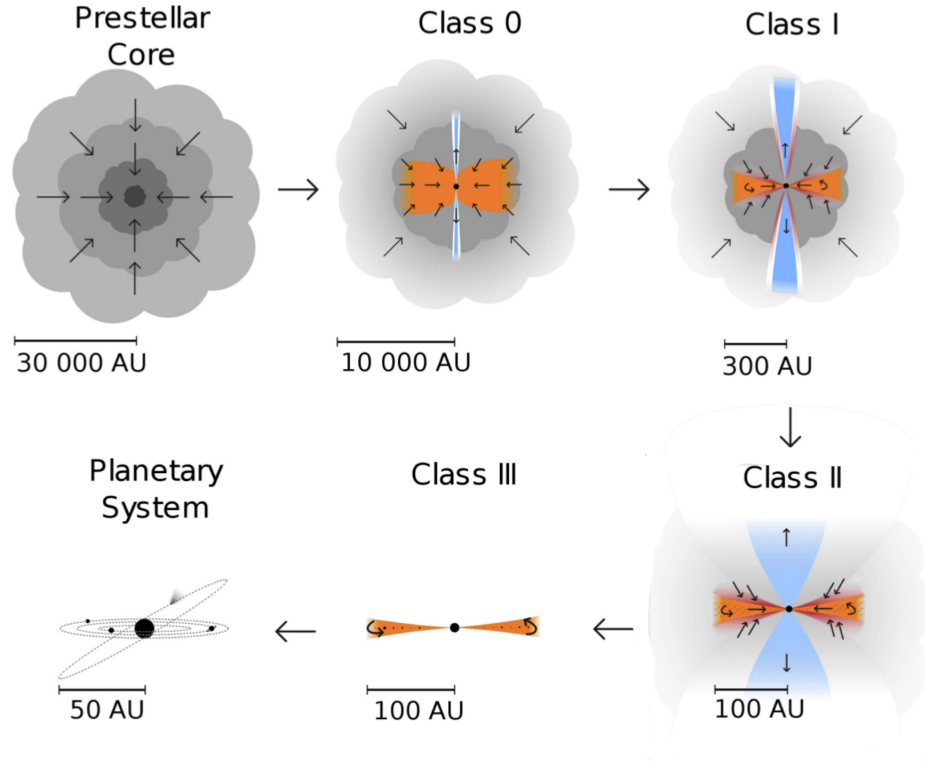


Figure 1.1: Evolutionary process of a YSO and planetary systems. A pre-stellar core collapses to a protostar still embedded in its envelope. Material keeps falling in and a rotating disk forms around the star. Molecular outflows and accretion remove the envelope material, until only a disk remains. The disk evolves from a massive gas-rich to a gas-poor debris disk, ending as a planetary system. Figure from van der Marel (2015), by Magnus Persson

In the case of planets, their formation and evolution occurs parallel to the evolution of the disk, and they are expected to be completely formed by the Class III stage. For giant planets, which are the focus of this work, there are two main mechanisms by which planets can be formed. The first bottom-up scenario is commonly known as core accretion (Pollack et al., 1996). Initially, the dust particles in the disk settle in its midplane at timescales of around 10^3 yrs (Armitage, 2011). The increase in density in this region allows the growth of the dust grains by sticking together, forming millimeter and centimeter particles (Natta et al., 2007). Planetesimals, which are the foundations of planetary cores, are then formed by the growth of the already bigger particles (Klahr and Brandner, 2006). When the planetary core is formed, it keeps growing via accretion of solid planetesimals, and its surrounded by a near-hydrostatic gaseous envelope. When the core reaches a critical mass ($\sim 10 - 15M_{\oplus}$), the core-envelope system becomes unstable and the envelope collapses, provoking a phase of rapid gas accretion. The mass of the planet can rapidly increase to several Jupiter masses, forming the giant planet. The other mechanism is the so-called gravitational instability formation (Boss, 1997). In this top-down scenario, a gravitational unstable disk suffers from fragmentation due to its own self-gravity, forming clumps of gas and dust called giant gaseous protoplanets (GGPPs), which then suffer of gravitational collapse to form giant planets. This gravitational instability scenario predicts the formation of planets at large separations from the host star, and in very short timescales (10^5 years). Both scenarios are extremely dependent on the physical properties of planet-forming disks, making the study of these systems

crucial to understand the current population of existing exoplanets.

1.3. Substructures in planet-forming disks

Planet-forming disks were initially believed to be smooth during early stages of evolution (Class I & II), yet high resolution imaging of planet-forming disks have revealed the presence of numerous substructures, such as rings/gaps (Fedele et al., 2017; Andrews et al., 2018; Dipierro et al., 2018; Huang et al., 2018a; Long et al., 2018), or spirals (ALMA Partnership et al., 2015; Pérez et al., 2016; Tang et al., 2017; Avenhaus et al., 2017; Huang et al., 2018b; Monnier et al., 2019), across a wide range of ages (from < 1 Myr and upwards of 10 Myr, e.g. Benisty et al., 2017; Pérez et al., 2018; Sheehan and Eisner, 2018). To illustrate the different substructures that can be observed in planet-forming disks, a gallery of multiple high resolution mm continuum and infrared (IR) scattered light images are showcased in Figure 1.2.

Of the observed structures, annular rings and gaps appear to be the most common. The origin of these substructures is still unclear, as many different physical mechanisms can create the observed features. For example, gaps and rings can be formed by dust accumulation in snowline regions (Okuzumi et al., 2012; Zhang et al., 2015; Pinilla et al., 2017b) due to three main factors; in first place the sublimation of icy particles into the snowlines produces a net mass loss for the solid particles, thus reducing the dust surface density on this regions. Second, gas liberated from the ices can be mixed back and re-condensed, enhancing the particle growth and dust surface density in regions outside the snowline. Finally, ices can change the particle strength, thus affecting the collision outcome between dust particles, resulting in either the enhancement of larger particles or the depletion of smaller particles at different snowlines. Zonal flows due to the magnetorotational instability (Johansen et al., 2009; Simon and Armitage, 2014) can also explain the observed structures. In this case, magnetohydrodynamic outflows produce local perturbations in the gas pressure distribution. Particularly, if the gas dynamics are modified by concentric concentrations of magnetic flux, it will be piled up in an annuli pushing away from regions of peak magnetic stress. This will subsequently produce variations in the radial pressure distribution, inducing annuli where solids will be trapped, inducing the formation of concentric rings and gaps. Finally, induction by young planetary companions forming inside the disk can also produce the observed rings and gaps (Paardekooper and Mellema, 2004; Fouchet et al., 2010; Pinilla et al., 2012; Bae et al., 2018), as the gravitational interaction between the companion and the disk produces spiral shocks that transfer angular momentum and repels the disk dust away from its orbit.

There is, however, building evidence that puts the planetary companion theory as the favoured mechanism for the origin of the observed annular structures. The location of gaps appears to be uncorrelated with the snowline location of common molecules (van der Marel et al., 2018b). Also, kinematic deviations have been observed at the location of the gaps, which have been explained by the presence of planetary-mass perturbers (e.g., Teague et al., 2018; Pinte et al., 2019; Casassus and Pérez, 2019, Further discussion in Section 5.1). The ubiquity of this annular substructures observed at high angular resolutions also supports the planetary companion postulate, as is one of the only common explanations for such diverse systems, and as we know that this mechanism is efficient given the large occurrence of pla-

netary systems and exoplanets observed in transit and radial velocity around older, main sequence stars.

Multiple studies have been carried out aiming to find a correlation between the observed annular substructures and the presence of one or multiple planetary companions embedded into the planet-forming disk, considering for example the orbital evolution of the planet (Li et al., 2019) and the relation between the disk and the companion properties (Zhang et al., 2018; Bae et al., 2018). Although these works put strong constraints on the physical properties of both the disks and the possible companions, which are in agreement with the formation of the observed dark gaps, they have also revealed that the origin of these structures can be explained with different configurations of planetary masses and disks properties (e.g., viscosity, grain size distribution, disk thermodynamics, etc.). So, given that the properties of a planetary companion are dependent on disk properties that are still not properly constrained, it is not possible to properly conclude whether these gaps are, in fact, evidence of the presence of a planetary companion or not, as it is almost always possible to find a combination of disk and planet properties that could explain the observed gaps. One solution for this problem is to directly observe and characterize the possible companions, to compare with the planetary and disks properties derived from these models.

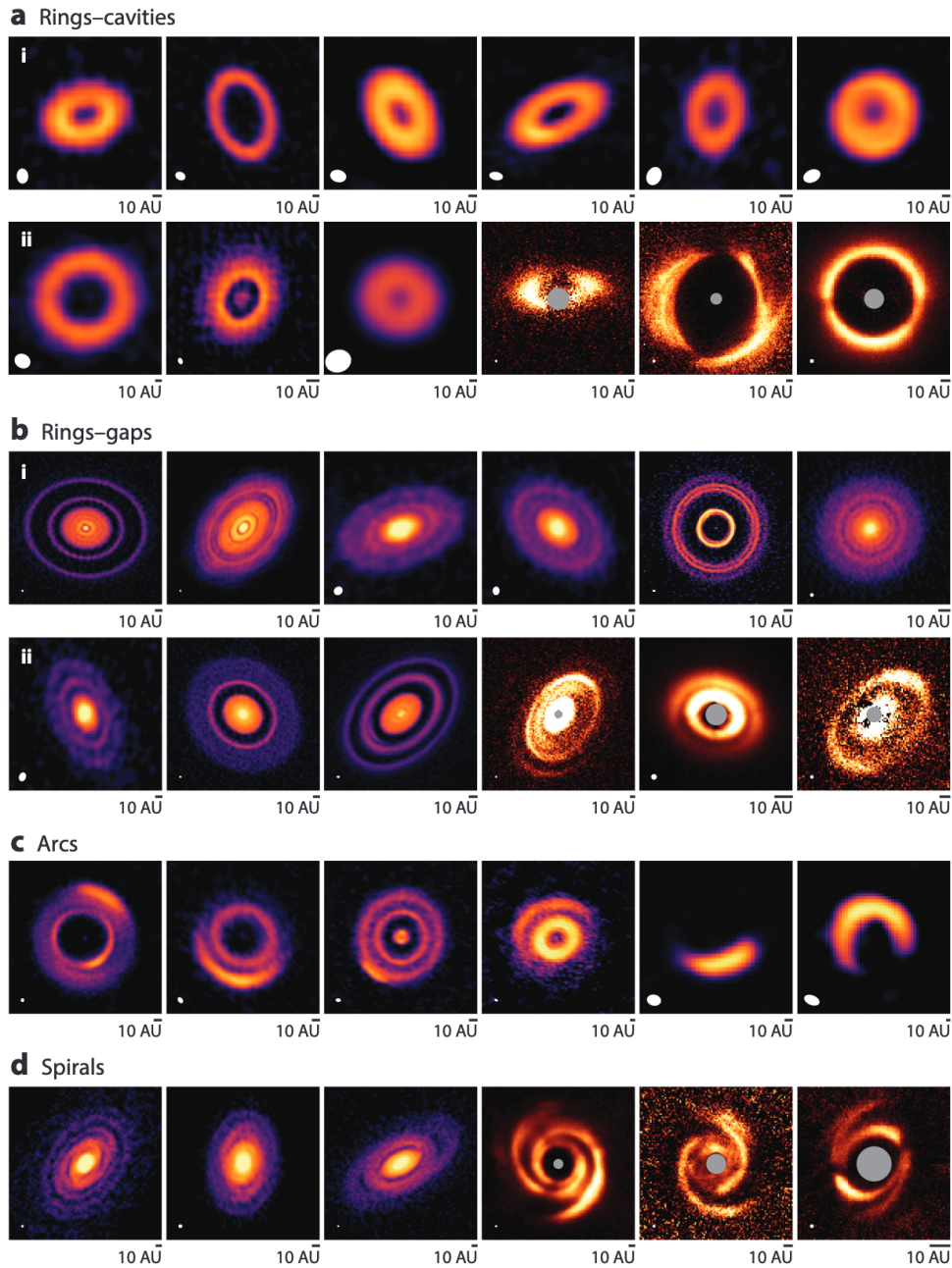


Figure 1.2: Gallery of mm continuum and IR scattered light images of planet-forming disks, from Andrews (2020). Resolutions are marked with white ellipses in the lower-left corners of each panel. For scattered light images, grey circles mark the coronagraphic or bad pixel region. The images correspond to the following systems. (a) ring-cavities: (a,i from left to right) CIDA 9 (Long et al., 2018), Sz 91 (Tsukagoshi et al., 2019), SR 24 S (Pinilla et al., 2017a), HD 34282 (van der Plas et al., 2017), IP Tau (Long et al., 2018) and SR 21 (van der Marel et al., 2018a); (a, ii from left to right) RXJ1604.3-2130 (Pinilla et al., 2018b), DM Tau (Kudo et al., 2018), DoAr 44 (Pinilla et al., 2018b), IRS 48 (Follette et al., 2015), HD 142527 (Avenhaus et al., 2014), and RXJ1604.3-2130 (Pinilla et al., 2018a). (b) ring-gaps: (b,i from left to right) AS 209 (Guzmán et al., 2018), HL Tau (ALMA Partnership et al., 2015), V1094 Sco (van Terwisga et al., 2018), DI Tau (Tsukagoshi et al., 2019), HD169142 (Pérez et al., 2019) and RU Lup (Andrews et al., 2018); (b, ii from left to right) GO Tau (Long et al., 2018), Elias 24 (Andrews et al., 2018), RXJ1852.3-3700 (Villenave et al., 2019), RXJ1615.3-3255 (Avenhaus et al., 2018), V4046 Sgr (Avenhaus et al., 2018) and HD 163296 (Monnier et al., 2017). (c) arcs: (from left to right) MWC 758 (Dong et al., 2018), SAO 206462 (Cazzoletti et al., 2018), HD 143006 (Pérez et al., 2018), HD 163296 (Isella et al., 2018), V1247 Ori (Kraus et al., 2017) and HD 142527 (Casassus et al., 2013). (d) spirals: (from left to right) IM Lup, WaOph6, Elias 27 (all from Huang et al., 2018b), SAO 206462 (Stolker et al., 2017), MWC 758 (Benisty et al., 2015) and HD 100453 (Benisty et al., 2017).

1.4. Observational strategy: technique and sample

As mentioned in section 1.1, the focus of this work is the direct imaging of planetary companions in young planet-forming disks. In this section we will address the reasons to use this approach, as well as the criteria for the selection of our sample.

1.4.1. The DSHARP sample

To determine the ideal candidates to search for planetary companions, first we have to take into account the different evolutionary stages of planet-forming disks. As mentioned before, Class I disks are surrounded by an envelope of material that blocks most of the optical and IR emission from the disk, difficulting the detection of any possible protoplanet. At the other end of the disk evolution we have the Class III objects, which have already been proven as good candidates for direct imaging of planets (e.g., Marois et al., 2008). However, at this point most of the material from the disk is expected to have been removed and any formed planet would be at their final evolutionary stages, making it extremely difficult to correlate the properties of the planet with the conditions and properties of the disk during its formation and evolution. Class II disks appear to be the only remaining option, and there are actually strong arguments on why these kind of disks are extremely well suited for this study. Most of the observed substructures have been detected in Class II objects, indicating that planet formation is already taking place in these systems, assuming that the structures have been formed due to the presence of a forming protoplanet. Also, unlike Class I and III disks, it is feasible to determine properties such as viscosity, grain size distribution, and density profile, among others for this type of objects by studying the distribution of dust and gas in the disk. Knowledge of these physical properties is crucial to understand how planets and planet-forming disks influence each other during their evolution, as mentioned in section 1.3.

With the aim set on Class II disks, the question remains on which systems might be well suited for the direct detection of planetary companions embedded into the disk. In this context, the Atacama ALMA Large Program titled "Disks Substructures at High Angular Resolution Program" (DSHARP, Andrews et al., 2018) provides a unique sample of young circumstellar disks where to search for planetary companions. This survey was aimed towards the study and characterization of substructures on planet-forming disks, as well as the relation between these substructures and young protoplanets. The project consisted of high spatial resolution observations (~ 35 mas) at a wavelength of 1.3 mm of 20 young systems from the ρ -Ophiuchus (Wilking et al., 2008), Lupus (Comerón, 2008) and Upper Scorpius (Preibisch and Mamajek, 2008) star forming regions. The interest in this sample arises from multiple key points; in first place, annular substructures appear to be ubiquitous in the objects from the DSHARP sample (Huang et al., 2018a). Second, observed structures are consistent with the presence of planets, as supported by hydrodynamical models of the DSHARP disks (Zhang et al., 2018), some of which are presented in Fig. 1.3 and 1.4, as well as from studies on the dust trapping in the main rings of the disks (Dullemond et al., 2018). Finally, the relatively young age of the systems (~ 1 Myr on average), makes it ideal to both study the planet-disk interactions that could produce these features and the properties of giant planets in formation or recently formed.

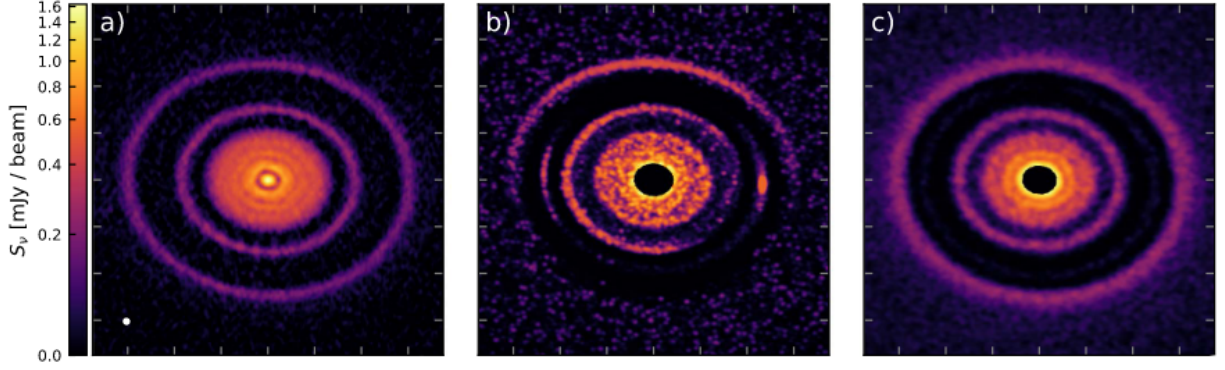


Figure 1.3: Comparison between the observed 1.3 mm continuum emission of the system AS209 and the corresponding hydrodynamical models from Zhang et al. (2018). Key parameter of the simulations are the planet and star mass ratio (M_p/M_*), the viscosity parameter α , the initial gas surface density, $\Sigma_{g,0}$, the maximum grain size s_{max} , and the parameter p , related to the dust size distribution. Panels are ordered as follows: (a) 1.3 mm continuum image of AS209. (b) Synthetic image from the hydrodynamical simulation, considering the presence of a single planet at 99 AU with $M_p/M_* = 0.1M_{Jup}/M_\odot$, $\alpha = 10^{-5}$, $\Sigma_{g,0} = 15 \text{ g cm}^{-2}$, $s_{max} = 0.3 \text{ mm}$ and $p = -3.5$, at an age of $\sim 2 \text{ Myr}$ (c) Similar to panel (b), with different parameters used for the simulation ($M_p/M_* = 0.1M_{Jup}/M_\odot$, varying α , $\Sigma_{g,0} = 6.4 \text{ g cm}^{-2}$, $s_{max} = 0.68 \text{ mm}$ and $p = -3.5$, with an age of $\sim 1.35 \text{ Myr}$). The intensity and structures observed in the hydrodynamical models are in very good agreement with the real observations of the system, supporting the idea that the observed structures are produced by the interaction of the disk with a planetary companion. The distance between two ticks on the axes is 40 AU. From Zhang et al. (2018)

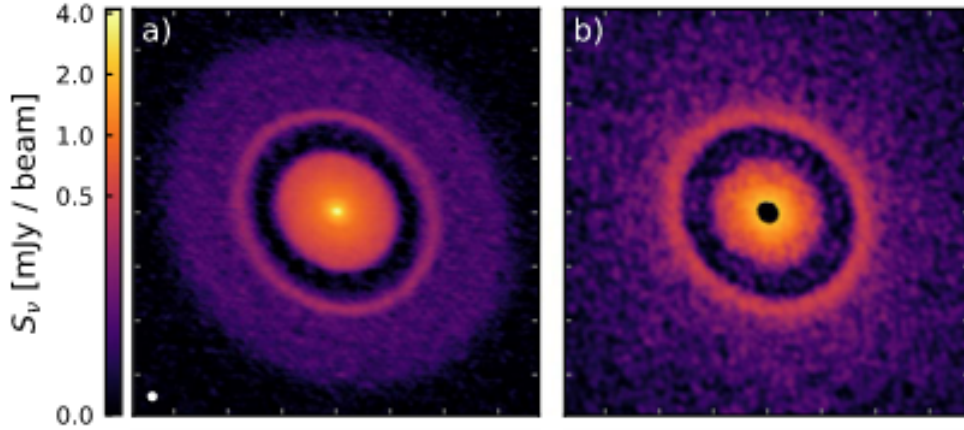


Figure 1.4: Comparison between the observed 1.3 mm continuum emission of the system Elias 24 and the corresponding hydrodynamical model from Zhang et al. (2018). Panels are ordered as follows: (a) 1.3 mm continuum image of AS209. (b) Synthetic image from the simulation, considering the presence of a single planet at 57 AU, with $M_p/M_* = 0.2M_{Jup}/M_\odot$, $\alpha = 5 \times 10^{-4}$, $\Sigma_{g,0} = 15 \text{ g cm}^{-2}$, $s_{max} = 2 \text{ mm}$ and $p = -3.5$, considering an age of of 0.43 Myr for the system. The intensity and structures observed in the hydrodynamical models are in very good agreement with the real observations of the system, supporting the idea that the observed structures are produced by the interaction of the disk with a planetary companion. The distance between two ticks on the axes is 40 AU. From Zhang et al. (2018)

Its important to note that although this sample is very well suited for this study, it suffers

of a notorious bias. Besides the fact that target selection was narrowed to only include Class II objects to avoid any confusion from the envelope emission, a brightness cut was also applied to select systems with high enough SNR to differentiate the structures from a smooth profile. These two criteria made the sample to lean towards very bright continuum sources, which are correlated with higher mass stars (Andrews et al., 2013).

Due to observational constraints imposed for the proper detection of embedded companions into the DSHARP disks, and the faintness of various of these targets for the NaCo Adaptive Optic system, a smaller sample of 10 of the original 20 disks were observed for this work. The disks observed with NaCo were HD 143006, AS 209, Elias 24, WaOph 6, GW Lup, AS 205, Sz 129, Sz 114, HT Lup and RU Lup. Figure 1.5 showcases the full sample of DSHARP, together with our selected targets. Further details regarding the sample selection for this work are given in section 2.1.

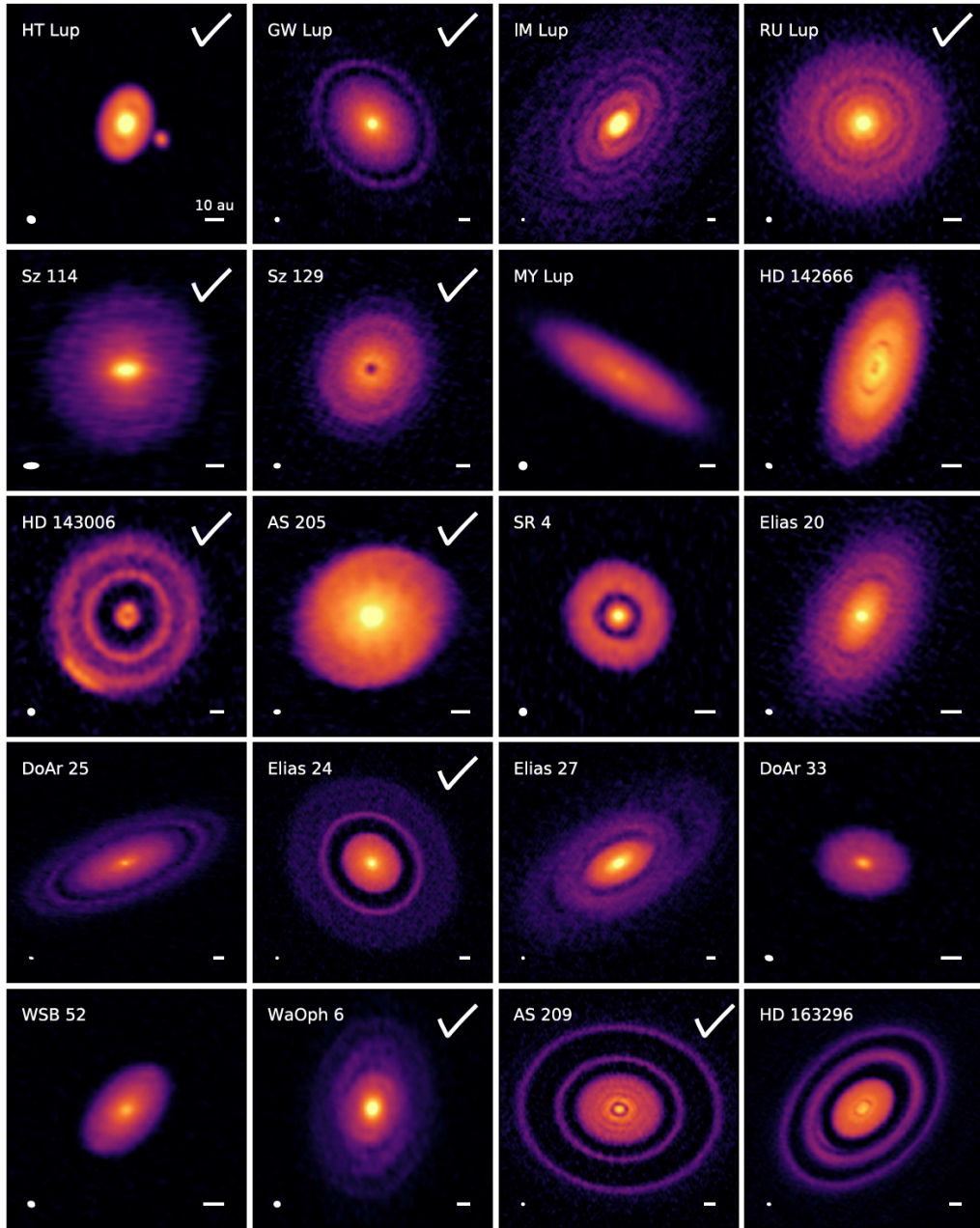


Figure 1.5: 1.3 mm continuum images of the DSHARP sample. Beam size is shown at the bottom left of each panel, together with a 10 au scale bar at the bottom right. Disks observed on this work are marked with a white check symbol. Figure from Andrews et al. (2018).

1.4.2. Direct Imaging

As of today, multiple techniques exist for the detection of exoplanets, with the most successful being the radial velocity (RV, Wright, 2018) and transit (Deeg and Alonso, 2018) methods, as can be seen in Figure 1.6. However, these two methods suffer from an intrinsic bias towards short period planets, as the perturbations from the companion have to be detected multiple times over the allocated time of the observations for it to be considered a real detection. As the observed substructures in planet-forming disks span a wide range

of separations (from 5 up to 150 AU; Huang et al., 2018a), these methods are not suitable for the search of planetary companions on these systems. In addition, RV and, on a lower extent transits, are significantly affected by stellar activity and have a lower performance for the detection of young protoplanets. Direct imaging, on the other side, doesn't suffer of these limitations, as modern instruments allow to detect exoplanets at separations over a few astronomical units (~ 5 AU, although this can vary for each specific target depending on its distance and other parameters such as its luminosity). This technique has already proven to be an extremely useful tool for the detection and characterization of possible companions in the presence of transition and debris disks at large separations (HR 8799, Marois et al. 2008; β Pictoris, Lagrange et al. 2009; HD 95086, Rameau et al. 2013b; HD 206893, Milli et al. 2017; PDS 70, Keppler et al. 2018).

To further increase the probability of a detection, we opted for L'-band ($3.8 \mu m$) observations. The reasons to select this particular band are multiple. In first place, the peak emission of a $1000 - 1800^\circ K$ blackbody, corresponding to planets of a few M_{Jup} , lies between $3 - 5 \mu m$. If the planets are also actively accreting material, then it is also expected for them to be surrounded by a circumplanetary disk (CPD), which have been shown to be very bright at $\lambda > 3 \mu m$, increasing the chance for a detection with the L' band (e.g., Zhu, 2015; Szulágyi et al., 2019, further discussion on this point is given in section 5.2). Finally, extinction from the planet-forming disk in the IR is expected to be lower for longer wavelengths, with L' being one of the less affected bands (e.g., Sanchis et al., 2020, further discussion in section 5.3).

The selected sample and detection method offers the unique opportunity to observe the formation of giant planets within their birth environment, study the planet-disk architecture and interactions, and access the orbital parameters together with the luminosity and atmospheric properties of the planets. A more detailed explanation on the specifics of the observations, such as the used instrument, configuration, and data analysis tools is given in the following chapter.

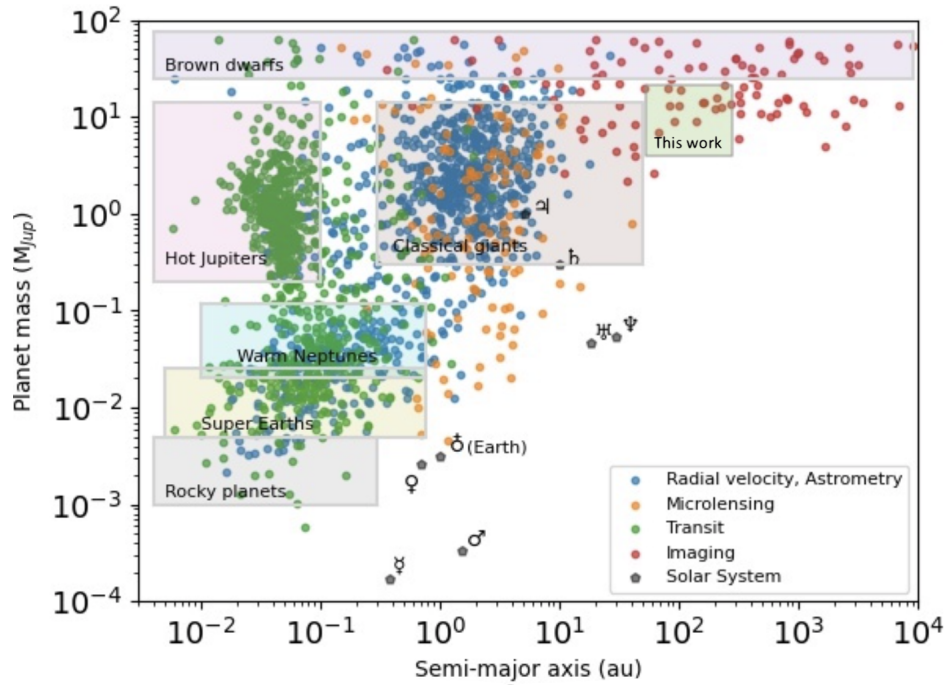


Figure 1.6: Distribution of planet mass vs separation of known exoplanets as listed on exoplanets.eu (Schneider et al., 2011). Planets are identified by different colors depending on the method used for their detection. Transparent boxes mark the range of semi-major axes and masses for different families of exoplanets. An additional box marks the region of semi-major axis vs mass expected for the systems presented in this work. Figure by Gaël Chauvin

Chapter 2

Observations

2.1. L' observations with VLT/NaCo

This work uses data obtained with the NaCo instrument at the Very Large Telescope, located at Cerro Paranal in Atacama, Chile. The NaCo instrument is composed of the NAOS Adaptive Optics (AO) system and the near-infrared imager and detector CONICA. As mentioned in Sect. 1.4.1, only 10 of the original 20 targets from the DSHARP sample were observed. The reasons for this reduced sample are the following. In first place, the infrared wavefront sensor of NAOS poses a limiting sensing magnitude of $K < 9 - 10$ mag for the proper operation of the Adaptive Optics system of the instrument, which is crucial for this kind of observations. Due to this magnitude limits, only 16 systems from the original DSHARP sample were eligible for the program. Also, to ensure the stability of the PSF, which is crucial for the performance of the ADI algorithms, heavy constraints were imposed for the observations (sidereal time constraints to observe close to meridian and avoid the zenith, airmass=1.4, seeing = 0.8, Strehl ratio > 40%). These constraints, together with the decommissioning of NaCo in October 2019, made possible to only observe 10 of the 16 eligible targets. Table 2.2 compiles the observed sample, together with their stellar hosts properties.

Observations were carried out over more than a year, starting on June 16th, 2018, and ending on September 29th, 2019. Given the red colours of our targets, the infrared wavefront sensor was used with the JHK dichroic. The L27 camera was used for data acquisition, which provides a sampling of $\simeq 27.1$ mas/pixel, together with the broadband L' filter ($\lambda_0 = 3.8\mu\text{m}$, $\Delta\lambda = 0.62\mu\text{m}$).

Pupil-tracking mode, necessary for the use of Angular Differential Imaging (ADI), was used to reduce instrumental speckles that limit the detection performances at inner angles. To optimize frame selection as well as sky and instrumental background removal, we use NaCo cube mode with a window field of view of 512×520 pixels (FoV of $\approx 14'' \times 14''$), a short integration time of 0.2 seconds per frame, and a dithering pattern of five offset positions.

Each observation is composed of a shallow starting and ending sequence with unsaturated exposure using the neutral density filter ND_Long, with a transmission of $\sim 1.75\%$ for L'. This sequence provides an estimation of the stellar point spread function (PSF) and serves as a photometric calibrator. The central sequence is composed of deep saturated images without the neutral density filter, following the five dithering pattern over a total observing time of

2 hours to maximize the FoV rotation. The detail of the exposure time (DIT), the number of frames per offset position (NDIT) and number of offset positions is given in Table 2.1, together with the parallactic angle variation and the observing condition of each target.

Table 2.1: Observing log of targets with VLT/NaCo. Columns are ordered as follows: Column 1: Type of observation. Saturated observations are identified with the name of the corresponding target. PSF correspond to unsaturated exposures. Column 2: Date of the observations. Column 3: Camera and filter used for the observations. ND refers to the NaCo ND_long filter. Column 4: Detector integration time times the number of integrations. Column 5: Final number of data cubes for each target, consisting of NDIT frames with and exposition time of DIT. Each cube has the target located at one of the five offset positions for the target (Several cubes were obtained for each offset position). In some cases, extra observations were obtained to complete the allocated time, producing a discrepancy between the number of data cubes and number of offset positions. Column 5: Parallactic angle at start and end of the observation sequence.

Type	Date	Cam./Filter	DIT \times NDIT	N_{cubes}	π -start/end
HD 143006	2018 Jul 12/13	L27/L'	0.2×70	280	-99.1/99
HD 143006 PSF	2018 Jul 12/13	L27/L'+ND	0.2×50	52	-
AS 209	2018 Jul 13/14	L27/L'	0.2×70	280	-157.4/140.7
AS 209 PSF	2018 Jul 13/14	L27/L'+ND	0.2×50	52	-
Elias 24	2018 Jul 15/16	L27/L'	0.2×70	260	-94.8/95.3
Elias 24 PSF	2018 Jul 15/16	L27/L'+ND	0.2×50	62	-
WaOph 6	2019 Apr 28/29	L27/L'	0.2×70	300	-129.8/122.5
WaOph 6 PSF	2019 Apr 28/29	L27/L'+ND	0.2×50	51	-
RU Lup	2019 May 2/3	L27/L'	0.2×70	280	-52.9°/49.2°
RU Lup PSF	2019 May 2/3	L27/L'+ND	0.2×50	51	-
GW Lup	2019 Jun 3/4	L27/L'	0.2×70	188	-61.6/13.4
GW Lup PSF	2019 Jun 3/4	L27/L'+ND	0.2×50	31	-
AS 205	2019 Jun 5/6	L27/L'	0.2×70	316	-117.5/113.1
AS 205 PSF	2019 Jun 5/6	L27/L'+ND	0.2×50	52	-
Sz 129	2019 Jul 4/5	L27/L'	0.2×70	286	-45.9/43.7
Sz 129 PSF	2019 Jul 4/5	L27/L'+ND	0.2×50	52	-
HT Lup	2019 Sep 10/11	L27/L'	0.2×70	78	87.6/91.9
HT Lup PSF	2019 Sep 10/11	L27/L'+ND	0.2×50	21	-
Elias 24	2019 Sep 27/28	L27/L'	0.2×70	80	99.9/101.6
2MASS J17354481-2413439	2019 Sep 27/28	L27/L'	0.2×70	80	98.8/100.5
Sz 114	2019 Sep 28/29	L27/L'	0.2×70	286	-45.9/43.7
Sz 114 PSF	2019 Sep 28/29	L27/L'+ND	0.2×50	52	-

In the case of the object Elias 24, a second set of observations was obtained after the apparent detection of a point source in one of the gaps of the disk (more details in chapter 4). The set-up for this second set of observations was designed for the usage of Radial Differential imaging (RDI) as the data reduction method, since it would allow to relax the observational constraints at the meridian passage in an attempt to secure the re-observation of this system. For this, we obtained consecutive saturated science images for Elias 24 and the reference star 2MASS J17354481-2413439 ($L' = 6.388 \pm 0.079$, Cutri et al., 2003) with similar parallactic angle variation. The reference star was selected based on its separation from the source and similar luminosity and spectral type. This approach allows us to use the PSF of the reference star as a model for the PSF of Elias 24 during the RDI reduction process (further detail in Chapter 4).

Table 2.2: Star properties from our NaCo sample. Values were extracted from Andrews et al. (2018). The columns are ordered as follows: Column 1: target name. Column 2: Associated star-forming region. Column 3: 2MASS designation. Column 4: distance. Column 5: Spectral type from the literature. Column 6: Effective temperature from the literature. Column 7: Stellar luminosities from the literature, scaled according to the appropriate distance in column 4. Column 8: Stellar masses. Column 9: Stellar ages. Column 10: Accretion rates inferred from accretion luminosities. Column 11: L' magnitudes (magnitude references: (1)Bourges et al. (2017), (2)Cutri and et al. (2014)).

Name	Region	2MASS	d	SpT	log T	log L	log M	log t	log Mdot	L'
(1)	(2)	(3)	(4)	(5)	(6)	(7)	(8)	(9)	(10)	(11)
HT Lup	Lup I	J15451286-3417305	154 ± 2	K2	3.69 ± 0.02	0.74 ± 0.20	0.23 ^{+0.26} _{-0.13}	5.9 ± 0.3	< -8.4	5.8 ± 0.12 ⁽¹⁾
GW Lup	Lup I	J15464473-3430354	155 ± 3	M1.5	3.56 ± 0.02	-0.48 ± 0.20	-0.34 ^{+0.10} _{-0.17}	6.3 ± 0.4	-9.0 ± 0.4	8.4 ± 0.02 ⁽²⁾
RU Lup	Lup II	J15564230-3749154	159 ± 3	K7	3.61 ± 0.02	0.16 ± 0.20	-0.20 ^{+0.12} _{-0.11}	5.7 ± 0.4	-7.9 ± 0.4	6.0 ± 0.12 ⁽¹⁾
Sz 114	Lup III	J16090185-3905124	162 ± 3	M5	3.50 ± 0.01	0.69 ± 0.20	-0.76 ^{+0.08} _{-0.07}	6.0 ^{+0.1} _{-0.8}	-9.1 ± 0.3	8.7 ± 0.02 ⁽²⁾
Sz 129	Lup IV	J15591647-4157102	161 ± 3	K7	3.61 ± 0.02	-0.36 ± 0.20	-0.08 ^{+0.03} _{-0.15}	6.6 ± 0.4	-8.3 ± 0.3	7.8 ± 0.03 ⁽²⁾
HD 143006	Upper Sco	J15583692-2257153	165 ± 5	G7	3.75 ± 0.02	0.58 ± 0.15	0.25 ^{+0.05} _{-0.08}	6.6 ± 0.3	-8.1 ± 0.4	5.8 ± 0.12 ⁽¹⁾
AS 205	Upper Sco	J16113134-1838259	128 ± 2	K5	3.63 ± 0.03	0.33 ± 0.15	-0.06 ^{+0.07} _{-0.05}	5.8 ± 0.3	-7.4 ± 0.4	4.6 ± 0.22 ⁽²⁾
Elias 24	Oph L1688	J16262407-2416134	136 ± 3	K5	3.63 ± 0.03	0.78 ± 0.20	-0.11 ^{+0.16} _{-0.08}	5.3 ± 0.4	-6.4 ± 0.5	6.6 ± 0.08 ⁽²⁾
WaOph 6	Oph N 3a	J16484562-1416359	123 ± 2	K6	3.62 ± 0.03	0.46 ± 0.20	-0.17 ^{+0.17} _{-0.09}	5.5 ± 0.5	-6.6 ± 0.5	6.2 ± 0.08 ⁽²⁾
AS 209	Oph N 3a	J16491530-1422087	121 ± 2	K5	3.63 ± 0.03	0.15 ± 0.20	-0.08 ^{+0.11} _{-0.14}	6.0 ± 0.4	-7.3 ± 0.5	6.4 ± 0.07 ⁽²⁾

2.2. ADI reduction

Direct detection of planetary companions is quite a difficult task. In first place, the brightness of a possible companions is orders of magnitude fainter than the background stellar point-spread function, making extremely hard to resolve its emission separately from the host star and surrounding planet-forming disk. Together with this, short lived speckles are produced randomly due to atmospheric aberrations, which could mask the presence of a faint companion. An increase on the integration time for the observations doesn't help to solve this problems, as observations have shown that for integration times over a few minutes the PSF noise converges to a quasistatic noise pattern and prevents the gain with increasing integration time (Marois et al., 2006).

The ADI technique is a PSF calibration technique that takes advantage of the PSF quasistatic noise pattern to suppress the PSF signal. For a long enough integration time, the quasistatic noise pattern becomes dominant over incoherent noise sources such as the sky or short lived speckles. By using the pupil-tracking mode of NaCo, the field of view (FOV) is slowly rotating from one image to the next in the same sequence of observations, while the PSF remains relatively stable during the full sequence. A reference PSF is then obtained for each image of the sequence based on all the other images of the same sequence, which is then subtracted to the science image to remove the quasistatic structures. If enough FOV rotation occurred during the sequence such as a point source has moved by at least twice its full width at half maximum (FWHM), this subtraction preserves the faint signal from an eventual companion. The PSF subtracted images are finally derotated to align the FOV and median combined. An schematic view of the method is showed in Figure 2.1

For our observations we applied multiple variations of the ADI technique, namely:

- Classical ADI (cADI), where the reference PSF is obtained by calculating the median of the science cube.
- Smart ADI (sADI), where the reference PSF for each science image is created considering frames that have rotated more than $\alpha \times \text{FWHM}$, with α a resolution criteria decided by the user.
- Radial ADI (rADI), which follows the same selection criteria that the sADI method but repeated for multiple separations.
- Locally optimized combination of images (LOCI, Lafrenière et al., 2007). This method is based on the use of an optimization zone (larger than the subtraction zone) to determine the best combination of reference PSFs used to remove the PSF signal from the science frame. To do this, coefficients for the linear optimization are computed by minimizing the sum of the squared residuals of the combination of the reference frames for the PSF subtraction using various set of user defined parameters, such as criteria of separation, size of optimization zone, radial width and ratio of the radial-to-azimuthal widths of subtraction zones.
- Principal Component Analysis (PCA, Soummer et al., 2012), which which creates an orthogonal basis of eigenimages based on the available reference PSFs, which are then linearly combined to produce a synthetic PSF which can be then subtracted to the

science PSF. The basis or modes, as will be referred further on, are ordered such that the first modes represent the the most general perturbations of the PSF, while each subsequent mode includes perturbations of decreasing importance. Because of this, an increasing number of modes provides a more aggressive subtraction of the PSF.

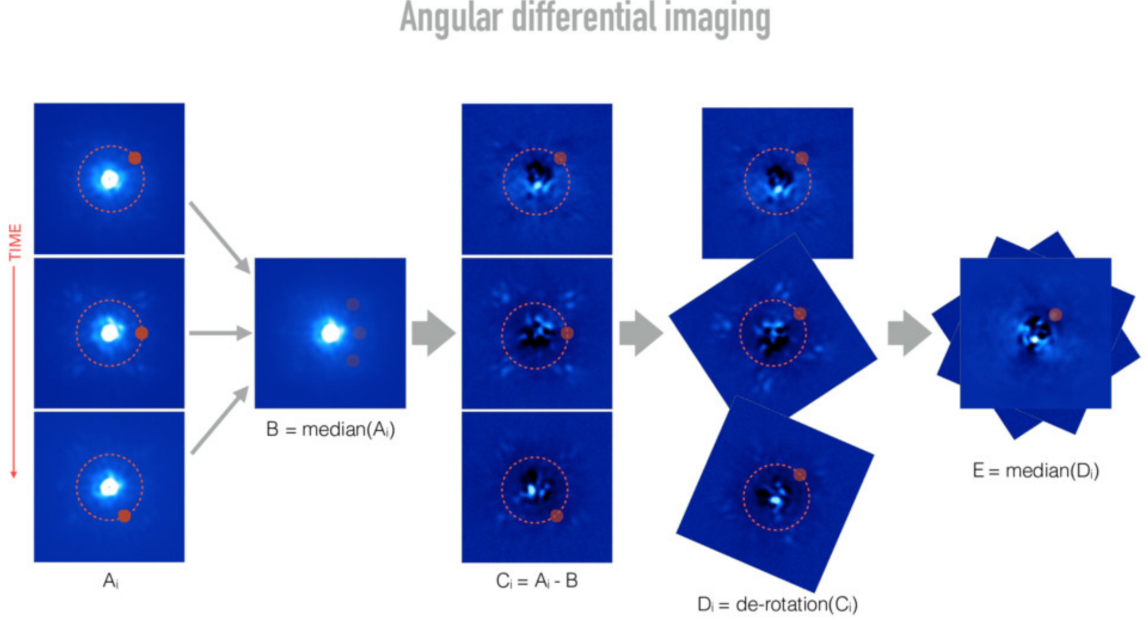


Figure 2.1: Schematic representation of the ADI method. A_i correspond to the set of images obtained for the target. An imaginary companion is represented with a red dot, with a red dashed line representing the path it follows due to the apparent rotation of the FOV. A reference psf, B , is created by calculating the median for each pixel from A_i . Due to the rotation of the FOV, signal from the companion doesn't appear in B . The reference PSF is then subtracted from the original frames, creating the set C_i . This subtracted frames only contains the signal from the companion plus some remaining artifacts at the innermost regions of the image. Frames are then derotated to align the signal of the companion, creating the set D_i . Finally, the derotated frames are median combined to obtain the final image, E . All methods used on this work follow the same basic steps, with the only difference being the method used to create the reference PSF. Figure by Carlos Gomez

As a first step, data reduction (flat-fielding, bad pixels, and sky removal) was performed on all the available cubes of each target. Sub-frames of 128×128 pixels (FoV of $3.5'' \times 3.5''$) were extracted to reduce computation time. These frames were then re-centered following a Moffat fitting on the non-saturated part of the stellar PSF wing. The last step was to remove the bad frames (poorly saturated, overly extended PSF) to obtain a final master cube containing all the reduced frames, together with their parallactic angles. The reduced images were then processed with all the previously mentioned algorithms using the IPAG-ADI pipeline (Chauvin et al., 2012)

For sADI, rADI and LOCI, we followed a similar configuration as Chauvin et al. (2012), with a $FWHM = 4.5$ pixels and a separation criteria of $0.75 \times FWHM$ at the companion separation, to preserve the signal of any possible companion. For the PCA method,

observations were reduced using three different number of modes ($k = 1, 5, 20$), to test the permanence of any possible companion and discard artifacts induced by the reduction. An exclusion radius of 60 pixels is also considered, so that the PSF modeling is done by only considering the signal inside this radius for all reference PSFs.

An example of the results from all the methods for one of our targets is presented in Figure 2.2. Figure 2.3 presents the results obtained from the data processing for all targets, together with a comparison with their respective 1.3 mm continuum images obtained by DSHARP. The full results from the data processing for each target considering all the previously mentioned methods can be found in Appendix A.

In the case of detections, we considered the solution of the contemporaneous ISPY survey over 2018 and 2019 for the plate scale and True North calibration used to derive the relative astrometry of the candidates, (Launhardt et al., 2020): pixel scale of 27.193 ± 0.059 mas, and True North of -0.568 ± 0.115 deg.¹

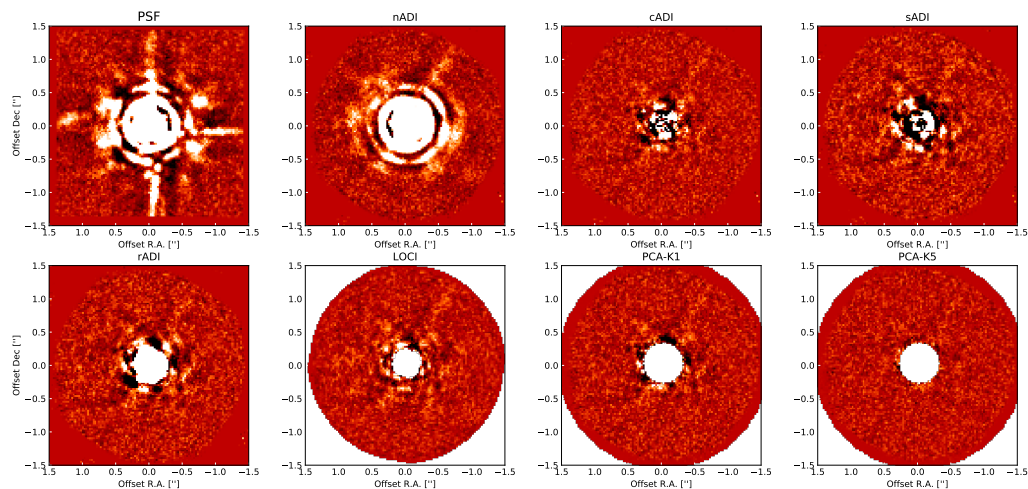


Figure 2.2: Gallery containing the all the reduction for the system AS 209. PSF and nADI refer to the original PSF obtained for the system and the median combination of all frames without applying any of the ADI methods, respectively. Although the results are similar, slight differences can be appreciated between the different ADI reduction methods. No companion was found for this system

¹ Note that Launhardt et al. (2020) refer to the True North correction in Table C.2 in Appendix.

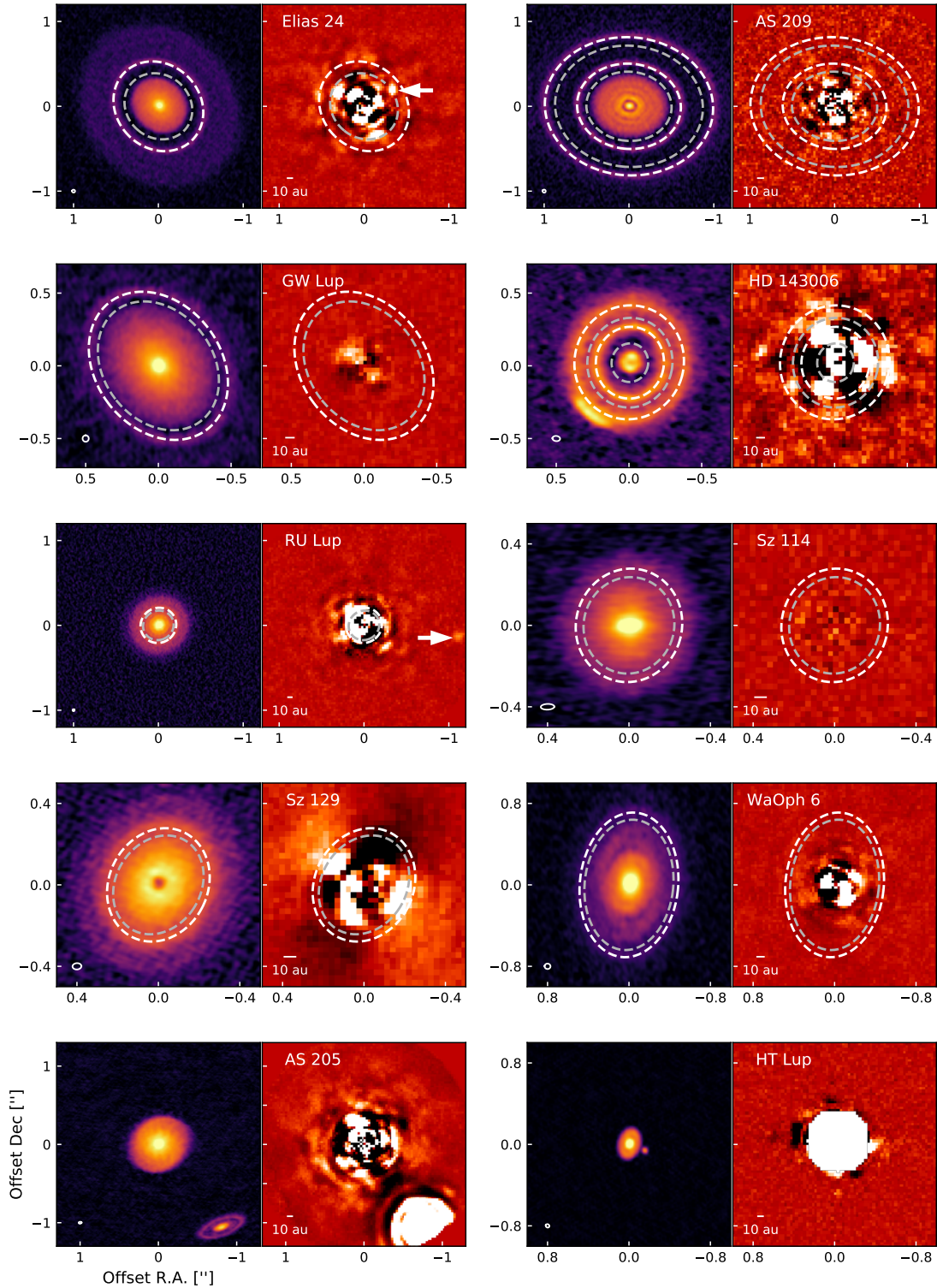


Figure 2.3: ALMA and NaCo gallery of all observed targets. ALMA images (left panels) are from the DSHARP survey, NaCo images (right panels) are the results from the Classical ADI reduction. White (grey) dashed lines mark the bright rings (dark gaps) of each disk, as derived by Huang et al. (2018a). Point-like sources are marked by a white arrow when recovered after the ADI reduction. A 10 AU scalebar is shown in the lower left corner of each cADI panel, the beam size of the ALMA images is shown in the lower left corner of each ALMA panel. In the case of HT Lup, variation of the parallactic angle was too low for proper cADI processing. The result from the PCA processing is presented instead.

Chapter 3

Detection limits of the sample

The analysis presented in this chapter is part of a paper titled “A search for companions via direct imaging in the DSHARP planet-forming disks” by Jorquera et al. 2020 (Accepted by AJ).

Regardless of the presence or lack of a detection of a possible planetary companion after the ADI processing, it is possible to extract significant information regarding the limit at which a detection will be feasible, in both magnitude and mass, of each individual target. This allows us to put constraints on the physical properties of theorized companions, which can then be compared with predictions from models of the disks and other indirect evidences of the presence of a protoplanet.

3.1. Mass and contrast detection limits

Pixel-to-pixel noise maps of each ADI reduction were estimated within a sliding box of $1.5 \times 1.5 FWHM$ in the NaCo field of view. To correct for the flux loss related to the ADI processing, fake planets were regularly injected every 10 pixels at 3 different position angles, with a flux corresponding to 100 ADU on the original data cubes before PSF subtraction. The cubes were then reprocessed using the different ADI algorithms, allowing us to estimate the flux loss by computing the azimuthal average of the flux losses for fake planets at the same radii (e.g., Chauvin et al., 2010; Rameau et al., 2013a). The final 5σ contrast maps were obtained using the pixel-to-pixel noise maps divided by the flux loss and normalized by the relative calibration with the primary star, and were also corrected from small number statistics following the prescription of Mawet et al. (2014) to adapt our 5σ confidence level at small angles. The 5σ contrast maps were then converted to mass maps based on the COND model predictions (Baraffe et al., 2003) where the star’s age, distance, and magnitude (reported in Table 2.2) are considered for the luminosity-mass conversion. The azimuthal median of the contrast and mass maps for all our targets with the sADI algorithm are reported in Fig. 3.1.

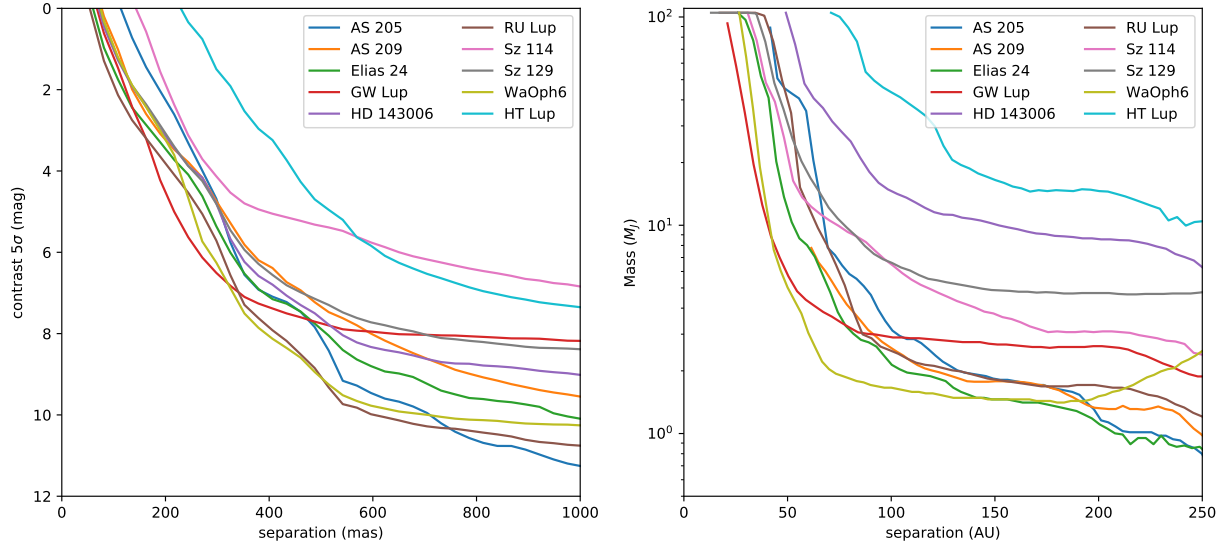


Figure 3.1: 5σ contrast and mass limits for possible companions obtained using the sADI algorithm as a function of separation for all the targets in our sample. Conversion from magnitude to mass were obtained based on COND model predictions and the age, distance and L' magnitude of the host stars presented in Table 2.2

As can be seen, both the 5σ contrasts and corresponding mass limits vary depending on the specific system, although some common results can be derived. For the majority of the sample a 2 magnitude contrast limit can be obtained at a projected separation of $\approx 0.1''$, increasing to a 4 magnitude contrast limit at $\approx 0.2''$. At further separations the limits start to differ depending on each target, mostly due to the difference on the physical properties of the systems. Translated to mass, the detection of a $10M_{Jup}$, which is considered the upper mass limit for a planetary object formed via core accretion (Schlaufman, 2018), is only possible at a separation of ≈ 50 AU for the more optimistic cases corresponding to GW Lup and WaOph 6, indicating that it is extremely difficult to resolve a planetary companion at shorter separations for any of the objects of the sample.

3.2. Detection Probability Maps

The derived detection limits gives us the minimum necessary contrast and mass for a planet to be detectable at different separations from the host star. However, it is also useful to study the detection probability for a range of masses at a given location, as it allows, for example, to compare with the specific predictions from hydrodynamical simulations of the disks.

We obtain detection probability maps for eight targets of our sample. The binary systems HT Lup and AS 205 were not considered for different reasons; in the case of HT Lup it was not possible to obtain enough rotation of the FOV to make it an appropriate case for this analysis. On the other side, AS 205 was discarded due to the brightness of the stellar

companion, which makes it impossible to resolve the signal of a planetary companion at near locations, which is crucial for the following process.

The detection probability maps for the remainder of the sample were derived by using the Multi-purpose Exoplanet Simulation System (MESS) code, a Monte Carlo tool for the predictions of exoplanet search results (Bonavita et al., 2012). We generated a uniform grid of mass and semi-major axis in the interval $[0.5, 80] M_{Jup}$ and $[10, 1000]$ AU with a sampling of $0.5 M_{Jup}$ and 1 AU respectively. For each point in the grid, 10^4 orbits were generated with a fixed inclination and position angle, Ω (based on the inclination and position angle of the observed annular structures of the disk from Huang et al., 2018a), but randomly oriented in space from uniform distributions in $\omega, e < 0.1$ and M , which correspond to the argument of periastron with respect to the line of nodes, eccentricity, and mean anomaly, respectively. Each combination of ω, e and M , produces a different projected orbit. The detection probability maps are then built by counting the number of detected planets over the number of generated ones, by comparing the on-sky projected position (separation and position angle) of each synthetic planet with the 2D mass maps at 5σ . The resulting detection probability maps are reported in Fig. 3.2, where the known gaps location is highlighted. As can be seen in the figure, detections are not possible at the inner (< 50 AU) regions of the disks. However, at larger separations the probability of a detection increases considerably, with over a 50% probability for masses around $3 - 5 M_{Jup}$ in most cases.

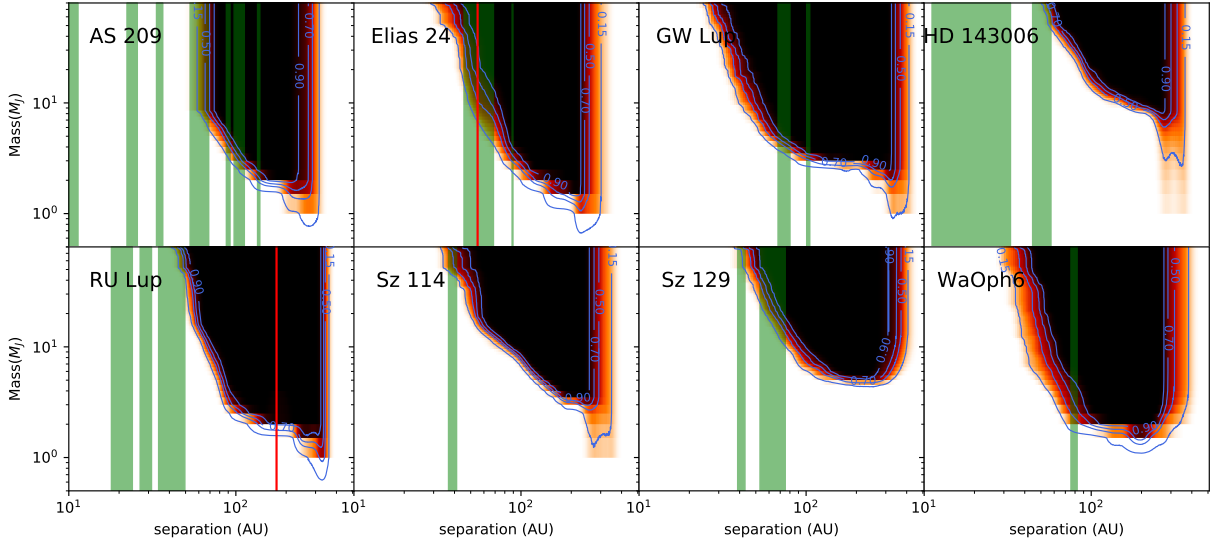


Figure 3.2: Detection probability maps for the single-star targets in our survey. Shaded green regions correspond to the location and width of the observed gaps of the disks, as derived by Huang et al. (2018a). Red lines indicate the location of the point sources presented in this work for Elias 24 and RU Lup. Our mass contrast limits are based on COND model predictions. In all cases, detection probability increases with both separation and mass, having a 50% probability for masses $\sim 5M_{Jup}$ at ≈ 100 AU around almost all targets.

Chapter 4

Point-source detections

The analysis presented in this chapter is part of a paper titled “A search for companions via direct imaging in the DSHARP planet-forming disks” by Jorquera et al. 2020 (Accepted by AJ).

Of the ten analysed systems, only RU Lup and Elias 24 exhibit a point like signal in our ADI reduction. Their signal appears consistently on all ADI processing methods, as shown in Fig. 4.1 and 4.2, supporting the idea that we are in the presence of a real detection. Further analysis is then carried out for each object, aiming to characterize the properties of the possible companions.

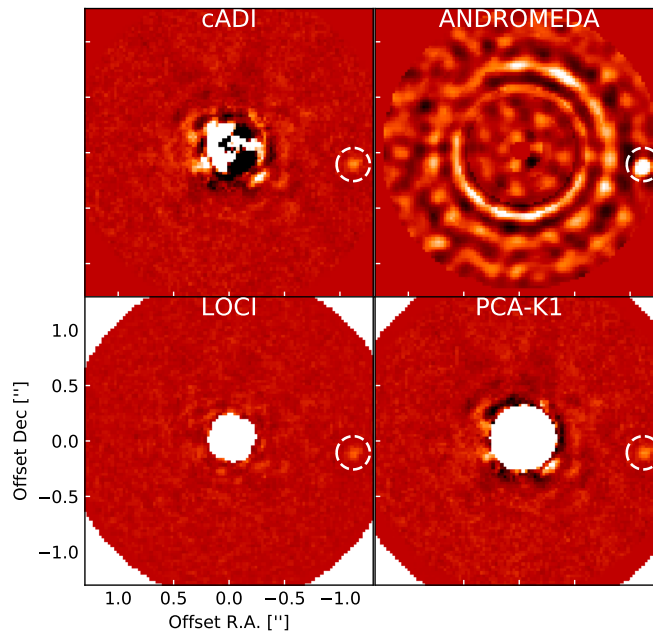


Figure 4.1: L' band images for RU Lup after processing using four different ADI algorithms. An additional reduction using the ANDROMEDA algorithm (Cantalloube et al., 2015) was performed as a test for the detection. A point source is recovered at the same position, marked with a circle, for all algorithms.

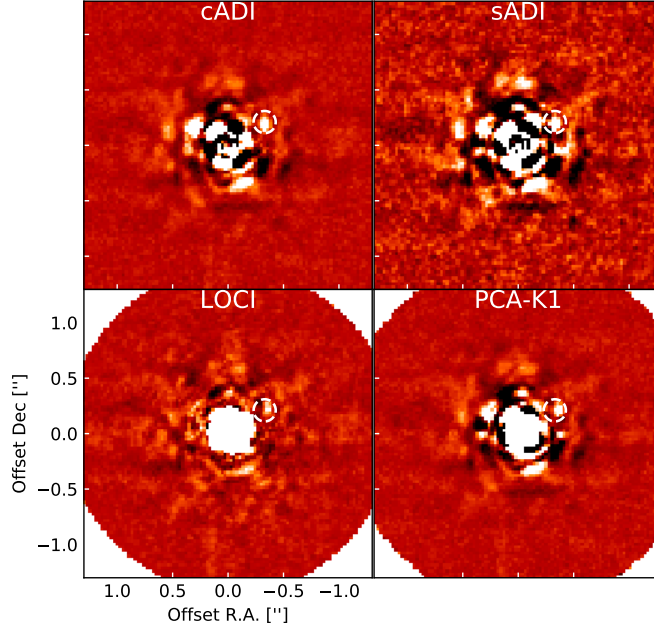


Figure 4.2: L' band images for Elias after processing using four different ADI algorithms. A point source is recovered at the same position, marked with a circle, for all algorithms.

4.1. RU Lup

The detected point source was first reported by Avenhaus et al. (2018) using H band observations obtained with the SPHERE/IRDIS instrument on the VLT. It was regarded to be most likely a background object, although further discussion was not provided.

To characterize the position of the companion, negative fake planets were injected one by one spanning a three dimensional parameter space (X position, Y position and flux) on the data cube before the PSF subtraction. The cube was then reprocessed to derive the best-fit solution that minimize the residuals in the final subtracted image. This process located the companion at a separation of $1.112 \pm 0.008''$ (174 AU) and a position angle of $263.97 \pm 0.46^\circ$, relative to the host star of the system. In addition to the fake planet injection uncertainties, we considered additional errors coming from the central star position (saturated core, < 0.3 pixels), and the plate scale and True North calibration reported in Chapter 2.

To test if the detection is in fact that of a planetary companion, we derive the astrometry of the object by using archival data from 2016 and 2017 of the same source (C. Ginski, priv. communication). The results, displayed in Fig. 4.3, indicate that the object is unambiguously not comoving with the primary star, with its astrometry being more consistent with that of a stationary background object. We still note a difference with the stationary background prediction, already present in the SPHERE measurements and confirmed with the NaCo third epoch, which suggests that the detected point-source has not a null proper motion.

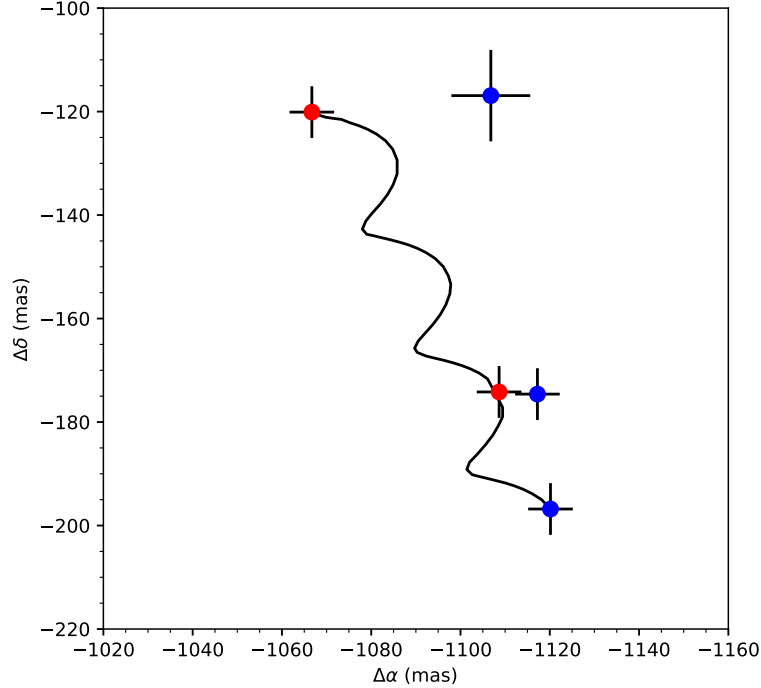


Figure 4.3: Relative astrometry for the point-source detected in RU Lup, at three different epochs, from bottom to top: March-2016, March-2017 and May-2019. The predicted motion of a comoving object follows the black line, with the red dots being the expected astrometry of a comoving object at the different epochs of the observations. Blue dots are the real astrometry of the observed point-source at the different epochs of the observations. Error bars are obtained by propagation of errors, considering the intrinsic error of 0.2 pixels for star centering, the True North and plate scale error of the instrument, and the error of the position fitting for the observed point source.

4.2. Elias 24

In this case, the location of the point source is both extremely interesting and challenging. Following the same procedure as for the companion observed in the case of RU Lup, we locate the source at a separation of $0.411 \pm 0.008''$ (~ 55 AU) and a position angle of $302.1 \pm 1.14^\circ$. This result locates the source within one of the observed gaps of the disk, as can be seen in Fig. 2.3. It has been proposed that the annular structures in the disk formed due to the presence of a planetary companion at this location (Cieza et al., 2017; Dipierro et al., 2018; Zhang et al., 2018), supporting the possibility that the detected signal could be evidence of a planet-forming in the disk. At the same time, our ADI observations start degrading at close separations in the inner region of the disk, as evidenced by the presence of artifacts that can be observed at separations similar to the alleged signal. Because of this, multiple tests were carried out to determine the possibility of it being a true detection. However, it was not possible to do the same astrometry comparison as it was done for RU Lup, since no previous detections of this source exist.

A first approach was to divide the original observing sequence into two, ensuring enough

rotation of the field of view for the ADI algorithms to correctly process the images. In both sequences, the point-like signal was recovered at the same location for all the ADI methods used. A second test consisted on the injection of fake planets in the original data cube before the PSF subtraction. Fake planets were positioned at similar separations but different position angles (0° , 90° and 180°) than the original signal. The cube was then processed using all ADI algorithms, to check if it was possible to recover the signal from the injected planets at the given separation. All the fake planets were recovered after the processing, producing similar point-like features as the original signal. The aforementioned tests strongly support the possibility that this detection could be of an actual planetary companion and not an speckle or other processing induced artifact. Another point to take into account is that first ADI detections of exoplanets using the NaCo instrument have been reported with a quality very similar to the ones obtained for Elias 24 (e.g, Lagrange et al., 2009; Keppler et al., 2018), indicating that it is still possible to recover the signal of a faint companion even at separation with a strong presence of residual artifacts after the data processing.

The process used to estimate the location of the point source also allows us to estimate the flux of the signal, as we also determine the flux that minimizes the signal of the companion after the reduction. By using the photometry of the signal together with the distance and L' magnitude of the host star, as reported on Table 2.2, we are able to derive its L' magnitude contrast. We derived the contrast to be 8.81 ± 0.12 mag. The age of the star is then considered in order to compare the measured magnitude contrast with the contrast expected for the appropriate isochrone of planetary evolution derived by Baraffe et al. (2003). This results in an estimated mass of $\sim 5M_{Jup}$ for the possible planet.

Given our preliminary results, a new set observations on Elias 24 was carried out on September 2019, to confirm the preliminary signal. New observations could not be carried out in an identical setup, due to the closeness to the decommissioning date of NaCo and since the target was not optimal to be observed during transit. Thus, we opted for an RDI approach, as more relaxed observational constraints can be set to carry out these observations. Fig 4.4 shows the resulting image for the second epoch after RDI processing, compared with the cADI results from the first epoch. In this case the previously reported signal was not recovered. However, it has to be considered that the results obtained with the RDI processing are harder to interpret than the ADI results at the estimated location of the point-like source, given the numerous artifacts that remain after the data reduction, together with the fact that the gap is located very close to the inner limit of the region that can be resolved with RDI, thus difficulting the detection of a signal at that separation. Based on this, further follow-up is mandatory to clarify the status of this faint planet candidate.

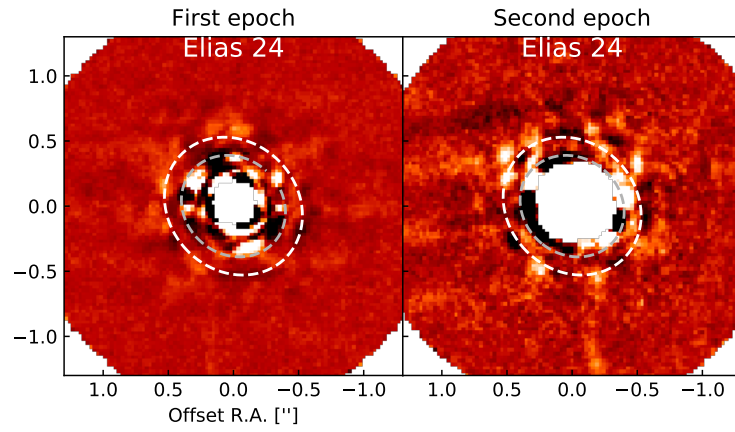


Figure 4.4: Comparison of the two different epochs of observation of Elias 24, using the PCA method. The same color scale is used for both observations. The signal of the possible companion was not recovered again during the second epoch, which was reduced using the RDI method.

Chapter 5

Discussion

5.1. Planet-Disk interaction

Assuming that the observed annular structures in our sample originate from the dynamical interaction between the disk and a forming planet, it is then necessary to analyze how our results, from both the detection and non-detection cases, correlate with the constraints on the system properties derived by different models of planet-disk interaction.

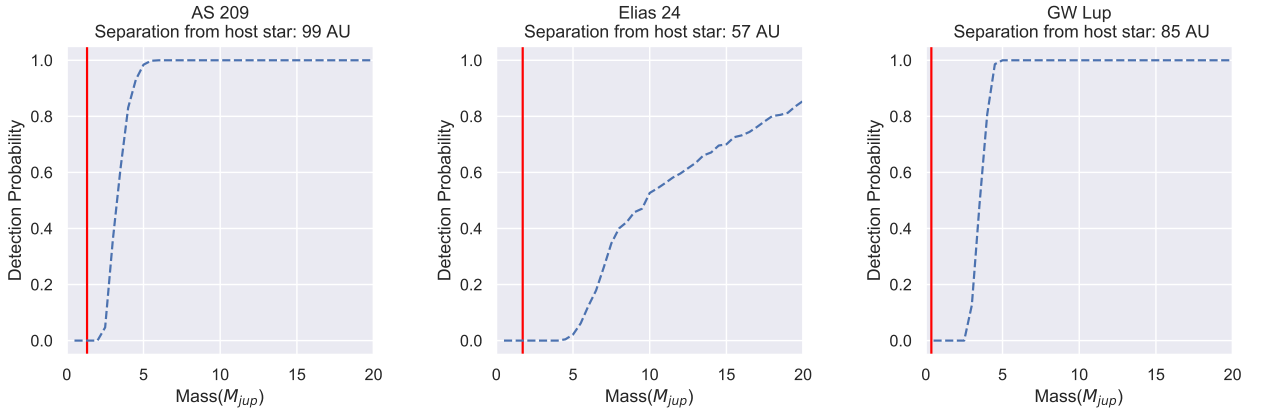


Figure 5.1: Cut of our MESS Detection probabilities at the possible planet locations considered by Zhang et al. (2018). Red vertical lines mark the highest mass needed for a planet to produce the observed gaps in the disk, as predicted by the hydrodynamical models.

From Fig 3.1 and 3.2, one can observe that the separations at which detections are possible vary depending on each particular target, with the closest distance being between 50-80 AU for a $10M_{Jup}$ object, depending on the target. However, at distances > 100 AU, we have a detection probability over 50% for planets with masses around $5 - 10M_{Jup}$, for almost all of our sample. Based on our non-detections, we can preliminary rule out the presence of high mass companions ($> 5M_{Jup}$) at these separations.

Different studies have shown that both the disks properties and the mass of a planetary companion embedded are closely linked to the final morphology and substructures of the disk. For example, Bae et al. (2018) found that a Jupiter-mass planet can produce different

disk morphologies depending on the viscosity of the disk and its grain size distribution. Similarly, Zhang et al. (2018) found from hydrodynamical simulations that companions with different masses can produce the structures observed on the disks of the DSHARP sample, depending on the disk surface density, viscosity and dust size distribution. A link between the companion properties and the morphology of the disk was also derived by Lodato et al. (2019), who inferred planetary masses of possible companions based on the width of the gaps of different planet-forming disks observed by ALMA, which were consistent with the mass estimations derived from hydrodynamical models.

Three of our observed targets were also modeled by Zhang et al. (2018): AS 209, Elias 24 and GW Lup. We can then compare our MESS results for the derived detection probabilities for these targets with the planetary masses and disk properties estimated by the hydrodynamical simulations. In Fig 5.1 we present our inferred detection probabilities for companions at the locations where hydrodynamical models from Zhang et al. (2018) require the presence of a planet to generate the observed gaps. For GW Lup, the highest estimated mass from hydro modeling for a companion is $0.06M_{Jup}$. However, it is also mentioned that this value could increase up to $0.36M_{Jup}$ if the gaps observed at 74 and 103 AU are part of a wide gap separated by a horseshoe region. In any case, the estimated mass is too low to be detected by our ADI observations. This is the same for AS 209, where the highest mass for a planet derived from the models is $1.32M_{Jup}$. The case of Elias 24 is similar, as it is not possible to detect even the higher mass planet ($1.7M_{Jup}$) predicted by the models. For a mass of $5M_{Jup}$, as the one derived in section 4.2 for the observed signal, we obtain a detection probability of $\sim 5\%$. Although it is still a low value, it might still be compatible with the one of a real planetary mass companion. For other targets, it was not possible to resolve the inner regions of the disk where the dark gaps have been observed, so it is not possible to compare with theoretical predictions as no constraints in the companion masses can be derived at those close-in separations. However, the derived detection probabilities for all the disks in the sample do not take into account the possible presence of a circumplanetary disk (CPD), which might alter these values, although to an unknown extent (see section 5.2 for further discussion).

An alternative method to detect and characterize planetary companions in planet-forming disks is to search for their kinematic signatures in the gas emission. Normally, for a given velocity channel, gas emission is concentrated along a Keplerian iso-velocity curve, corresponding to the region of the disk where the projected velocity is equal to the channel velocity and which is consistent with Keplerian rotation of the gas. However, the presence of a planet in the disk can distort the iso-velocity curve, producing a distinctive "kink" in the emission. Hydrodynamical models can then be used to reproduce the observed kinks considering an embedded planet in the disk, allowing for an estimation of the mass of the possible companion depending on the magnitude of the deviation observed. This technique has proven useful, as it has led to detections of kinks that may be associated with massive planets in the disks surrounding HD163296 (Pinte et al., 2018) and HD97048 (Pinte et al., 2019). Pinte et al. (2020) reported the detection of kinematical signatures in nine disks from the DSHARP sample, using ^{12}CO J=2-1 emission observations.

Four of these objects were also observed here: HD 143006, GW Lup, Sz 129 and WaOph 6. In all cases, the location of the velocity "kink" is consistent with the location of the gaps observed in the continuum emission of these disks, as shown in Fig. 5.3, suggesting that a

significant fraction of the observed structures are caused by embedded protoplanets. Due to the velocity resolution of the observations, Pinte et al. (2020) cannot properly determine the mass of the possible perturber. Instead, ranges of masses from $1M_{Jup}$ to $3M_{Jup}$ were estimated for almost all cases, with the exception of HD 143006, whose velocity deviation is significantly larger, pointing to a more massive planet. Depending on the case, Pinte et al. (2020) argues that mass estimations can range from 4 up to 10 times larger than the masses derived from the hydrodynamical models of Zhang et al. (2018) and Lodato et al. (2019), giving them a higher probability of being detected by direct imaging, based on Fig 3.2. In Fig 5.2 we present our derived detection probabilities at the location of the gaps for the cases of GW Lup, Sz 129 and WaOph 6. HD 143006, which was reported Pinte et al. (2020) as containing kinematic signatures possibly linked to a planetary companion, was not included, as it is not possible to resolve the region where the planet is expected to lie, at a separation of 22 AU from the host star. For Sz 129, the estimated planet mass from the observed kinks is still too small to be detected in our ADI observations, as only objects with masses higher than $11M_{Jup}$ are expected to be observable with any probability. The best options for a direct detection of a companion is then WaOph 6, which has a detection probability of $\sim 70\%$ for planets with $3M_{Jup}$. In the case of GW Lup it is not possible to detect a planet with a mass lower than $3M_{Jup}$, as can be seen in Figure 5.2, although the pronounced increase in the detection probability between $3M_{Jup}$ and $5M_{Jup}$ makes it an interesting case for future searches of companions within this mass range. The fact that no signal of a possible companion was recovered after the ADI processing suggest the presence of planet with masses lower than $3M_{Jup}$.

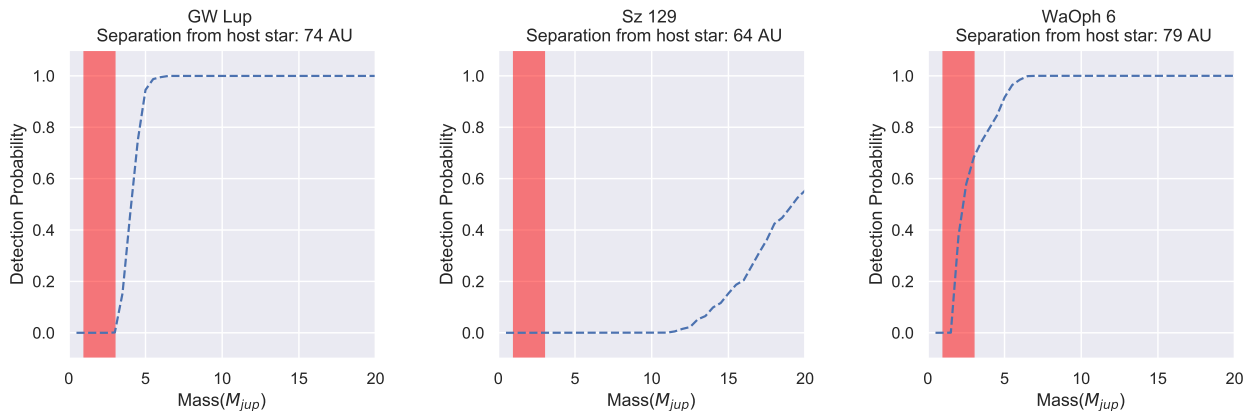


Figure 5.2: Cut of our MESS Detection probabilities at the possible planet locations obtained by Pinte et al. (2020). Red shaded intervals correspond to the mass range $1M_{Jup} - 3M_{Jup}$. In the three cases, planets location is consistent with the radius of one of the disk gaps.

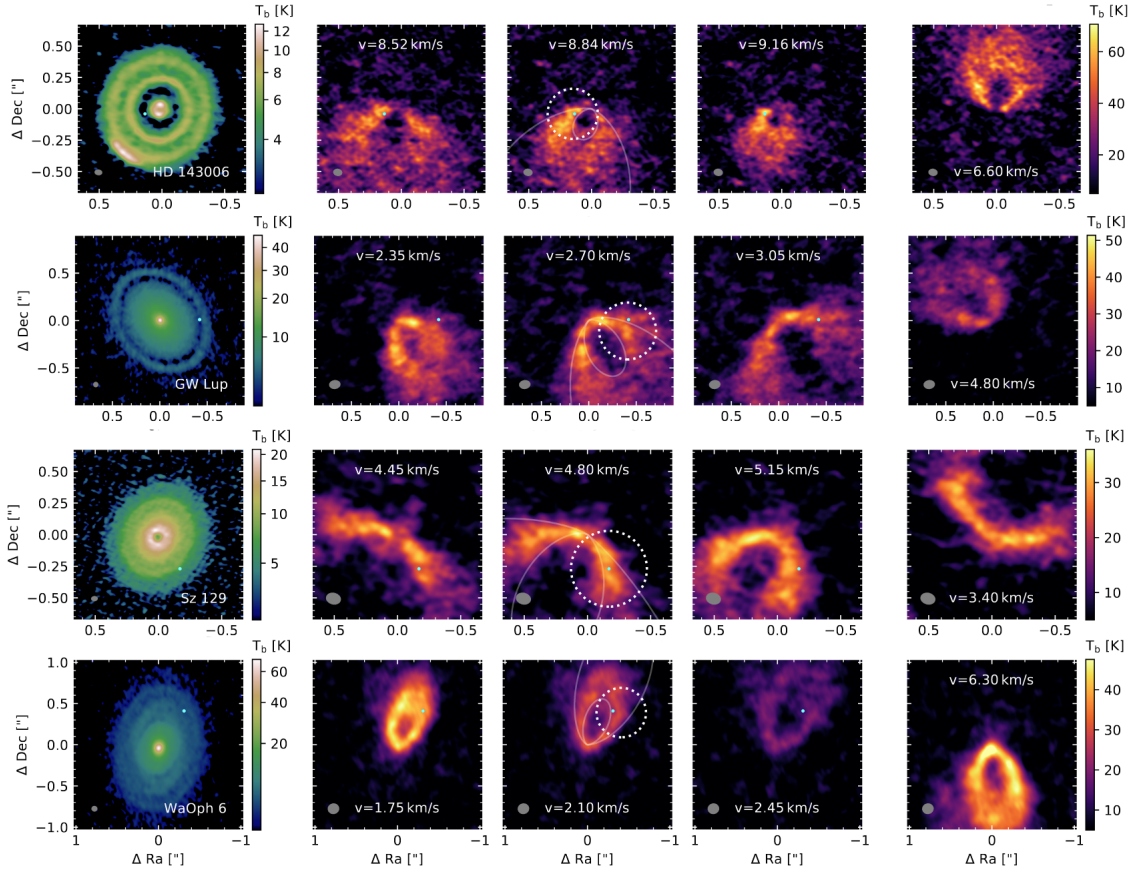


Figure 5.3: Candidate velocity kinks detected in the ^{12}CO $J=2-1$ DSHARP data. Dashed circles indicate the velocity kinks, and the cyan dots the location of the planet assuming it is in the disk midplane. Solid lines in the third column indicate the expected location of the isovelocity curves at $\pm 0.2v_{Kep} \sin i$, where v_{Kep} is the Keplerian velocity at the location of the planet and i the disk inclination. From Pinte et al. (2020)

The lack of detections of high mass planets at the location of the gap and even further away also gives important insight into the origin of the observed spiral arms in the disk of WaOph 6. Huang et al. (2018b) discussed the possibility of this spiral features to be created due to a planetary perturber located outside the arms, which extend up to 75 AU, and with a mass of several Jupiter masses. If that is the case, we should expect to recover the signal of these companions after the ADI processing based on the detection probabilities on Figure 3.2, which reveal that we are sensitive to the detection of high mass planets at these regions. Although follow-up observations of this target are needed to definitely rule out the presence of a massive companion, as well as to check for possible planets with masses below our derived detection limits, this suggests that for WaOph 6, the spiral arms might not be triggered by interaction with a massive companion, and other alternatives should be considered such as formation due to gravitational instabilities.

5.2. Circumplanetary disk effects

Taking into account the young age of the sample ($\leq 10\text{Myr}$), combined with the derived planet masses that are consistent with the formation of the observed annular substructures (Zhang et al., 2018), it is expected that the planetary companions forming inside the DSHARP disks are on relatively early evolutionary stages, when protoplanets are still actively accreting. If that is the case, it is expected that the accreted material will form a circumplanetary disk that will surround the planet (CPD; Quillen and Trilling, 1998; Lubow et al., 1999; Papaloizou and Nelson, 2005; Ayliffe and Bate, 2009, 2012; Mordasini et al., 2012). Any attempt to observe the forming protoplanets will then not only capture the emission from the planet, but from the CPD as well, making it crucial to address how the presence of a CPD impacts on both the detection and characterization of these systems.

CPDs are expected to be very bright at infrared wavelengths, specially at the L'-band (Eisner, 2015; Zhu, 2015; Szulágyi et al., 2019), with its luminosity even surpassing that from the protoplanet. Because of this, the total emission of the CPD-planet system could mimic the one derived from evolutionary models for planets with masses up to an order of magnitude higher than the protoplanet real mass (Szulágyi et al., 2019). Although this increased brightness can make these systems easier to detect, exact determination of their physical properties remains an extremely difficult challenge due to the multiple different phenomena CPDs are subjected to, such as the effects of magnetic fields (Gressel et al., 2013; Turner et al., 2014; Keith and Wardle, 2015; Pérez et al., 2016), accretion outbursts (Lubow and Martin, 2012), episodic infall of material from the planet-forming disk (Gressel et al., 2013), and radiative feedback from the protoplanet (Montesinos et al., 2015; Gárate et al., 2017). Given that all of these processes play an important role on the final architecture and emission of the CPD, and since they can differ for each particular target, it is essential to study each system individually to properly characterize it.

A possible method to derive the properties of these systems is to use the relation of its apparent magnitude, which can be obtained from observations, with other properties such as its mass and accretion rate. It has been found that the brightness of these systems might be directly linked to the product of the planet mass and the mass accretion rate ($M_p\dot{M}$) as well as the CPD inner radius, R_{in} , (Zhu, 2015; Mordasini et al., 2017). Thus, the contrast of a detected companion can be used to derive the value of $M_p\dot{M}$ for each particular system. This information can then be used to run system-specific disk models, aiming to reproduce both the signal of the companion and the structures observed on the planet-forming disk. With these results, it is then possible to determine, or at least constrain, properties such as the mass or temperature of both the CPD and the embedded protoplanet for each particular system.

The case of the point-source observed on the gap of Elias 24 can be used to illustrate the previously mentioned method. Based on the derived contrast of the signal, we estimate its apparent magnitude to be $L' = 15.4 \pm 0.14$. Assuming the distance of 136 pc reported in Table 2.2, its absolute magnitude is $L' = 9.73 \pm 0.14$. This magnitude is then compared with the results from Zhu (2015), allowing to obtain three possible values of $M_p\dot{M}$ with an Absolute L' magnitude consistent with the value derived for the observed source. Finally, these values of $M_p\dot{M}$ are used to obtain an estimate of the accretion rates associated with the mass

predictions from the hydrodynamical models of Zhang et al. (2018) and the mass derived in Sect. 4.2. The minimum mass is set at $0.4M_{Jup}$, as derived from Zhang et al. (2018). Two values are considered for the maximum masses; $1.72M_{Jup}$, which is the highest mass predicted by the hydrodynamical models, and $5M_{Jup}$ which is the mass derived from evolutionary models based on the luminosity of the source. The predicted accretion rates are reported in Table 5.1. For the ranges of masses and CPD inner radii we consider, the planet accretion rate inferred (from $1.2 \times 10^{-7}M_{Jup}yr^{-1}$ up to $1.5 \times 10^{-5}M_{Jup}yr^{-1}$) indicate a reasonable, low to moderate, growth for the posited planet. Future observations and dedicated hydro simulations are needed to confirm and further characterize the nature and the properties of the observed point-source in Elias 24.

Table 5.1: Mass ranges and accretion rates based on the results from Zhu (2015). Three possible models of a planet plus a CPD are consistent with the derived L' magnitude of the point like source, considering the derived error of 0.14 mag and the distance uncertainties to the host star. The columns are ordered as follows: Column 1: Expected L' magnitude from the CPD models. Column 2: Expected value of $M_p\dot{M}$ from the CPD models. Column 3: CPD inner radius. Column 4: Companion mass range. Column 5: Accretion rates associated with the minimum and maximum mass of the planet, respectively.

L'	$M_p\dot{M}$	R_{in}	Mass	Accretion rate
(mag)	($M_J^2yr^{-1}$)	(R_J)	(M_{Jup})	($M_{Jup}yr^{-1}$)
9.8	6×10^{-6}	4	0.4 / 1.72 / 5	1.5×10^{-5} / 3.5×10^{-6} / 1.2×10^{-6}
9.8	10^{-6}	2	0.4 / 1.72 / 5	2.5×10^{-6} / 5.8×10^{-7} / 2×10^{-7}
9.5	6×10^{-7}	1	0.4 / 1.72 / 5	1.5×10^{-6} / 3.5×10^{-7} / 1.2×10^{-7}

The existence of a CPD can be inferred by other tracers than a potential overluminosity in infrared. A spectrum may actually reveal the presence of circumplanetary material significantly contributing to the total spectral energy distribution in addition to the planet's atmospheric emission as proposed for PDS70b combining SPHERE, NaCo and SINFONI observations at VLT (Christiaens et al., 2018; Cheetham et al., 2018; Müller et al., 2018). Shocks on the CPD surface can arise from meridional accretion flows (Tanigawa et al., 2012; Morbidelli et al., 2014; Szulágyi et al., 2014; Dong et al., 2019), which happen at near free-fall speed and heat the gas to thousand of Kelvin, theoretically producing strong H_α emission (Aoyama et al., 2018). H_α high-contrast imaging can then be used as an alternative technique to observe these systems. Surveys using this method have already been carried out with MagAO/VisAO, VLT/ZIMPOL and MUSE (e.g; Close et al., 2014; Huélamo et al., 2018; Cugno et al., 2019; Haffert et al., 2019; Zurlo et al., 2020) as well as observation on particular targets, producing interesting results such as a successful H_α detection at the same location as the imaged protoplanets PDS70b and c (Wagner et al., 2018; Haffert et al., 2019). They definitively offer a rich perspective to explore the physics of accretion (accretion rate, variability) during the formation of young giant planets in addition to their discoveries.

CPDs can be potentially detected also at longer wavelengths, such as the sub-millimetre regime. Zhu et al. (2018) found from multiple different models of CPDs that radio observations of these systems are more sensitive at shorter wavelengths, which in the case of ALMA are possible at Band 7 or above. Similarly, Szulágyi et al. (2018) propose that the best option is to use Band 9 observations with the ALMA instrument to detect these systems, which

allows to obtain fluxes up to 2 times higher than the flux detected in any other band. Furthermore, high resolution imaging at long wavelengths aiming to detect circumplanetary disks have already been carried out, with the most promising result being the detection of a third planetary companion orbiting the system PDS70 (PDS70c; Isella et al., 2019). These results strongly support the use of radio observations as an alternative method to detect planetary companions.

5.3. Extinction from planet-forming disk material

Finally, it is important to point out that the contrast values, and subsequently the detection probability maps, derived from our observations might be optimistic estimates, since we are not considering the effects of the disk material on the planets infrared emission. The presence of dust grains between the mid-plane of the disk, where the planet is expected to form, and its surface layer is expected to reduce the observed brightness of a source embedded into the disk, due to absorption and scattering from this solid material (Quanz et al., 2015; Maire et al., 2017). This implies that higher magnitude contrasts, and hence higher masses, may be needed for a planet to be detected via direct imaging when dust effects are considered.

Sanchis et al. (2020) derived the effect of extinction due to disk dust for multiple planet masses, separations from the host star, and IR bands. They found that for a $5M_{Jup}$ planet, extinction almost does not affect any IR band at any separation, since the planet is extremely efficient at removing the dust content along its orbit, opening a deep gap. On the other hand, it was found that for planets with masses below $5M_{Jup}$, which seems to be the case of our sample based on our non-detections, dust extinction increases as the planet mass or the separation to the host star decreases, with dust extinction effects being less dramatic for longer IR wavelengths. Since the resolved regions after the ADI processing of our L' observations correspond to distances where dust extinction is supposed to be low ($\geq 50AU$), and that L-band is one of the bands less affected by extinction, we could expect that the derived detection limits will not vary much due to presence of dust near the planet.

Chapter 6

Conclusion

We present the first attempt to directly image planetary companions embedded into planet-forming disks from the DSHARP sample, using angular differential imaging observations in thermal infrared. Our main results can be summarized as follows.

Observations of ten planet-forming disks were processed using multiple flavours of ADI algorithms. The resolved regions vary for each disk, with a separation limit ranging from 30 to 80 AU, allowing for the detection of planets on the outermost parts of the disk. Possible detections of companions are reported for two disk: RU Lup and Elias 24.

In the case of RU Lup, the possible companion is located at a separation of $\sim 1.1''$ (174 AU). Using archival data, the astrometry of the object was obtained for three different epochs, revealing it is not comoving with the host star of the disk. We conclude that it is in fact a stationary background object, being this the first time it is properly reported.

In the case of Elias 24, the observed point-like signal is located within one of the observed gaps of the disk, at a separation of $\sim 0.42''$ (55 AU). Two mass ranges are derived for the companion, based on different assumptions. Evolutionary models suggest the mass to be at least $5M_{Jup}$, while a lower mass of $0.5 M_{Jup}$ can be obtained when considering the presence of a CPD. Due to the challenging location of the signal, multiple tests were carried out to check for the possibility of it being an artifact induced by the reduction. Results from this tests seem to suggest that this is in fact a real detection.

A second set of images of Elias 24 was obtained as a follow-up based on the possible detection previously reported. In this case observation could only be processed using an RDI technique. The point-like signal was not recovered this time.

Contrast limits at 5σ were obtained in both magnitude and mass for each of the observed objects, as well as probability detection maps. These reveals that our observations are mostly sensitive to planets with masses $\geq 5M_{Jup}$ at large separations (≥ 100 AU).

Our detection limits and probabilities are compared with predictions on the companions masses based on both hydrodynamical simulations and kinematical signatures on the disk. In both cases the predicted masses are in good agreement with our results, since the putative companions would be too light and too faint to be detected in our survey. For WaOph 6, the lack of detections of high mass planets at the location of the gap or larger separations

suggest that the observed spiral features on the disk are not originated due to the interaction of a planetary companion and most likely arise from gravitational instabilities.

Implications on the existence of an already formed CPD surrounding the theorized planetary companion in the gap of Elias 24 is discussed. Based on the derived luminosity of the point-like source and an inferred mass for the planet of $0.4 - 5M_{Jup}$, we derived a range for the mass accretion rate of the system from $2 \times 10^{-8}M_{Jup}yr^{-1}$ up to $1.5 \times 10^{-6}M_{Jup}yr^{-1}$. In all studied cases this suggest a reasonable growth rate for the possible planet. Future observations and further modeling are needed to properly confirm if the observed signal is a real companion, if a CPD is surrounding the protoplanet, and to properly characterize this system.

6.0.1. Future work

Given our results, it is still too early to properly conclude if the observed structures on the disks are caused by the presence of planetary companions. Further attempts to observe these objects with more sensitive instruments, which will allow to go deeper in both contrast and location in the search of young planets, are currently in preparation. These multi-epochs observations are fundamental to determine the presence of a planet embedded into the disk via proper motion, and to derive its orbital properties, which will help to better understand the physical interaction between disks and planets, the evolution of planet-forming disks, and the processes of planetary formation and evolution.

With that in mind, we plan to continue the search and detection of planetary companions on the DSHARP planet-forming disks, by using multiple complimentary approaches and instruments. Observations with the MUSE instrument for 7 disk from the DSHARP sample were approved for period P106. These observations are aimed at the detection of H_α emission expected from the CPD of young planetary companions, as described in section 5.2. At the same time, observations with the SPHERE instrument of 15 disks from the same sample were also approved for period P106. These focus of these observations is the detection of companions by Direct Imaging, by using the same Angular Differential Imaging techniques described in this work, but also including a technique called Spectral Differential Imaging. Use of this instrument will allows us a greater sensitivity with respect to our NaCo observations, allowing for the detection of companions with lower masses and shorter separation from the host star.

Finally, a proposal was submitted for the JWST in an attempt to re-detect the source observed on Elias 24. These observations, in combination with the results presented in this work, will allow to confirm the nature of this object and to further constraint its physical and orbital properties in the case that it is, in fact, a real planetary companion.

Acknowledgements

This Thesis makes use of the following ALMA data: ADS/JAO.ALMA #2016.1.00484.L, ADS/JAO.ALMA #2011.0.00531.S, ADS/JAO.ALMA #2012.1.00694.S, ADS/JAO.ALMA #2013.1.00226.S, ADS/JAO.ALMA #2013.1.00366.S, ADS/JAO.ALMA #2013.1.00498.S, ADS/JAO.ALMA #2013.1.00631.S, ADS/JAO.ALMA #2013.1.00798.S, ADS/JAO.ALMA #2015.1.00486.S, ADS/JAO.ALMA #2015.1.00964.S. This thesis, and the work presented in Jorquera et al. 2020, has been partially funded by the National Agency for Research and Development (ANID), Scholarship Program, Magister Becas Nacionales/2019 - 22191721, by the ANID project Basal AFB-170002, from ANID FONDECYT Iniciación project #11181068, and from the National Aeronautics and Space Administration under grant No. 15XRP15_20140 issued through the Exoplanets Research Program.

Bibliography

- ALMA Partnership, C. L. Brogan, L. M. Pérez, T. R. Hunter, W. R. F. Dent, A. S. Hales, R. E. Hills, S. Corder, E. B. Fomalont, C. Vlahakis, Y. Asaki, D. Barkats, A. Hirota, J. A. Hodge, C. M. V. Impellizzeri, R. Kneissl, E. Liuzzo, R. Lucas, N. Marcelino, S. Matsushita, K. Nakanishi, N. Phillips, A. M. S. Richards, I. Toledo, R. Aladro, D. Broguiere, J. R. Cortes, P. C. Cortes, D. Espada, F. Galarza, D. Garcia-Appadoo, L. Guzman-Ramirez, E. M. Humphreys, T. Jung, S. Kamenon, R. A. Laing, S. Leon, G. Marconi, A. Mignano, B. Nikolic, L. A. Nyman, M. Radiszcz, A. Remijan, J. A. Rodón, T. Sawada, S. Takahashi, R. P. J. Tilanus, B. Vila Vilaro, L. C. Watson, T. Wiklind, E. Akiyama, E. Chapillon, I. de Gregorio-Monsalvo, J. Di Francesco, F. Gueth, A. Kawamura, C. F. Lee, Q. Nguyen Luong, J. Mangum, V. Pietu, P. Sanhueza, K. Saigo, S. Takakuwa, C. Ubach, T. van Kempen, A. Wootten, A. Castro-Carrizo, H. Francke, J. Gallardo, J. Garcia, S. Gonzalez, T. Hill, T. Kaminski, Y. Kurono, H. Y. Liu, C. Lopez, F. Morales, K. Plarre, G. Schieven, L. Testi, L. Videla, E. Villard, P. Andreani, J. E. Hibbard, and K. Tatematsu. The 2014 ALMA Long Baseline Campaign: First Results from High Angular Resolution Observations toward the HL Tau Region. , 808(1):L3, July 2015. doi: 10.1088/2041-8205/808/1/L3.
- Sean M. Andrews. Observations of Protoplanetary Disk Structures. , 58:483–528, August 2020. doi: 10.1146/annurev-astro-031220-010302.
- Sean M. Andrews, Katherine A. Rosenfeld, Adam L. Kraus, and David J. Wilner. The Mass Dependence between Protoplanetary Disks and their Stellar Hosts. , 771(2):129, July 2013. doi: 10.1088/0004-637X/771/2/129.
- Sean M. Andrews, Jane Huang, Laura M. Pérez, Andrea Isella, Cornelis P. Dullemond, Nicolás T. Kurtovic, Viviana V. Guzmán, John M. Carpenter, David J. Wilner, Shangjia Zhang, Zhaohuan Zhu, Tilman Birnstiel, Xue-Ning Bai, Myriam Benisty, A. Meredith Hughes, Karin I. Öberg, and Luca Ricci. The Disk Substructures at High Angular Resolution Project (DSHARP). I. Motivation, Sample, Calibration, and Overview. , 869(2):L41, Dec 2018. doi: 10.3847/2041-8213/aaf741.
- Yuhiko Aoyama, Masahiro Ikoma, and Takayuki Tanigawa. Theoretical Model of Hydrogen Line Emission from Accreting Gas Giants. , 866(2):84, October 2018. doi: 10.3847/1538-4357/aadc11.
- Philip J. Armitage. Dynamics of Protoplanetary Disks. , 49(1):195–236, September 2011. doi: 10.1146/annurev-astro-081710-102521.
- H. Avenhaus, S. P. Quanz, H. M. Schmid, C. Dominik, T. Stolker, C. Ginski, J. de Boer, J. Szulágyi, A. Garufi, A. Zurlo, J. Hagelberg, M. Benisty, T. Henning, F. Ménard, M. R. Meyer, A. Baruffolo, A. Bazzon, J. L. Beuzit, A. Costille, K. Dohlen, J. H. Girard, D. Gisler, M. Kasper, D. Mouillet, J. Pragt, R. Roelfsema, B. Salasnich, and J. F. Sauvage. Exploring

- Dust around HD 142527 down to 0.025 (4 au) Using SPHERE/ZIMPOL. , 154(1):33, Jul 2017. doi: 10.3847/1538-3881/aa7560.
- Henning Avenhaus, Sascha P. Quanz, Hans Martin Schmid, Michael R. Meyer, Antonio Garufi, Sebastian Wolf, and Carsten Dominik. Structures in the Protoplanetary Disk of HD142527 Seen in Polarized Scattered Light. , 781(2):87, February 2014. doi: 10.1088/0004-637X/781/2/87.
- Henning Avenhaus, Sascha P. Quanz, Antonio Garufi, Sebastian Perez, Simon Casassus, Christophe Pinte, Gesa H. M. Bertrang, Claudio Caceres, Myriam Benisty, and Carsten Dominik. Disks around T Tauri Stars with SPHERE (DARTTS-S). I. SPHERE/IRDIS Polarimetric Imaging of Eight Prominent T Tauri Disks. , 863(1):44, Aug 2018. doi: 10.3847/1538-4357/aab846.
- Ben A. Ayliffe and Matthew R. Bate. Gas accretion on to planetary cores: three-dimensional self-gravitating radiation hydrodynamical calculations. , 393(1):49–64, February 2009. doi: 10.1111/j.1365-2966.2008.14184.x.
- Ben A. Ayliffe and Matthew R. Bate. The growth and hydrodynamic collapse of a protoplanet envelope. , 427(3):2597–2612, December 2012. doi: 10.1111/j.1365-2966.2012.21979.x.
- Jaehan Bae, Paola Pinilla, and Tilman Birnstiel. Diverse Protoplanetary Disk Morphology Produced by a Jupiter-mass Planet. , 864(2):L26, Sep 2018. doi: 10.3847/2041-8213/aadd51.
- I. Baraffe, G. Chabrier, T. S. Barman, F. Allard, and P. H. Hauschildt. Evolutionary models for cool brown dwarfs and extrasolar giant planets. The case of HD 209458. , 402:701–712, May 2003. doi: 10.1051/0004-6361:20030252.
- M. Benisty, A. Juhasz, A. Boccaletti, H. Avenhaus, J. Milli, C. Thalmann, C. Dominik, P. Pinilla, E. Buenzli, A. Pohl, J. L. Beuzit, T. Birnstiel, J. de Boer, M. Bonnefoy, G. Chauvin, V. Christiaens, A. Garufi, C. Grady, T. Henning, N. Huelamo, A. Isella, M. Langlois, F. Ménard, D. Mouillet, J. Olofsson, E. Pantin, C. Pinte, and L. Pueyo. Asymmetric features in the protoplanetary disk MWC 758. , 578:L6, June 2015. doi: 10.1051/0004-6361/201526011.
- M. Benisty, T. Stolker, A. Pohl, J. de Boer, G. Lesur, C. Dominik, C. P. Dullemond, M. Langlois, M. Min, K. Wagner, T. Henning, A. Juhasz, P. Pinilla, S. Facchini, D. Apai, R. van Boekel, A. Garufi, C. Ginski, F. Ménard, C. Pinte, S. P. Quanz, A. Zurlo, A. Boccaletti, M. Bonnefoy, J. L. Beuzit, G. Chauvin, M. Cudel, S. Desidera, M. Feldt, C. Fontanive, R. Gratton, M. Kasper, A. M. Lagrange, H. LeCoroller, D. Mouillet, D. Mesa, E. Sissa, A. Vigan, J. Antichi, T. Buey, T. Fusco, D. Gisler, M. Llored, Y. Magnard, O. Moeller-Nilsson, J. Pragt, R. Roelfsema, J. F. Sauvage, and F. Wildi. Shadows and spirals in the protoplanetary disk HD 100453. , 597:A42, Jan 2017. doi: 10.1051/0004-6361/201629798.
- W. Benz, S. Ida, Y. Alibert, D. Lin, and C. Mordasini. Planet Population Synthesis. In Henrik Beuther, Ralf S. Klessen, Cornelis P. Dullemond, and Thomas Henning, editors, *Protostars and Planets VI*, page 691, Jan 2014. doi: 10.2458/azu_uapress_9780816531240-ch030.
- M. Bonavita, G. Chauvin, S. Desidera, R. Gratton, M. Janson, J. L. Beuzit, M. Kasper, and C. Mordasini. MESS (multi-purpose exoplanet simulation system). A Monte Carlo tool for the statistical analysis and prediction of exoplanet search results. , 537:A67, Jan 2012. doi: 10.1051/0004-6361/201116852.

- A. P. Boss. Giant planet formation by gravitational instability. *Science*, 276:1836–1839, Jan 1997. doi: 10.1126/science.276.5320.1836.
- L. Bourges, G. Mella, S. Lafrasse, G. Duvert, A. Chelli, J. B. Le Bouquin, X. Delfosse, and O. Chesneau. VizieR Online Data Catalog: JMMC Stellar Diameters Catalogue - JSDC. Version 2 (Bourges+, 2017). *VizieR Online Data Catalog*, art. II/346, January 2017.
- A. G. W. Cameron. Physics of the Primitive Solar Accretion Disk. *Moon and Planets*, 18(1): 5–40, Feb 1978. doi: 10.1007/BF00896696.
- F. Cantalloube, D. Mouillet, L. M. Mugnier, J. Milli, O. Absil, C. A. Gomez Gonzalez, G. Chauvin, J. L. Beuzit, and A. Cornia. Direct exoplanet detection and characterization using the ANDROMEDA method: Performance on VLT/NaCo data. , 582:A89, Oct 2015. doi: 10.1051/0004-6361/201425571.
- Simon Casassus and Sebastián Pérez. Kinematic Detections of Protoplanets: A Doppler Flip in the Disk of HD 100546. , 883(2):L41, October 2019. doi: 10.3847/2041-8213/ab4425.
- Simon Casassus, Gerrit M. van der Plas, Sebastian Perez, William R. F. Dent, Ed Fomalont, Janis Hagelberg, Antonio Hales, Andrés Jordán, Dimitri Mawet, Francois Ménard, Al Wootten, David Wilner, A. Meredith Hughes, Matthias R. Schreiber, Julien H. Girard, Barbara Ercolano, Hector Canovas, Pablo E. Román, and Vachail Salinas. Flows of gas through a protoplanetary gap. , 493(7431):191–194, January 2013. doi: 10.1038/nature11769.
- P. Cazzoletti, E. F. van Dishoeck, P. Pinilla, M. Tazzari, S. Facchini, N. van der Marel, M. Benisty, A. Garufi, and L. M. Pérez. Evidence for a massive dust-trapping vortex connected to spirals. Multi-wavelength analysis of the HD 135344B protoplanetary disk. , 619:A161, November 2018. doi: 10.1051/0004-6361/201834006.
- G. Chauvin, A. M. Lagrange, M. Bonavita, B. Zuckerman, C. Dumas, M. S. Bessell, J. L. Beuzit, M. Bonnefoy, S. Desidera, J. Farihi, P. Lowrance, D. Mouillet, and I. Song. Deep imaging survey of young, nearby austral stars . VLT/NACO near-infrared Lyot-coronagraphic observations. , 509:A52, Jan 2010. doi: 10.1051/0004-6361/200911716.
- G. Chauvin, A. M. Lagrange, H. Beust, M. Bonnefoy, A. Boccaletti, D. Apai, F. Allard, D. Ehrenreich, J. H. V. Girard, D. Mouillet, and D. Rouan. Orbital characterization of the β Pictoris b giant planet. , 542:A41, Jun 2012. doi: 10.1051/0004-6361/201118346.
- A. Cheetham, M. Bonnefoy, S. Desidera, M. Langlois, A. Vigan, T. Schmidt, J. Olofsson, G. Chauvin, H. Klahr, R. Gratton, V. D’Orazi, T. Henning, M. Janson, B. Biller, S. Peretti, J. Hagelberg, D. Ségransan, S. Udry, D. Mesa, E. Sissa, Q. Kral, J. Schlieder, A. L. Maire, C. Mordasini, F. Menard, A. Zurlo, J. L. Beuzit, M. Feldt, D. Mouillet, M. Meyer, A. M. Lagrange, A. Boccaletti, M. Keppler, T. Kopytova, R. Ligi, D. Rouan, H. Le Cooller, C. Dominik, E. Lagadec, M. Turatto, L. Abe, J. Antichi, A. Baruffolo, P. Baudoz, P. Blanchard, T. Buey, M. Carbillet, M. Carle, E. Cascone, R. Claudi, A. Costille, A. Delboulbé, V. De Caprio, K. Dohlen, D. Fantinel, P. Feautrier, T. Fusco, E. Giro, L. Gluck, N. Hubin, E. Hugot, M. Jaquet, M. Kasper, M. Llored, F. Madec, Y. Magnard, P. Martinez, D. Maurel, D. Le Mignant, O. Möller-Nilsson, T. Moulin, A. Origné, A. Pavlov, D. Perret, C. Petit, J. Pragt, P. Puget, P. Rabou, J. Ramos, F. Rigal, S. Rochat, R. Roelfsema, G. Rousset, A. Roux, B. Salasnich, J. F. Sauvage, A. Sevin, C. Soenke, E. Stadler, M. Suarez, L. Weber, and F. Wildi. Discovery of a brown dwarf companion to the star HIP 64892. , 615:A160, August 2018. doi: 10.1051/0004-6361/201832650.

- V. Christiaens, S. Casassus, O. Absil, S. Kimeswenger, C. A. Gomez Gonzalez, J. Girard, R. Ramírez, O. Wertz, A. Zurlo, Z. Wahhaj, C. Flores, V. Salinas, A. Jordán, and D. Mawet. Characterization of low-mass companion HD 142527 B. , 617:A37, September 2018. doi: 10.1051/0004-6361/201629454.
- Lucas A. Cieza, Simon Casassus, Sebastian Pérez, Antonio Hales, Miguel Cárcamo, Megan Ansdell, Henning Avenhaus, Amelia Bayo, Gesa H. M. Bertrang, Hector Cánovas, Valentin Christiaens, William Dent, Gabriel Ferrero, Roberto Gamen, Johan Olofsson, Santiago Orcajo, Axel Osses, Karla Peña-Ramirez, David Principe, Dary Ruíz-Rodríguez, Matthias R. Schreiber, Gerrit van der Plas, Jonathan P. Williams, and Alice Zurlo. ALMA Observations of Elias 2-24: A Protoplanetary Disk with Multiple Gaps in the Ophiuchus Molecular Cloud. , 851(2):L23, December 2017. doi: 10.3847/2041-8213/aa9b7b.
- L. M. Close, K. B. Follette, J. R. Males, A. Puglisi, M. Xompero, D. Apai, J. Najita, A. J. Weinberger, K. Morzinski, T. J. Rodigas, P. Hinz, V. Bailey, and R. Briguglio. Discovery of H α Emission from the Close Companion inside the Gap of Transitional Disk HD 142527. , 781(2):L30, February 2014. doi: 10.1088/2041-8205/781/2/L30.
- F. Comerón. *The Lupus Clouds*, volume 5, page 295. 2008.
- G. Cugno, S. P. Quanz, S. Hunziker, T. Stolker, H. M. Schmid, H. Avenhaus, P. Baudoz, A. J. Bohn, M. Bonnefoy, E. Buenzli, G. Chauvin, A. Cheetham, S. Desidera, C. Dominik, P. Feautrier, M. Feldt, C. Ginski, J. H. Girard, R. Gratton, J. Hagelberg, E. Hugot, M. Janson, A. M. Lagrange, M. Langlois, Y. Magnard, A. L. Maire, F. Menard, M. Meyer, J. Milli, C. Mordasini, C. Pinte, J. Pragt, R. Roelfsema, F. Rigal, J. Szulágyi, R. van Boekel, G. van der Plas, A. Vigan, Z. Wahhaj, and A. Zurlo. A search for accreting young companions embedded in circumstellar disks. High-contrast H α imaging with VLT/SPHERE. , 622:A156, February 2019. doi: 10.1051/0004-6361/201834170.
- R. M. Cutri and et al. VizieR Online Data Catalog: AllWISE Data Release (Cutri+ 2013). *VizieR Online Data Catalog*, art. II/328, January 2014.
- R. M. Cutri, M. F. Skrutskie, S. van Dyk, C. A. Beichman, J. M. Carpenter, T. Chester, L. Cambresy, T. Evans, J. Fowler, J. Gizis, E. Howard, J. Huchra, T. Jarrett, E. L. Kopan, J. D. Kirkpatrick, R. M. Light, K. A. Marsh, H. McCallon, S. Schneider, R. Stiening, M. Sykes, M. Weinberg, W. A. Wheaton, S. Wheelock, and N. Zacarias. VizieR Online Data Catalog: 2MASS All-Sky Catalog of Point Sources (Cutri+ 2003). *VizieR Online Data Catalog*, art. II/246, June 2003.
- Hans J. Deeg and Roi Alonso. *Transit Photometry as an Exoplanet Discovery Method*, page 117. 2018. doi: 10.1007/978-3-319-55333-7_117.
- G. Dipierro, L. Ricci, L. Pérez, G. Lodato, R. D. Alexander, G. Laibe, S. Andrews, J. M. Carpenter, C. J. Chandler, J. A. Greaves, C. Hall, T. Henning, W. Kwon, H. Linz, L. Mundy, A. Sargent, M. Tazzari, L. Testi, and D. Wilner. Rings and gaps in the disc around Elias 24 revealed by ALMA. , 475(4):5296–5312, Apr 2018. doi: 10.1093/mnras/sty181.
- Ruobing Dong, Sheng-yuan Liu, Josh Eisner, Sean Andrews, Jeffrey Fung, Zhaohuan Zhu, Eugene Chiang, Jun Hashimoto, Hauyu Baobab Liu, Simon Casassus, Thomas Esposito, Yasuhiro Hasegawa, Takayuki Muto, Yaroslav Pavlyuchenkov, David Wilner, Eiji Akiyama, Motohide Tamura, and John Wisniewski. The Eccentric Cavity, Triple Rings, Two-armed Spirals, and Double Clumps of the MWC 758 Disk. , 860(2):124, June 2018. doi: 10.3847/

1538-4357/aac6cb.

- Ruobing Dong, Sheng-Yuan Liu, and Jeffrey Fung. Observational Signatures of Planets in Protoplanetary Disks: Planet-induced Line Broadening in Gaps. , 870(2):72, January 2019. doi: 10.3847/1538-4357/aaf38e.
- Cornelis P. Dullemond, Tilman Birnstiel, Jane Huang, Nicolás T. Kurtovic, Sean M. Andrews, Viviana V. Guzmán, Laura M. Pérez, Andrea Isella, Zhaohuan Zhu, Myriam Benisty, David J. Wilner, Xue-Ning Bai, John M. Carpenter, Shangjia Zhang, and Luca Ricci. The Disk Substructures at High Angular Resolution Project (DSHARP). VI. Dust Trapping in Thin-ringed Protoplanetary Disks. , 869(2):L46, December 2018. doi: 10.3847/2041-8213/aaf742.
- J. A. Eisner. Spectral Energy Distributions of Accreting Protoplanets. , 803(1):L4, April 2015. doi: 10.1088/2041-8205/803/1/L4.
- II Evans, Neal J., Michael M. Dunham, Jes K. Jørgensen, Melissa L. Enoch, Bruno Merín, Ewine F. van Dishoeck, Juan M. Alcalá, Philip C. Myers, Karl R. Stapelfeldt, Tracy L. Huard, Lori E. Allen, Paul M. Harvey, Tim van Kempen, Geoffrey A. Blake, David W. Koerner, Lee G. Mundy, Deborah L. Padgett, and Anneila I. Sargent. The Spitzer c2d Legacy Results: Star-Formation Rates and Efficiencies; Evolution and Lifetimes. , 181(2): 321–350, April 2009. doi: 10.1088/0067-0049/181/2/321.
- D. Fedele, M. Carney, M. R. Hogerheijde, C. Walsh, A. Miotello, P. Klaassen, S. Bruderer, Th. Henning, and E. F. van Dishoeck. ALMA unveils rings and gaps in the protoplanetary system <ASTROBJ>HD 169142</ASTROBJ>: signatures of two giant protoplanets. , 600:A72, Apr 2017. doi: 10.1051/0004-6361/201629860.
- Katherine B. Follette, Carol A. Grady, Jeremy R. Swearingen, Michael L. Sitko, Elizabeth H. Champney, Nienke van der Marel, Michihiro Takami, Marc J. Kuchner, Laird M. Close, Takayuki Muto, Satoshi Mayama, Michael W. McElwain, Misato Fukagawa, Koen Maas-kant, Michiel Min, Ray W. Russell, Tomoyuki Kudo, Nobuhiko Kusakabe, Jun Hashimoto, Lyu Abe, Eiji Akiyama, Wolfgang Brandner, Timothy D. Brandt, Joseph Carson, Thayne Currie, Sebastian E. Egner, Markus Feldt, Miwa Goto, Olivier Guyon, Yutaka Hayano, Masahiko Hayashi, Saeko Hayashi, Thomas Henning, Klaus Hodapp, Miki Ishii, Masanori Iye, Markus Janson, Ryo Kandori, Gillian R. Knapp, Masayuki Kuzuhara, Jungmi Kwon, Taro Matsuo, Shoken Miyama, Jun-Ichi Morino, Amaya Moro-Martin, Tetsuo Nishimura, Tae-Soo Pyo, Eugene Serabyn, Takuya Suenaga, Hiroshi Suto, Ryuji Suzuki, Yasuhiro Takahashi, Naruhisa Takato, Hiroshi Terada, Christian Thalmann, Daigo Tomono, Edwin L. Turner, Makoto Watanabe, John P. Wisniewski, Toru Yamada, Hideki Takami, Tomonori Usuda, and Motohide Tamura. SEEDS Adaptive Optics Imaging of the Asymmetric Transition Disk Oph IRS 48 in Scattered Light. , 798(2):132, January 2015. doi: 10.1088/0004-637X/798/2/132.
- L. Fouchet, J. F. Gonzalez, and S. T. Maddison. Planet gaps in the dust layer of 3D protoplanetary disks. I. Hydrodynamical simulations of T Tauri disks. , 518:A16, Jul 2010. doi: 10.1051/0004-6361/200913778.
- Matías Gárate, Jorge Cuadra, and Matias Montesinos. Feedback-limited Accretion: Luminous Signatures from Growing Planets. *arXiv e-prints*, art. arXiv:1711.01372, November 2017.
- O. Gressel, R. P. Nelson, N. J. Turner, and U. Ziegler. Global Hydromagnetic Simulations

- of a Planet Embedded in a Dead Zone: Gap Opening, Gas Accretion, and Formation of a Protoplanetary Jet. , 779(1):59, December 2013. doi: 10.1088/0004-637X/779/1/59.
- Viviana V. Guzmán, Jane Huang, Sean M. Andrews, Andrea Isella, Laura M. Pérez, John M. Carpenter, Cornelis P. Dullemond, Luca Ricci, Tilman Birnstiel, Shangjia Zhang, Zhaohuan Zhu, Xue-Ning Bai, Myriam Benisty, Karin I. Öberg, and David J. Wilner. The Disk Substructures at High Angular Resolution Program (DSHARP). VIII. The Rich Ringed Substructures in the AS 209 Disk. , 869(2):L48, Dec 2018. doi: 10.3847/2041-8213/aaedae.
- S. Y. Haffert, A. J. Bohn, J. de Boer, I. A. G. Snellen, J. Brinchmann, J. H. Girard, C. U. Keller, and R. Bacon. Two accreting protoplanets around the young star PDS 70. *Nature Astronomy*, 3:749–754, June 2019. doi: 10.1038/s41550-019-0780-5.
- Jane Huang, Sean M. Andrews, Cornelis P. Dullemond, Andrea Isella, Laura M. Pérez, Viviana V. Guzmán, Karin I. Öberg, Zhaohuan Zhu, Shangjia Zhang, Xue-Ning Bai, Myriam Benisty, Tilman Birnstiel, John M. Carpenter, A. Meredith Hughes, Luca Ricci, Erik Weaver, and David J. Wilner. The Disk Substructures at High Angular Resolution Project (DSHARP). II. Characteristics of Annular Substructures. , 869(2):L42, Dec 2018a. doi: 10.3847/2041-8213/aaf740.
- Jane Huang, Sean M. Andrews, Laura M. Pérez, Zhaohuan Zhu, Cornelis P. Dullemond, Andrea Isella, Myriam Benisty, Xue-Ning Bai, Tilman Birnstiel, John M. Carpenter, Viviana V. Guzmán, A. Meredith Hughes, Karin I. Öberg, Luca Ricci, David J. Wilner, and Shangjia Zhang. The Disk Substructures at High Angular Resolution Project (DSHARP). III. Spiral Structures in the Millimeter Continuum of the Elias 27, IM Lup, and WaOph 6 Disks. , 869(2):L43, Dec 2018b. doi: 10.3847/2041-8213/aaf7a0.
- N. Huélamo, G. Chauvin, H. M. Schmid, S. P. Quanz, E. Whelan, J. Lillo-Box, D. Barrado, B. Montesinos, J. M. Alcalá, M. Benisty, I. de Gregorio-Monsalvo, I. Mendigutía, H. Bouy, B. Merín, J. de Boer, A. Garufi, and E. Pantin. Searching for H α emitting sources around MWC 758. SPHERE/ZIMPOL high-contrast imaging. , 613:L5, May 2018. doi: 10.1051/0004-6361/201832874.
- Andrea Isella, Jane Huang, Sean M. Andrews, Cornelis P. Dullemond, Tilman Birnstiel, Shangjia Zhang, Zhaohuan Zhu, Viviana V. Guzmán, Laura M. Pérez, Xue-Ning Bai, Myriam Benisty, John M. Carpenter, Luca Ricci, and David J. Wilner. The Disk Substructures at High Angular Resolution Project (DSHARP). IX. A High-definition Study of the HD 163296 Planet-forming Disk. , 869(2):L49, December 2018. doi: 10.3847/2041-8213/aaf747.
- Andrea Isella, Myriam Benisty, Richard Teague, Jaehan Bae, Miriam Keppler, Stefano Facchini, and Laura Pérez. Detection of Continuum Submillimeter Emission Associated with Candidate Protoplanets. , 879(2):L25, July 2019. doi: 10.3847/2041-8213/ab2a12.
- A. Johansen, A. Youdin, and H. Klahr. Zonal Flows and Long-lived Axisymmetric Pressure Bumps in Magnetorotational Turbulence. , 697(2):1269–1289, Jun 2009. doi: 10.1088/0004-637X/697/2/1269.
- Sarah L. Keith and Mark Wardle. Magnetic fields in gaps surrounding giant protoplanets. , 451(1):1104–1116, July 2015. doi: 10.1093/mnras/stv1029.
- M. Keppler, M. Benisty, A. Müller, Th. Henning, R. van Boekel, F. Cantalloube, C. Ginski, R. G. van Holstein, A. L. Maire, A. Pohl, M. Samland , H. Avenhaus, J. L. Baudino,

- A. Boccaletti, J. de Boer, M. Bonnefoy, G. Chauvin, S. Desidera, M. Langlois, C. Lazzoni, G. D. Marleau, C. Mordasini, N. Pawellek, T. Stolker, A. Vigan, A. Zurlo, T. Birnstiel, W. Brandner, M. Feldt, M. Flock, J. Girard, R. Gratton, J. Hagelberg, A. Isella, M. Janson, A. Juhasz, J. Kemmer, Q. Kral, A. M. Lagrange, R. Launhardt, A. Matter, F. Ménard, J. Milli, P. Mollière, J. Olofsson, L. Pérez, P. Pinilla, C. Pinte, S. P. Quanz, T. Schmidt, S. Udry, Z. Wahhaj, J. P. Williams, E. Buenzli, M. Cudel, C. Dominik, R. Galicher, M. Kasper, J. Lannier, D. Mesa, D. Mouillet, S. Peretti, C. Perrot, G. Salter, E. Sissa, F. Wildi, L. Abe, J. Antichi, J. C. Augereau, A. Baruffolo, P. Baudoz, A. Bazzon, J. L. Beuzit, P. Blanchard, S. S. Brems, T. Buey, V. De Caprio, M. Carbillet, M. Carle, E. Cascone, A. Cheetham, R. Claudi, A. Costille, A. Delboulbé, K. Dohlen, D. Fantinel, P. Feautrier, T. Fusco, E. Giro, L. Gluck, C. Gry, N. Hubin, E. Hugot, M. Jaquet, D. Le Mignant, M. Llored, F. Madec, Y. Magnard, P. Martinez, D. Maurel, M. Meyer, O. Möller-Nilsson, T. Moulin, L. Mugnier, A. Origné, A. Pavlov, D. Perret, C. Petit, J. Pragt, P. Puget, P. Rabou, J. Ramos, F. Rigal, S. Rochat, R. Roelfsema, G. Rousset, A. Roux, B. Salasnich, J. F. Sauvage, A. Sevin, C. Soenke, E. Stadler, M. Suarez, M. Turatto, and L. Weber. Discovery of a planetary-mass companion within the gap of the transition disk around PDS 70. , 617:A44, Sep 2018. doi: 10.1051/0004-6361/201832957.
- Hubert Klahr and Wolfgang Brandner. *Planet Formation*. 2006.
- Stefan Kraus, Alexander Kreplin, Misato Fukugawa, Takayuki Muto, Michael L. Sitko, Alison K. Young, Matthew R. Bate, Carol Grady, Tim T. Harries, John D. Monnier, Matthew Willson, and John Wisniewski. Dust-trapping Vortices and a Potentially Planet-triggered Spiral Wake in the Pre-transitional Disk of V1247 Orionis. , 848(1):L11, October 2017. doi: 10.3847/2041-8213/aa8edc.
- Tomoyuki Kudo, Jun Hashimoto, Takayuki Muto, Haiyu Baobab Liu, Ruobing Dong, Yasuhiro Hasegawa, Takashi Tsukagoshi, and Mihoko Konishi. A Spatially Resolved au-scale Inner Disk around DM Tau. , 868(1):L5, November 2018. doi: 10.3847/2041-8213/aaeb1c.
- Charles J. Lada. Star formation: from OB associations to protostars. In Manuel Peimbert and Jun Jugaku, editors, *Star Forming Regions*, volume 115, page 1, January 1987.
- David Lafrenière, Christian Marois, René Doyon, Daniel Nadeau, and Étienne Artigau. A New Algorithm for Point-Spread Function Subtraction in High-Contrast Imaging: A Demonstration with Angular Differential Imaging. , 660(1):770–780, May 2007. doi: 10.1086/513180.
- A. M. Lagrange, D. Gratadour, G. Chauvin, T. Fusco, D. Ehrenreich, D. Mouillet, G. Rousset, D. Rouan, F. Allard, É. Gendron, J. Charton, L. Mugnier, P. Rabou, J. Montri, and F. Lacombe. A probable giant planet imaged in the β Pictoris disk. VLT/NaCo deep L'-band imaging. , 493(2):L21–L25, Jan 2009. doi: 10.1051/0004-6361:200811325.
- R. Launhardt, Th. Henning, A. Quirrenbach, D. Ségransan, H. Avenhaus, R. van Boekel, S. S. Brems, A. C. Cheetham, G. Cugno, J. Girard, N. Godoy, G. M. Kennedy, A. L. Maire, S. Metchev, A. Müller, A. Musso Barucci, J. Olofsson, F. Pepe, S. P. Quanz, D. Queloz, S. Reffert, E. L. Rickman, H. L. Ruh, and M. Samland. ISPY-NACO Imaging Survey for Planets around Young stars. Survey description and results from the first 2.5 years of observations. , 635:A162, March 2020. doi: 10.1051/0004-6361/201937000.
- Ya-Ping Li, Hui Li, Shengtai Li, and Douglas N. C. Lin. On the Dust Signatures Induced by Eccentric Super-Earths in Protoplanetary Disks. , 886(1):62, Nov 2019. doi: 10.3847/

- Giuseppe Lodato, Giovanni Dipierro, Enrico Ragusa, Feng Long, Gregory J. Herczeg, Ilaria Pascucci, Paola Pinilla, Carlo F. Manara, Marco Tazzari, Yao Liu, Gijs D. Mulders, Daniel Harsono, Yann Boehler, François Ménard, Doug Johnstone, Colette Salyk, Gerrit van der Plas, Sylvie Cabrit, Suzan Edwards, William J. Fischer, Nathan Hendler, Brunella Nisini, Elisabetta Rigliaco, Henning Avenhaus, Andrea Banzatti, and Michael Gully-Santiago. The newborn planet population emerging from ring-like structures in discs. , 486(1):453–461, Jun 2019. doi: 10.1093/mnras/stz913.
- Feng Long, Paola Pinilla, Gregory J. Herczeg, Daniel Harsono, Giovanni Dipierro, Ilaria Pascucci, Nathan Hendler, Marco Tazzari, Enrico Ragusa, Colette Salyk, Suzan Edwards, Giuseppe Lodato, Gerrit van de Plas, Doug Johnstone, Yao Liu, Yann Boehler, Sylvie Cabrit, Carlo F. Manara, Francois Menard, Gijs D. Mulders, Brunella Nisini, William J. Fischer, Elisabetta Rigliaco, Andrea Banzatti, Henning Avenhaus, and Michael Gully-Santiago. Gaps and Rings in an ALMA Survey of Disks in the Taurus Star-forming Region. , 869(1):17, Dec 2018. doi: 10.3847/1538-4357/aae8e1.
- S. H. Lubow and R. G. Martin. Accretion Outbursts in Circumplanetary Disks. , 749(2):L37, April 2012. doi: 10.1088/2041-8205/749/2/L37.
- S. H. Lubow, M. Seibert, and P. Artymowicz. Disk Accretion onto High-Mass Planets. , 526(2):1001–1012, December 1999. doi: 10.1086/308045.
- A. L. Maire, T. Stolker, S. Messina, A. Müller, B. A. Biller, T. Currie, C. Dominik, C. A. Grady, A. Boccaletti, M. Bonnefoy, G. Chauvin, R. Galicher, M. Millward, A. Pohl, W. Brandner, T. Henning, A. M. Lagrange, M. Langlois, M. R. Meyer, S. P. Quanz, A. Vigan, A. Zurlo, R. van Boekel, E. Buenzli, T. Buey, S. Desidera, M. Feldt, T. Fusco, C. Ginski, E. Giro, R. Gratton, N. Hubin, J. Lannier, D. Le Mignant, D. Mesa, S. Peretti, C. Perrot, J. R. Ramos, G. Salter, M. Samland, E. Sissa, E. Stadler, C. Thalmann, S. Udry, and L. Weber. Testing giant planet formation in the transitional disk of SAO 206462 using deep VLT/SPHERE imaging. , 601:A134, May 2017. doi: 10.1051/0004-6361/201629896.
- Christian Marois, David Lafrenière, René Doyon, Bruce Macintosh, and Daniel Nadeau. Angular Differential Imaging: A Powerful High-Contrast Imaging Technique. , 641(1):556–564, April 2006. doi: 10.1086/500401.
- Christian Marois, Bruce Macintosh, Travis Barman, B. Zuckerman, Inseok Song, Jennifer Patience, David Lafrenière, and René Doyon. Direct Imaging of Multiple Planets Orbiting the Star HR 8799. *Science*, 322(5906):1348, November 2008. doi: 10.1126/science.1166585.
- D. Mawet, J. Milli, Z. Wahhaj, D. Pelat, O. Absil, C. Delacroix, A. Boccaletti, M. Kasper, M. Kenworthy, C. Marois, B. Mennesson, and L. Pueyo. Fundamental Limitations of High Contrast Imaging Set by Small Sample Statistics. , 792(2):97, September 2014. doi: 10.1088/0004-637X/792/2/97.
- J. Milli, P. Higon, V. Christiaens, É. Choquet, M. Bonnefoy, G. M. Kennedy, M. C. Wyatt, O. Absil, C. A. Gómez González, C. del Burgo, L. Matrà, J. C. Augereau, A. Boccaletti, C. Delacroix, S. Ertel, W. R. F. Dent, P. Forsberg, T. Fusco, J. H. Girard, S. Habraken, E. Huby, M. Karlsson, A. M. Lagrange, D. Mawet, D. Mouillet, M. Perrin, C. Pinte, L. Pueyo, C. Reyes, R. Soummer, J. Surdej, Y. Tarricq, and Z. Wahhaj. Discovery of a low-mass companion inside the debris ring surrounding the F5V star HD 206893. , 597:

L2, January 2017. doi: 10.1051/0004-6361/201629908.

- John D. Monnier, Tim J. Harries, Alicia Aarnio, Fred C. Adams, Sean Andrews, Nuria Calvet, Catherine Espaillat, Lee Hartmann, Sasha Hinkley, Stefan Kraus, Melissa McClure, Rebecca Oppenheimer, Marshall Perrin, and David Wilner. Polarized Disk Emission from Herbig Ae/Be Stars Observed Using Gemini Planet Imager: HD 144432, HD 150193, HD 163296, and HD 169142. , 838(1):20, March 2017. doi: 10.3847/1538-4357/aa6248.
- John D. Monnier, Tim J. Harries, Jaehan Bae, Benjamin R. Setterholm, Anna Laws, Alicia Aarnio, Fred C. Adams, Sean Andrews, Nuria Calvet, Catherine Espaillat, Lee Hartmann, Stefan Kraus, Melissa McClure, Chris Miller, Rebecca Oppenheimer, David Wilner, and Zhaohuan Zhu. Multiple Spiral Arms in the Disk around Intermediate-mass Binary HD 34700A. , 872(2):122, Feb 2019. doi: 10.3847/1538-4357/aafe87.
- Matías Montesinos, Jorge Cuadra, Sebastian Perez, Clément Baruteau, and Simon Casassus. Protoplanetary Disks Including Radiative Feedback from Accreting Planets. , 806(2):253, June 2015. doi: 10.1088/0004-637X/806/2/253.
- A. Morbidelli, J. Szulágyi, A. Crida, E. Lega, B. Bitsch, T. Tanigawa, and K. Kanagawa. Meridional circulation of gas into gaps opened by giant planets in three-dimensional low-viscosity disks. , 232:266–270, April 2014. doi: 10.1016/j.icarus.2014.01.010.
- C. Mordasini, Y. Alibert, H. Klahr, and T. Henning. Characterization of exoplanets from their formation. I. Models of combined planet formation and evolution. , 547:A111, November 2012. doi: 10.1051/0004-6361/201118457.
- C. Mordasini, G. D. Marleau, and P. Mollière. Characterization of exoplanets from their formation. III. The statistics of planetary luminosities. , 608:A72, December 2017. doi: 10.1051/0004-6361/201630077.
- Christoph Mordasini. *Planetary Population Synthesis*, page 143. 2018. doi: 10.1007/978-3-319-55333-7_143.
- A. Müller, M. Keppler, Th. Henning, M. Samland, G. Chauvin, H. Beust, A. L. Maire, K. Molaverdikhani, R. van Boekel, M. Benisty, A. Boccaletti, M. Bonnefoy, F. Cantalloube, B. Charnay, J. L. Baudino, M. Gennaro, Z. C. Long, A. Cheetham, S. Desidera, M. Feldt, T. Fusco, J. Girard, R. Gratton, J. Hagelberg, M. Janson, A. M. Lagrange, M. Langlois, C. Lazzoni, R. Ligi, F. Ménard, D. Mesa, M. Meyer, P. Mollière, C. Mordasini, T. Moulin, A. Pavlov, N. Pawellek, S. P. Quanz, J. Ramos, D. Rouan, E. Sissa, E. Stadler, A. Vigan, Z. Wahhaj, L. Weber, and A. Zurlo. Orbital and atmospheric characterization of the planet within the gap of the PDS 70 transition disk. , 617:L2, September 2018. doi: 10.1051/0004-6361/201833584.
- A. Natta, L. Testi, N. Calvet, Th. Henning, R. Waters, and D. Wilner. Dust in Protoplanetary Disks: Properties and Evolution. In Bo Reipurth, David Jewitt, and Klaus Keil, editors, *Protostars and Planets V*, page 767, January 2007.
- Satoshi Okuzumi, Hidekazu Tanaka, Hiroshi Kobayashi, and Koji Wada. Rapid Coagulation of Porous Dust Aggregates outside the Snow Line: A Pathway to Successful Icy Planetesimal Formation. , 752(2):106, June 2012. doi: 10.1088/0004-637X/752/2/106.
- S. J. Paardekooper and G. Mellema. Planets opening dust gaps in gas disks. , 425:L9–L12, October 2004. doi: 10.1051/0004-6361:200400053.

- J. C. B. Papaloizou and R. P. Nelson. Models of accreting gas giant protoplanets in protostellar disks. , 433(1):247–265, April 2005. doi: 10.1051/0004-6361:20042029.
- Laura M. Pérez, John M. Carpenter, Sean M. Andrews, Luca Ricci, Andrea Isella, Hendrik Linz, Anneila I. Sargent, David J. Wilner, Thomas Henning, Adam T. Deller, Claire J. Chandler, Cornelis P. Dullemond, Joseph Lazio, Karl M. Menten, Stuartt A. Corder, Shaye Storm, Leonardo Testi, Marco Tazzari, Woojin Kwon, Nuria Calvet, Jane S. Greaves, Robert J. Harris, and Lee G. Mundy. Spiral density waves in a young protoplanetary disk. *Science*, 353(6307):1519–1521, Sep 2016. doi: 10.1126/science.aaf8296.
- Laura M. Pérez, Myriam Benisty, Sean M. Andrews, Andrea Isella, Cornelis P. Dullemond, Jane Huang, Nicolás T. Kurtovic, Viviana V. Guzmán, Zhaohuan Zhu, Tilman Birnstiel, Shangjia Zhang, John M. Carpenter, David J. Wilner, Luca Ricci, Xue-Ning Bai, Erik Weaver, and Karin I. Öberg. The Disk Substructures at High Angular Resolution Project (DSHARP). X. Multiple Rings, a Misaligned Inner Disk, and a Bright Arc in the Disk around the T Tauri star HD 143006. , 869(2):L50, Dec 2018. doi: 10.3847/2041-8213/aaf745.
- Sebastián Pérez, Simon Casassus, Clément Baruteau, Ruobing Dong, Antonio Hales, and Lucas Cieza. Dust Unveils the Formation of a Mini-Neptune Planet in a Protoplanetary Ring. , 158(1):15, July 2019. doi: 10.3847/1538-3881/ab1f88.
- P. Pinilla, M. Benisty, and T. Birnstiel. Ring shaped dust accumulation in transition disks. , 545:A81, September 2012. doi: 10.1051/0004-6361/201219315.
- P. Pinilla, L. M. Pérez, S. Andrews, N. van der Marel, E. F. van Dishoeck, S. Ataiee, M. Benisty, T. Birnstiel, A. Juhász, A. Natta, L. Ricci, and L. Testi. A Multi-wavelength Analysis of Dust and Gas in the SR 24S Transition Disk. , 839(2):99, April 2017a. doi: 10.3847/1538-4357/aa6973.
- P. Pinilla, A. Pohl, S. M. Stammler, and T. Birnstiel. Dust Density Distribution and Imaging Analysis of Different Ice Lines in Protoplanetary Disks. , 845(1):68, Aug 2017b. doi: 10.3847/1538-4357/aa7edb.
- P. Pinilla, M. Benisty, J. de Boer, C. F. Manara, J. Bouvier, C. Dominik, C. Ginski, R. A. Loomis, and A. Sicilia Aguilar. Variable Outer Disk Shadowing around the Dipper Star RXJ1604.3-2130. , 868(2):85, December 2018a. doi: 10.3847/1538-4357/aae824.
- P. Pinilla, M. Tazzari, I. Pascucci, A. N. Youdin, A. Garufi, C. F. Manara, L. Testi, G. van der Plas, S. A. Barenfeld, H. Canovas, E. G. Cox, N. P. Hendler, L. M. Pérez, and N. van der Marel. Homogeneous Analysis of the Dust Morphology of Transition Disks Observed with ALMA: Investigating Dust Trapping and the Origin of the Cavities. , 859(1):32, May 2018b. doi: 10.3847/1538-4357/aabf94.
- C. Pinte, D. J. Price, F. Ménard, G. Duchêne, W. R. F. Dent, T. Hill, I. de Gregorio-Monsalvo, A. Hales, and D. Mentiplay. Kinematic Evidence for an Embedded Protoplanet in a Circumstellar Disk. , 860(1):L13, Jun 2018. doi: 10.3847/2041-8213/aac6dc.
- C. Pinte, G. van der Plas, F. Ménard, D. J. Price, V. Christiaens, T. Hill, D. Mentiplay, C. Ginski, E. Choquet, Y. Boehler, G. Duchêne, S. Perez, and S. Casassus. Kinematic detection of a planet carving a gap in a protoplanetary disk. *Nature Astronomy*, 3:1109–1114, Aug 2019. doi: 10.1038/s41550-019-0852-6.
- C. Pinte, D. J. Price, F. Ménard, G. Duchêne, V. Christiaens, S. M. Andrews, J. Huang,

- T. Hill, G. van der Plas, L. M. Perez, A. Isella, Y. Boehler, W. R. F. Dent, D. Mentiplay, and R. A. Loomis. Nine Localized Deviations from Keplerian Rotation in the DSHARP Circumstellar Disks: Kinematic Evidence for Protoplanets Carving the Gaps. , 890(1):L9, February 2020. doi: 10.3847/2041-8213/ab6dda.
- James B. Pollack, Olenka Hubickyj, Peter Bodenheimer, Jack J. Lissauer, Morris Podolak, and Yuval Greenzweig. Formation of the Giant Planets by Concurrent Accretion of Solids and Gas. , 124(1):62–85, Nov 1996. doi: 10.1006/icar.1996.0190.
- T. Preibisch and E. Mamajek. *The Nearest OB Association: Scorpius-Centaurus (Sco OB2)*, volume 5, page 235. 2008.
- Giovanni Privitera, Georges Meynet, Patrick Eggenberger, Aline A. Vidotto, Eva Villaver, and Michele Bianda. Star-planet interactions. I. Stellar rotation and planetary orbits. , 591:A45, Jun 2016. doi: 10.1051/0004-6361/201528044.
- Sascha P. Quanz, Adam Amara, Michael R. Meyer, Julien H. Girard, Matthew A. Kenworthy, and Markus Kasper. Confirmation and Characterization of the Protoplanet HD 100546 b—Direct Evidence for Gas Giant Planet Formation at 50 AU. , 807(1):64, Jul 2015. doi: 10.1088/0004-637X/807/1/64.
- A. C. Quillen and D. E. Trilling. Do Proto-jovian Planets Drive Outflows? , 508(2):707–713, December 1998. doi: 10.1086/306421.
- J. Rameau, G. Chauvin, A. M. Lagrange, H. Klahr, M. Bonnefoy, C. Mordasini, M. Bonavita, S. Desidera, C. Dumas, and J. H. Girard. A survey of young, nearby, and dusty stars conducted to understand the formation of wide-orbit giant planets. VLT/NaCo adaptive optics thermal and angular differential imaging. , 553:A60, May 2013a. doi: 10.1051/0004-6361/201220984.
- J. Rameau, G. Chauvin, A. M. Lagrange, T. Meshkat, A. Boccaletti, S. P. Quanz, T. Currie, D. Mawet, J. H. Girard, M. Bonnefoy, and M. Kenworthy. Confirmation of the Planet around HD 95086 by Direct Imaging. , 779(2):L26, Dec 2013b. doi: 10.1088/2041-8205/779/2/L26.
- Suvrat Rao, Georges Meynet, Patrick Eggenberger, Lionel Haemmerlé, Giovanni Privitera, Cyril Georgy, Sylvia Ekström, and Christoph Mordasini. Star-planet interactions. V. Dynamical and equilibrium tides in convective zones. , 618:A18, Oct 2018. doi: 10.1051/0004-6361/201833107.
- E. Sanchis, G. Picogna, B. Ercolano, L. Testi, and G. Rosotti. Detectability of embedded protoplanets from hydrodynamical simulations. , 492(3):3440–3458, Mar 2020. doi: 10.1093/mnras/staa074.
- Kevin C. Schlaufman. Evidence of an Upper Bound on the Masses of Planets and Its Implications for Giant Planet Formation. , 853(1):37, January 2018. doi: 10.3847/1538-4357/aa961c.
- J. Schneider, C. Dedieu, P. Le Sidaner, R. Savalle, and I. Zolotukhin. Defining and cataloging exoplanets: the exoplanet.eu database. , 532:A79, August 2011. doi: 10.1051/0004-6361/201116713.
- Patrick D. Sheehan and Josh A. Eisner. Multiple Gaps in the Disk of the Class I Protostar GY 91. , 857(1):18, Apr 2018. doi: 10.3847/1538-4357/aaae65.

- Frank H. Shu, Fred C. Adams, and Susana Lizano. Star formation in molecular clouds: observation and theory. , 25:23–81, January 1987. doi: 10.1146/annurev.aa.25.090187.000323.
- Jacob B. Simon and Philip J. Armitage. Efficiency of Particle Trapping in the Outer Regions of Protoplanetary Disks. , 784(1):15, Mar 2014. doi: 10.1088/0004-637X/784/1/15.
- Rémi Soummer, Laurent Pueyo, and James Larkin. Detection and Characterization of Exoplanets and Disks Using Projections on Karhunen-Loève Eigenimages. , 755(2):L28, Aug 2012. doi: 10.1088/2041-8205/755/2/L28.
- Tomas Stolker, Mike Sitko, Bernard Lazareff, Myriam Benisty, Carsten Dominik, Rens Waters, Michiel Min, Sebastian Perez, Julien Milli, Antonio Garufi, Jozua de Boer, Christian Ginski, Stefan Kraus, Jean-Philippe Berger, and Henning Avenhaus. Variable Dynamics in the Inner Disk of HD 135344B Revealed with Multi-epoch Scattered Light Imaging. , 849(2):143, November 2017. doi: 10.3847/1538-4357/aa886a.
- J. Szulágyi, A. Morbidelli, A. Crida, and F. Masset. Accretion of Jupiter-mass Planets in the Limit of Vanishing Viscosity. , 782(2):65, February 2014. doi: 10.1088/0004-637X/782/2/65.
- J. Szulágyi, G. van der Plas, M. R. Meyer, A. Pohl, S. P. Quanz, L. Mayer, S. Daemgen, and V. Tamburello. Observability of forming planets and their circumplanetary discs - I. Parameter study for ALMA. , 473(3):3573–3583, January 2018. doi: 10.1093/mnras/stx2602.
- J. Szulágyi, C. P. Dullemond, A. Pohl, and S. P. Quanz. Observability of forming planets and their circumplanetary discs II. - SEDs and near-infrared fluxes. , 487(1):1248–1258, July 2019. doi: 10.1093/mnras/stz1326.
- Ya-Wen Tang, Stephane Guilloteau, Anne Dutrey, Takayuki Muto, Bo-Ting Shen, Pin-Gao Gu, Shu-ichiro Inutsuka, Munetake Momose, Vincent Pietu, Misato Fukagawa, Edwige Chapillon, Paul T. P. Ho, Emmanuel di Folco, Stuartt Corder, Nagayoshi Ohashi, and Jun Hashimoto. Planet Formation in AB Aurigae: Imaging of the Inner Gaseous Spirals Observed inside the Dust Cavity. , 840(1):32, May 2017. doi: 10.3847/1538-4357/aa6af7.
- Takayuki Tanigawa, Keiji Ohtsuki, and Masahiro N. Machida. Distribution of Accreting Gas and Angular Momentum onto Circumplanetary Disks. , 747(1):47, March 2012. doi: 10.1088/0004-637X/747/1/47.
- Richard Teague, Jaehan Bae, Edwin A. Bergin, Tilman Birnstiel, and Daniel Foreman-Mackey. A Kinematical Detection of Two Embedded Jupiter-mass Planets in HD 163296. , 860(1):L12, June 2018. doi: 10.3847/2041-8213/aac6d7.
- S. Terebey, F. H. Shu, and P. Cassen. The collapse of the cores of slowly rotating isothermal clouds. , 286:529–551, November 1984. doi: 10.1086/162628.
- Takashi Tsukagoshi, Munetake Momose, Yoshimi Kitamura, Masao Saito, Ryohei Kawabe, Sean Andrews, David Wilner, Tomoyuki Kudo, Jun Hashimoto, Nagayoshi Ohashi, and Motohide Tamura. The Flared Gas Structure of the Transitional Disk around Sz 91. , 871(1):5, January 2019. doi: 10.3847/1538-4357/aaf4f1.
- N. J. Turner, Man Hoi Lee, and T. Sano. Magnetic Coupling in the Disks around Young Gas Giant Planets. , 783(1):14, March 2014. doi: 10.1088/0004-637X/783/1/14.

- Nienke van der Marel. *Mind the gap: gas and dust in planet-forming disks*. PhD thesis, Leiden University, September 2015.
- Nienke van der Marel, Jonathan P. Williams, M. Ansdell, Carlo F. Manara, Anna Miotello, Marco Tazzari, Leonardo Testi, Michiel Hogerheijde, Simon Bruderer, Sierk E. van Terwisga, and Ewine F. van Dishoeck. New Insights into the Nature of Transition Disks from a Complete Disk Survey of the Lupus Star-forming Region. , 854(2):177, February 2018a. doi: 10.3847/1538-4357/aaaa6b.
- Nienke van der Marel, Jonathan P. Williams, and Simon Bruderer. Rings and Gaps in Protoplanetary Disks: Planets or Snowlines? , 867(1):L14, November 2018b. doi: 10.3847/2041-8213/aae88e.
- G. van der Plas, F. Ménard, H. Canovas, H. Avenhaus, S. Casassus, C. Pinte, C. Caceres, and L. Cieza. An 80 au cavity in the disk around HD 34282. , 607:A55, November 2017. doi: 10.1051/0004-6361/201731392.
- S. E. van Terwisga, E. F. van Dishoeck, M. Ansdell, N. van der Marel, L. Testi, J. P. Williams, S. Facchini, M. Tazzari, M. R. Hogerheijde, L. Trapman, C. F. Manara, A. Miotello, L. T. Maud, and D. Harsono. V1094 Scorpii: A rare giant multi-ringed disk around a T Tauri star. , 616:A88, August 2018. doi: 10.1051/0004-6361/201832862.
- M. Villenave, M. Benisty, W. R. F. Dent, F. Ménard, A. Garufi, C. Ginski, P. Pinilla, C. Pinte, J. P. Williams, J. de Boer, J. I. Morino, M. Fukagawa, C. Dominik, M. Flock, T. Henning, A. Juhász, M. Keppler, G. Muro-Arena, J. Olofsson, L. M. Pérez, G. van der Plas, A. Zurlo, M. Carle, P. Feautrier, A. Pavlov, J. Pragt, J. Ramos, J. F. Sauvage, E. Stadler, and L. Weber. Spatial segregation of dust grains in transition disks. SPHERE observations of 2MASS J16083070-3828268 and RXJ1852.3-3700. , 624:A7, April 2019. doi: 10.1051/0004-6361/201834800.
- Kevin Wagner, Katherine B. Follete, Laird M. Close, Dániel Apai, Aidan Gibbs, Miriam Keppler, André Müller, Thomas Henning, Markus Kasper, Ya-Lin Wu, Joseph Long, Jared Males, Katie Morzinski, and Melissa McClure. Magellan Adaptive Optics Imaging of PDS 70: Measuring the Mass Accretion Rate of a Young Giant Planet within a Gapped Disk. , 863(1):L8, August 2018. doi: 10.3847/2041-8213/aad695.
- B. A. Wilking, M. Gagné, and L. E. Allen. *Star Formation in the ρ Ophiuchi Molecular Cloud*, volume 5, page 351. 2008.
- Jonathan P. Williams and Lucas A. Cieza. Protoplanetary Disks and Their Evolution. , 49(1):67–117, September 2011. doi: 10.1146/annurev-astro-081710-102548.
- Joshua N. Winn and Daniel C. Fabrycky. The Occurrence and Architecture of Exoplanetary Systems. , 53:409–447, Aug 2015. doi: 10.1146/annurev-astro-082214-122246.
- A. Wolszczan and D. A. Frail. A planetary system around the millisecond pulsar PSR1257 + 12. , 355(6356):145–147, Jan 1992. doi: 10.1038/355145a0.
- Jason T. Wright. *Radial Velocities as an Exoplanet Discovery Method*, page 4. 2018. doi: 10.1007/978-3-319-55333-7_4.
- Ke Zhang, Geoffrey A. Blake, and Edwin A. Bergin. Evidence of Fast Pebble Growth Near Condensation Fronts in the HL Tau Protoplanetary Disk. , 806(1):L7, June 2015. doi: 10.1088/2041-8205/806/1/L7.

- Shangjia Zhang, Zhaohuan Zhu, Jane Huang, Viviana V. Guzmán, Sean M. Andrews, Tilman Birnstiel, Cornelis P. Dullemond, John M. Carpenter, Andrea Isella, Laura M. Pérez, Myriam Benisty, David J. Wilner, Clément Baruteau, Xue-Ning Bai, and Luca Ricci. The Disk Substructures at High Angular Resolution Project (DSHARP). VII. The Planet-Disk Interactions Interpretation. , 869(2):L47, Dec 2018. doi: 10.3847/2041-8213/aaf744.
- Zhaohuan Zhu. Accreting Circumplanetary Disks: Observational Signatures. , 799(1):16, January 2015. doi: 10.1088/0004-637X/799/1/16.
- Zhaohuan Zhu, Sean M. Andrews, and Andrea Isella. On the radio detectability of circumplanetary discs. , 479(2):1850–1865, September 2018. doi: 10.1093/mnras/sty1503.
- A. Zurlo, G. Cugno, M. Montesinos, S. Perez, H. Canovas, S. Casassus, V. Christiaens, L. Cieza, and N. Huelamo. The widest H α survey of accreting protoplanets around nearby transition disks. , 633:A119, January 2020. doi: 10.1051/0004-6361/201936891.

Appendix A

ADI reductions

In this section, we present the ADI reduction for the 10 planet-forming disks presented in this work. All the methods discussed in Sect. 2.2 were applied for all targets except two: Sz 114 and HT Lup. For this targets, it wasn't possible to secure enough rotation of the FOV for a correct application of the ADI algorithms. For this cases, only the PCA method was applied.

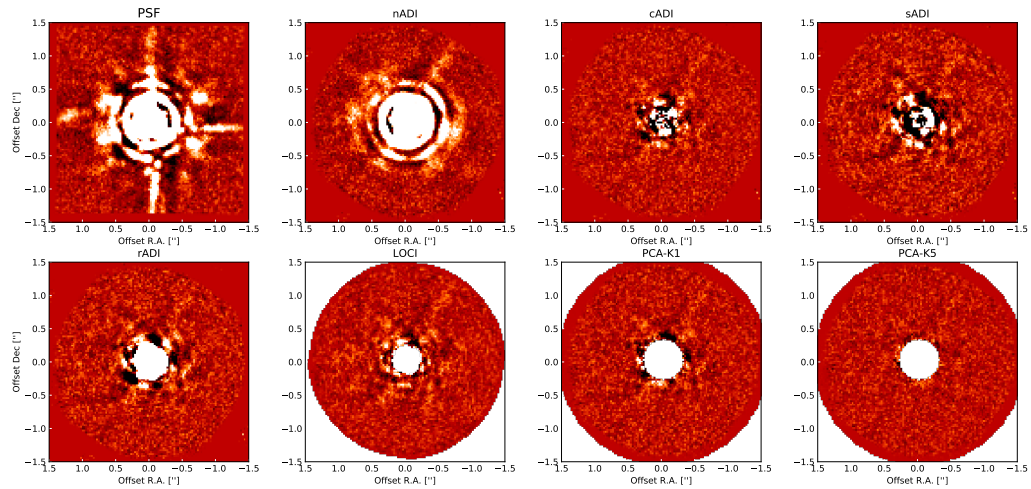


Figure A.1: Gallery containing the all the reduction for the system AS 209. PSF and nADI refer to the original PSF obtained for the system and the median combination of all frames without applying any of the ADI methods, respectively. Although the results are similar, slight differences can be appreciated between the different ADI reduction methods. No companion was found for this system

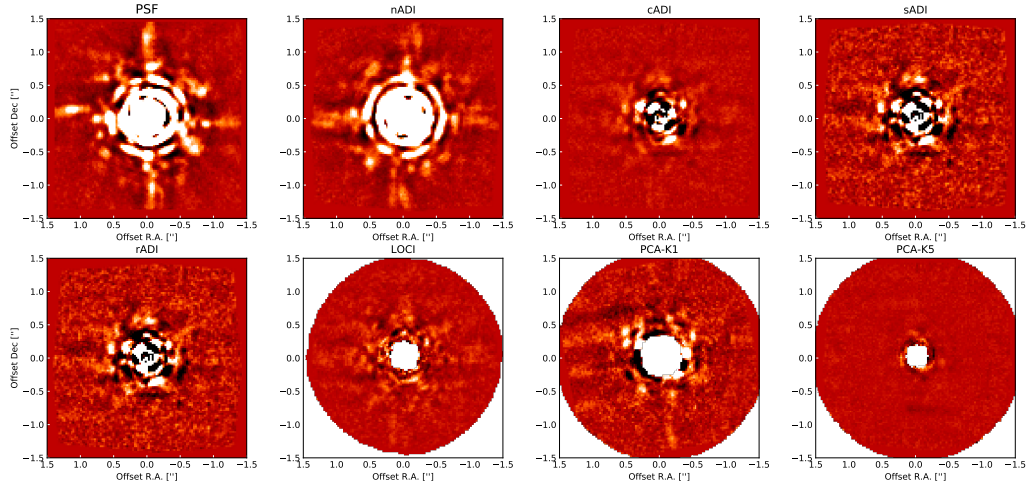


Figure A.2: Gallery containing the all the reduction for the system Elias 24. PSF and nADI refer to the original PSF obtained for the system and the median combination of all frames without applying any of the ADI methods, respectively. Although the results are similar, slight differences can be appreciated between the different ADI reduction methods. An apparent point-like source can be observed at a separation of $\sim 0.4''$ (~ 55 AU) and a position angle of $\sim 300^\circ$ in all the different reductions, as discussed in Sect. 4.2

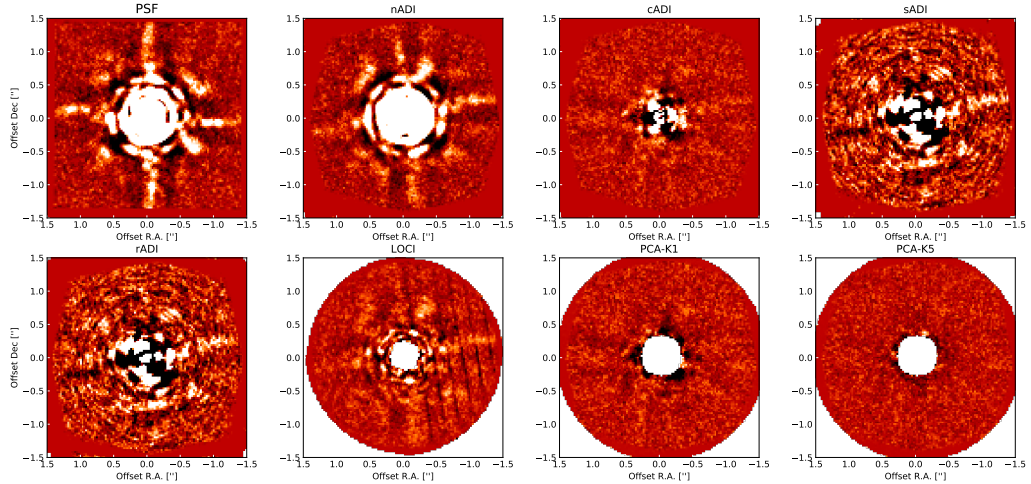


Figure A.3: Gallery containing the all the reduction for the system HD 143006. PSF and nADI refer to the original PSF obtained for the system and the median combination of all frames without applying any of the ADI methods, respectively. Although the results are similar, slight differences can be appreciated between the different ADI reduction methods. Some artifacts remained after the LOCI reduction, but were impossible to completely remove due to the fact that the remotion of more images would compromise the FOV rotation needed for the ADI algorithms to properly work. No companion was found for this system

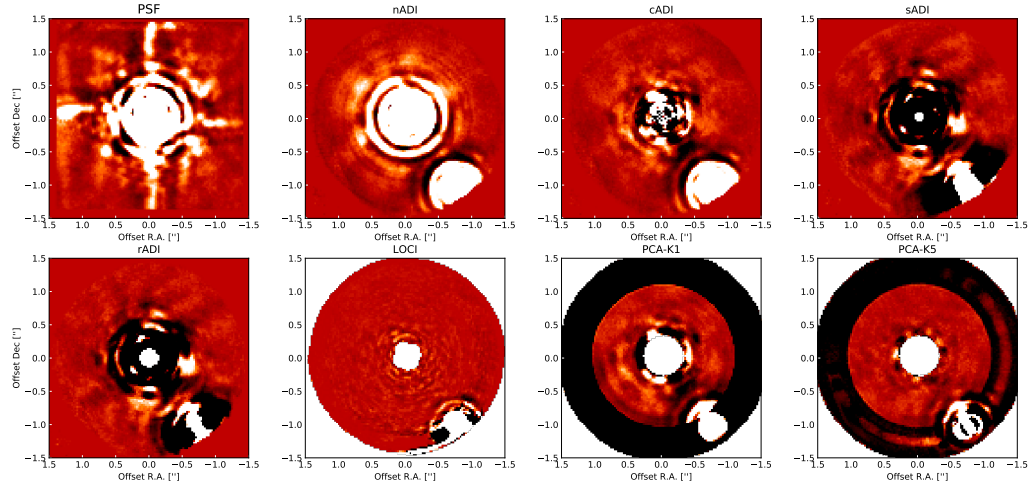


Figure A.4: Gallery containing the all the reduction for the system AS 205. PSF and nADI refer to the original PSF obtained for the system and the median combination of all frames without applying any of the ADI methods, respectively. Although the results are similar, slight differences can be appreciated between the different ADI reduction methods. Due to the presence of a binary companion, detection at the separation of the secondary star is not possible. No companion was found for this system

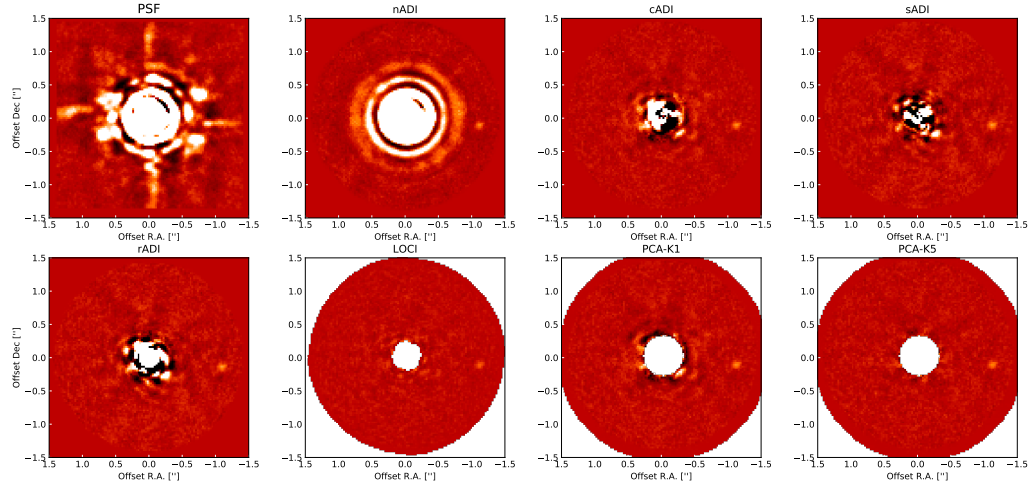


Figure A.5: Gallery containing the all the reduction for the system RU Lup. PSF and nADI refer to the original PSF obtained for the system and the median combination of all frames without applying any of the ADI methods, respectively. Although the results are similar, slight differences can be appreciated between the different ADI reduction methods. An apparent point-like source can be observed at a separation of $\sim 1.1''$ (~ 55 AU) and a position angle of $\sim 260^\circ$ in all the different reductions, as discussed in Sect. 4.1

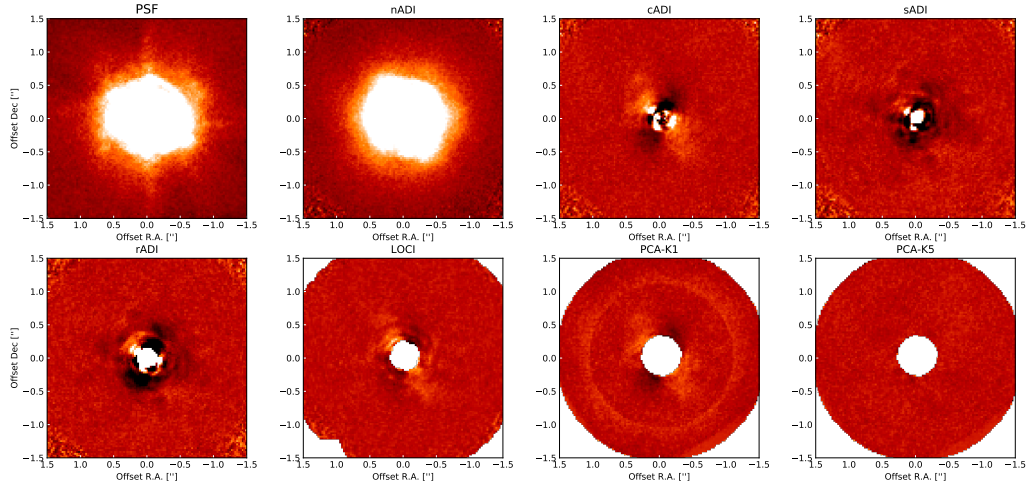


Figure A.6: Gallery containing the all the reduction for the system Sz 129. PSF and nADI refer to the original PSF obtained for the system and the median combination of all frames without applying any of the ADI methods, respectively. Although the results are similar, slight differences can be appreciated between the different ADI reduction methods. No companion was found for this system

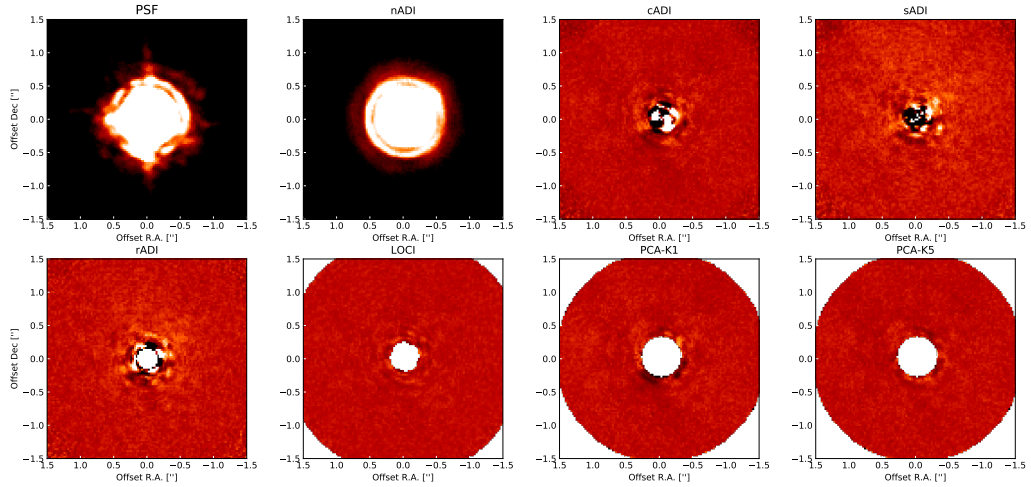


Figure A.7: Gallery containing the all the reduction for the system Wa Oph 6. PSF and nADI refer to the original PSF obtained for the system and the median combination of all frames without applying any of the ADI methods, respectively. Although the results are similar, slight differences can be appreciated between the different ADI reduction methods. No companion was found for this system

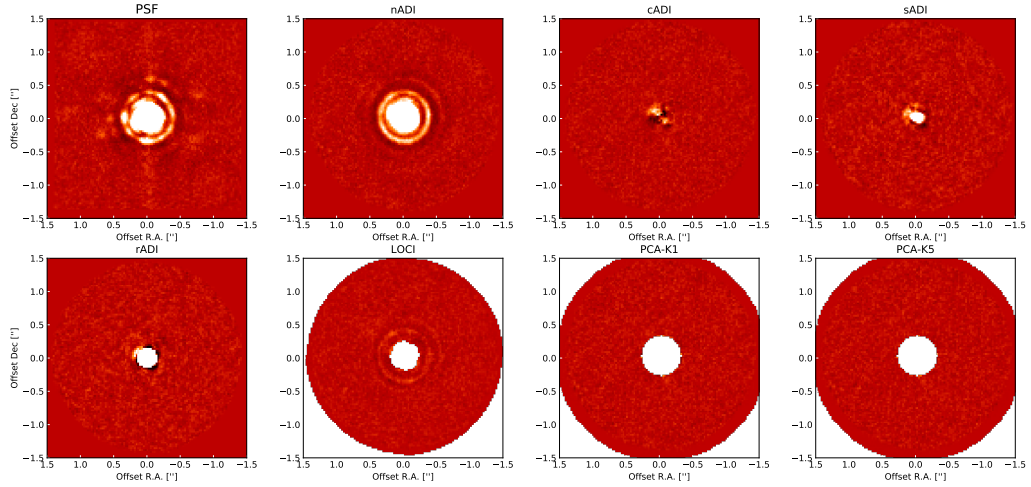


Figure A.8: Gallery containing the all the reduction for the system GW Lup. PSF and nADI refer to the original PSF obtained for the system and the median combination of all frames without applying any of the ADI methods, respectively. Although the results are similar, slight differences can be appreciated between the different ADI reduction methods. No companion was found for this system

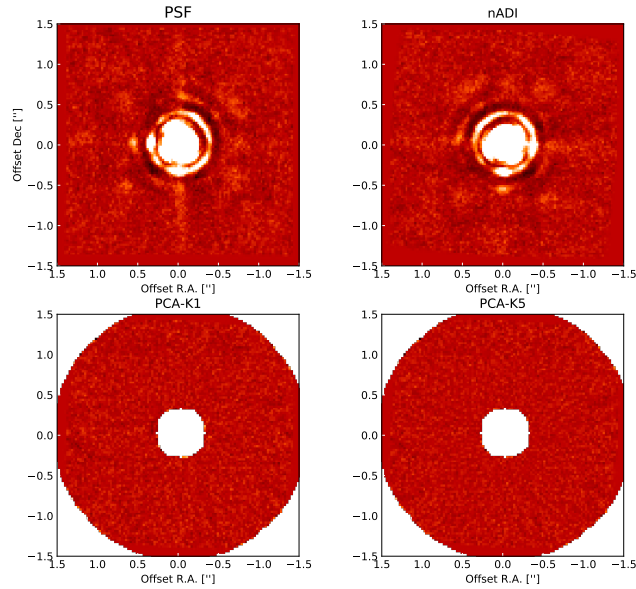


Figure A.9: Gallery containing the all the reduction for the system Sz 114. PSF and nADI refer to the original PSF obtained for the system and the median combination of all frames without applying any of the ADI methods, respectively. Due to lack of enough FOV rotation, only the PCA method was applied. No companion was found for this system

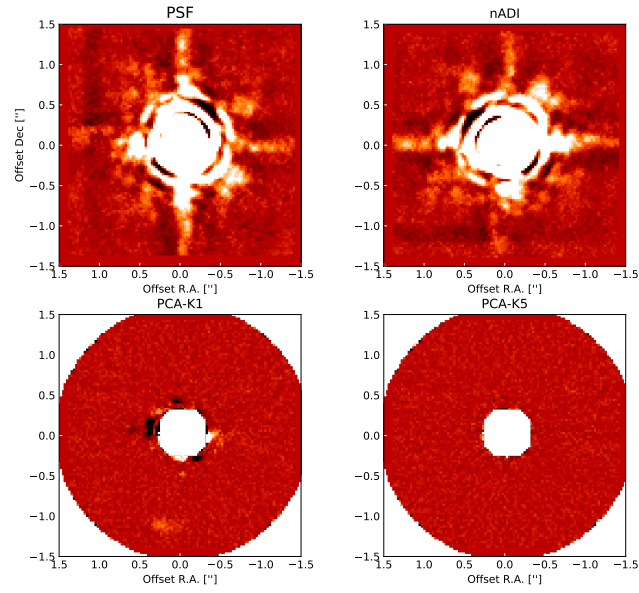


Figure A.10: Gallery containing the all the reduction for the system HT Lup. PSF and nADI refer to the original PSF obtained for the system and the median combination of all frames without applying any of the ADI methods, respectively. Due to lack of enough FOV rotation, only the PCA method was applied. No companion was found for this system